



**Politecnico
di Torino**

CORSO DI LAUREA MAGISTRALE IN INGEGNERIA AEROSPAZIALE

TESI DI LAUREA MAGISTRALE

**Thermo-elastic analysis of variable
stiffness composites**

CANDIDATA

Francesca Bracaglia

RELATORI

Prof. Alfonso Pagani

Prof. Enrico Zappino

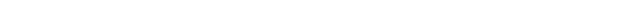
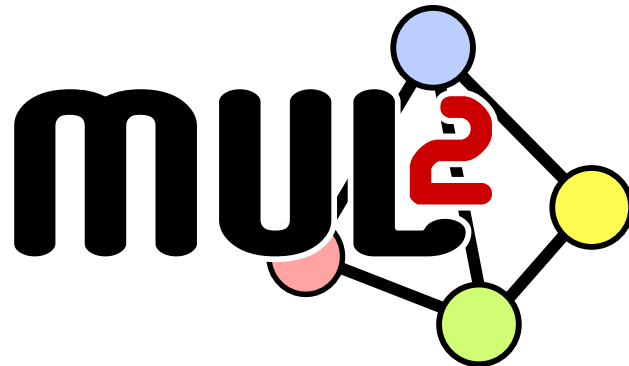
Dott.ssa Rebecca Masia

Prof. Erasmo Carrera

AA. 2022/2023



**Politecnico
di Torino**



Contents

1	Introduction	2
1.1	An overview of composite materials	2
1.2	Thermal environment and thermal buckling	5
1.3	Present work overview	6
2	Preliminary concepts	8
2.1	Constitutive relations	8
2.2	Geometrical relations	11
2.3	Principle of Virtual Displacements, PVD	13
2.4	Plate theories	16
2.4.1	Kirchhoff plate theory	16
2.4.2	Reissner Mindlin plate theory	17
2.4.3	High Order Theories (HOT)	18
3	Carrera Unified Formulation (CUF) and Finite Element (FE) method	21
3.1	Introduction to CUF for 2D theories	21
3.1.1	The FE formulation and the FN	22
3.1.2	Coupled thermo-mechanical problem through CUF and FNs	24
3.1.3	Buckling FNs	25
4	Introduction to multilayered structures	29
4.1	Multilayered structures	29
4.2	Variable angle tow (VAT)	31
4.3	Equivalent Single Layer Method	32
4.4	Layer Wise methods (LW)	33
5	Thermo-mechanical analyses for isotropic and laminated composite plate	35
5.1	Coupled analysis of isotropic laminates	35
5.1.1	Validation of the analysis	35
5.1.2	Convergence study: surfaces elements Q9	37
5.1.3	Convergence study of the expansion along the thickness	40
5.1.4	Best mesh results 20×20 1 LE3 each layer	43
5.2	Decoupled and coupled thermo-mechanical analysis of composite multilayered plate	44
5.2.1	Decoupled approach	45
5.2.2	Coupled approach	50

6	Thermo-mechanical and thermo-buckling analyses of VAT composite plate	56
6.1	Pure mechanical static analysis for VAT composites	56
6.2	VAT thermo-mechanical decoupled analysis	60
6.3	Thermal buckling	63
6.4	Thermal buckling angle optimization	68
6.4.1	Carbon/Epoxy angle optimization	68
6.4.2	E-Glass/Epoxy optimization	73
7	Conclusions	77
7.1	Future Trends	78
A		79
B		81

List of Figures

1.1	(a) Sandwich configuration with honeycomb core [1]. (b) Fiber reinforced composite laminate [2].	4
1.2	VAT laminate representation.	5
2.1	Plate geometry and references system.	16
2.2	Distribution of displacements in Classical Plate Theory.	17
2.3	Distribution of displacements in First shear deformation theory.	18
2.4	Distribution of displacements for different orders of expansion.	19
2.5	Differences between CAD, Lagrange and Taylor for plate.	20
3.1	QUAD element representation. Element numeration and displacement dependence on a random point of the element from all nodes.	23
3.2	Automatic implementation of the stiffness matrix through CUF.	24
3.3	Representation of the ideal buckling representing the cases of bifurcation. On the left plate/beam behavior, on the right typical cylinder buckling behavior where bifurcation point can not be considered as critical load. w represents the in plane deflection.	28
4.1	Rotation angle α and representation of the lamina rotation from a lamina to a global reference system.	30
4.2	Description of the fiber orientation in VAT curvilinear path.	32
4.3	Discretization and local rotation angle for a VAT panel.	32
4.4	Lamination example with an ESL FN representation.	33
4.5	Lamination example with an layer wise FN representation.	34
5.1	Geometry, material and BCs representation of the analyzed plate.	36
5.2	Temperature profile from references [3] and calculated temperature profile with a surface discretization of 20x20 Q9 elements and in-thickness expansion with 4 LE 3. Aluminum external material, steel internal material.	36
5.3	Displacement convergence. Variation of the discretization number of Q9 elements along the plane, 4 LE3 in-thickness expansion. Steel external material, aluminum internal material.	38
5.4	Convergence analysis in x-logarithmic way. Variation in the discretization number of Q9 elements along the plane, 4 LE3 in-thickness expansion. Steel external material, aluminum internal material.	38

5.5	Thickness expansion: one LE3 for each layer, convergence study on surface mesh with Q9 elements. σ_{xx}, σ_{yy} (a) , σ_{xy} (b), σ_{zz} (c), σ_{xz}, σ_{yz} (d), steel external material, aluminum internal material.	39
5.6	Convergence analysis with along the thickness theory LE1,LE2 and LE3, surface mesh 20x20 Q9. Displacement in z-direction. The legend is referred to the expansions used for each layer, steel external material, aluminum internal material.	40
5.7	Convergence analysis with along the thickness theory LE1,LE2 and LE3, surface mesh 20x20 Q9. σ_{xx}, σ_{yy} (a), σ_{xz}, σ_{yz} (b), σ_{xy} (c), σ_{zz} (d).The legend is referred to the expansions used for each layer, steel external material, aluminum internal material.	41
5.8	Convergence analysis with along the thickness theory LE2 and LE3, surface mesh 20x20 Q9. (a) Displacement,(b) Temperature profile, σ_{xx}, σ_{yy} (c), σ_{zz} (d). The legend is referred to the number of element used for each layer, steel external material, aluminum internal material.	42
5.9	Convergence analysis with along the thickness theory LE2 and LE3, surface mesh 20x20 Q9. σ_{xy} (a), σ_{xz} (b). The legend is referred to the number of element used for each layer, steel external material, aluminum internal material.	43
5.10	Results with along the thickness theory 1 LE3 for each layer, surface mesh 20x20 Q9. σ_{xy} (a) , $\sigma_{xz} = \sigma_{yz}$ (b), σ_{zz} (c).	44
5.11	σ_{xx} convergence study graphical representation. Decoupled analysis carried out by the present method.	46
5.12	Displacement z-direction. Comparison between 30 x 30 Q9 with thickness expansion 1 LE3 each layer and ABAQUS analysis.	47
5.13	σ_{xx} . Comparison between 30 x 30 Q9 with thickness expansion 1 LE3 each layer and ABAQUS analysis.	48
5.14	σ_{yy} . Comparison between 30 x 30 Q9 with thickness expansion 1 LE3 each layer and ABAQUS analysis.	48
5.15	Convergence study graphical representation. Coupled analysis carried out by the present method, (a) u_z , (b) σ_{xz}	51
5.16	Displacement taken from present analysis reported in mm. Coupled approach.	52
5.17	Over-temperature profile from point O. Comparison between the present method with thickness expansion 1 LE3 each layer and ABAQUS analysis.	52
5.18	Displacement along the thickness from point O. Comparison between the present method with thickness expansion 1 LE3 each layer and ABAQUS analysis.	53
5.19	σ_{xx} along the thickness from point C. Comparison between the present method with thickness expansion 1 LE3 each layer and ABAQUS analysis.	53
5.20	σ_{yy} along the thickness from point C. Comparison between the present method with thickness expansion 1 LE3 each layer and ABAQUS analysis.	54
5.21	σ_{yz} along the thickness from point C. Comparison between the present method with thickness expansion 1 LE3 each layer and ABAQUS analysis.	54
5.22	σ_{xz} along the thickness from point C. Comparison between the present method with thickness expansion 1 LE3 each layer and ABAQUS analysis.	55
6.1	VAT stacking sequence representation.	57
6.2	z-displacement [m] simply supported, two layers, plate. External pressure $10kPa$, in plane mesh of 14 x 14 Q9 elements, 2LE3 along the thickness. $[0 < 90, 0 >, 0 < 0, 45 >]$	58

6.3	Displacement along z-direction. Comparison between the present method using a mesh 14 x 14 Q9 along the thickness expansion 2LE3 and references results [4]. . . .	58
6.4	$\sigma_{xx}(a), \sigma_{yy}(b), \sigma_{zz}(c), \sigma_{xz}(d), \sigma_{yz}(e), \sigma_{xy}(f)$ comparison between the present method using a mesh 14 x 14 Q9 along the thickness expansion 2LE3 and references results [4].	59
6.5	Displacement along the thickness. Comparison between different approaches. Discretization for the present method 30 x 30 Q9 4LE3. Carbon/Epoxy [0/90/90/0]. . .	61
6.6	σ_{xx} along the thickness. Comparison between different approaches. Discretization for the present method 30 x 30 Q9 4LE3. Carbon/Epoxy [0/90/90/0].	62
6.7	σ_{yy} along the thickness. Comparison between different approaches. Discretization for the present method 30 x 30 Q9 4LE3. Carbon/Epoxy [0/90/90/0].	62
6.8	Plate [mm].	64
6.9	Convergence study for the thermal buckling analysis.	65
6.10	Displacement along z-direction. Convergence study varying the in-plane discretization, 4 LE3 thickness expansion, results have been taken in point P.	66
6.11	Representation of the buckling critical temperature obtained by in-thickness theory variations.	67
6.12	Carbon/Epoxy critical buckling temperature varying the path angles. Present method with ESL and TE2 in-thickness expansion.	68
6.13	Carbon/Epoxy critical buckling temperature varying the path angles. Reference taken from Duran et al. [12]	69
6.14	Carbon/Epoxy critical buckling temperature varying the path angles. LE3 thickness expansion.	69
6.15	Percentage relative increasing accuracy from LE to TE2.	71
6.16	Carbon/Epoxy. Thickness expansion: one LE3 for each layer, 20 x 20 Q9 elements. Comparison of stresses in the better and worst buckling case.(a)(b) σ_{xx} , (c)(d) σ_{yy} . .	72
6.17	Carbon/Epoxy. Thickness expansion: one LE3 for each layer, 20 x 20 Q9 elements. Comparison of stresses in the better and worst buckling case, σ_{zz}	73
6.18	E-Glass/Epoxy critical buckling temperature varying the path angles.	74
6.19	E-Glass/Epoxy critical buckling temperature varying the path angles. Reference taken from Duran et al. [12]	74
6.20	E-Glass/Epoxy. Thickness expansion: one LE3 for each layer, 20 x 20 Q9 elements. Comparison of stresses in the better and worst buckling case, σ_{zz}	75
6.21	E-Glass/Epoxy. Thickness expansion: one LE3 for each layer, 20 x 20 Q9 elements. Comparison of stresses in the better and worst buckling case.(a)(b) σ_{xx} , (c)(d) σ_{yy} . .	76

List of Tables

5.1	Over temperature results for model validation. Surface discretization with 20x20 Q9 elements and in-thickness expansion with 4 LE 3, aluminum external material, steel internal material.	37
5.2	Maximum displacement value for each surface discretization. In-thickness expansion 4LE3. Steel external material, aluminum internal material.	38
5.3	Material coefficients taken from [5]	45
5.4	Convergence study using the present method. The displacement and the stresses are taken in the center of the palate and $z=\pm h/2$	46
5.5	Convergence study in ABAQUS. The displacement and the stresses are taken in the center of the plate and $z=-h/2$	46
5.6	Comparison between coupled and decoupled approaches applied to the same plate.	49
5.7	Convergence study using the present method. The displacement is taken in the center of the plate and $z = 0$, σ_{xz} in the point C (-12.5, -12.5) mm, reference system reported in Figure 5.16.	50
6.1	Simply supported square plate displacement results comparison with respect to the literature [4]. Results taken in the point Q at datum thickness position.	60
6.2	Simply supported square plate stresses results comparison with respect to the literature [4]. Results taken in the point Q at datum thickness position.	60
6.3	Materials properties used in the analysis.	64
6.4	Convergence study considering Q9 elements for the present work and LE3 expansion along the thickness. CLT and Q4 elements are used in reference.	65
6.5	Thermal-buckling critical temperature for changes in the in-thickness expansion theory, 20 x 20 Q9 plate discretization.	67
6.6	Thermal-buckling critical temperature for in-thickness expansion theory changes, 20 x 20 Q9 plate discretization.	67
6.7	Maximum critical buckling temperatures for VAT and straight configuration. Present work with surface mesh 20 x 20 Q9, thickness expansion 4LE3. Carbon/Epoxy.	70
6.8	Minimum critical buckling temperature and orientations. Present work with surface mesh 20 x 20 Q9, thickness expansion 4LE3. Carbon/Epoxy.	70
6.9	Maximum critical buckling temperatures for VAT and straight configuration. Present work with surface mesh 20 x 20 Q9, thickness expansion 4LE3. E-Glass/Epoxy.	75
6.10	Minimum critical buckling temperature and orientations. Present work with surface mesh 20 x 20 Q9, thickness expansion 4LE3. E-Glass/Epoxy.	75
B.1	On the left: Carbon/Epoxy critical temperature. On the right: E-Glass/Epoxy critical temperature.	82

LIST OF TABLES

B.2 Carbon/Epoxy TE2 point of evaluation 83

Abstract

During the last few years, a new class of composite materials has been introduced. The Variable Angle Tow composites (VATs) are materials that are not constrained to the straight deposition of the fibers with the worth of curvilinear fibers path that introduce additional degrees of freedom in the fiber deposition. The property of the laminated material change not only along the thickness, as in the case of the classical laminate, but also along the path of the fibers in the in-plane direction. Nevertheless, this structural advantage introduces a new numerical challenge as a consequence of the material properties variation from one point to another following the curvature. Curved fiber deposition increasingly exploits composite manufacturing technologies. Moreover, it permits the adaptation of the fiber path to the load type retarding some critical phenomena such as bending displacement or buckling deflections. Moreover, some improvements in the specific mechanical properties allow for obtaining lighter structures. One of the most important challenges for the development in the aerospace field is the design of lighter structures, due to this purpose VATs composites have been increasingly studied in the last year.

Composite materials, particularly used in high-speed aircraft and space structures are frequently subjected to thermal environments. Furthermore, lighter structures such as thin panels are required in the aerospace field and low tolerance is mandatory in some precision space applications. These requirements imply the thermal external environment has to be deepened.

Furthermore, thin structures are subjected to buckling phenomena that may cause unexpected deformation and failure, indeed in these applications, stiffness and strength requirements are both fundamental. Buckling occurs when a sudden change in the structure's geometry happens at a critical load value.

The present work is focused on the study of thermal buckling which is a non-linear phenomenon analyzed using the Green-Lagrange geometrical relation and linearizing the problem. Through the use of the well-established Carrera Unified Formulation (CUF), the thermal buckling critical load is investigated through the solution of an eigenvalue problem.

Some convergence and validation analyses comparing the present method with literature and commercial software numerical analyses are reported. Stresses generated under thermal loads are investigated and results are presented for the main aerospace used materials. Laminate made of isotropic layers, straight fibers composite, and VAT composite are analyzed.

The critical temperature corresponding to the bifurcation point is investigated for VAT square panels with a linearized analysis based on the eigenvalues approach. Some final considerations on the optimal layers orientations of the curved fibers path are reported at the end of the thesis with the related thermal stresses.

Chapter 1

Introduction

During the use of spacecraft or aircraft, structures are subjected to the external environment acting as an additional load. The thermal environment is one of the most huge and strong acts on the structures used in space and high-speed aeronautical applications.

Composite materials are particularly subjected to the thermal field. Furthermore, the study of the thermal behavior of composite structures is more complex than traditional material ones considering the presence of more than one expansion coefficient. Such type of load can induce the buckle of the structure. The buckling is a sudden event that can affect thin structures and in some cases lead to breakage.

New composite materials are developed and studied during the last few years. The Variable Angle Tow (VAT) are fiber-reinforced composite material with fibers that follow an in-plane curvilinear path. With the introduction of a new type of composite material, the thermal buckle phenomenon is studied.

1.1 An overview of composite materials

When two or more different materials are assembled together remaining discrete in a macroscopic way a composite is obtained. The definition permits the differentiation of composite materials from metallic alloys which are composed of more than one phase that are not distinguishable from a macroscopic point of view. The main difference between these two material configurations is thus described.

Joining two or more materials together permits improving some specific properties. The combination of different properties allows us to take full gains from the used materials. Indeed, the main advantages of composite use are the high specific properties and the possibility to adapt the configuration to the external load type and the critical phenomena to avoid.

With new improvements in manufacturing, numerical and analytical capability, during the last decades, the use of multilayered structures has quickly risen. Different configurations are involved in the definition of multilayered materials. Some configurations used in the last years include layers made of isotropic alloys, carbon fiber laminates, sandwich structures, and layered ceramic-metallic structures where the common characteristic is the use of more than one material that appears different at a macroscopic level and which combination can create some advantages properties.

Particularly in aerospace, composite materials offer new possibilities to traditional materials due to their corrosion resistance, high strength-to-weight ratio, stiffness, and flexibility. Composite mate-

rials permit, acting on the stacking sequence and lamina orientation, to modify and improve the plate properties even if the material composition does not change. Furthermore, the combination of different materials such as ceramic and carbon fiber reinforced permits the creation of a laminate with variable properties depending on the in-thickness coordinate.

Historically, in the aerospace field, the first composite material involved in aeronautical applications has been wood, an organic composite of cellulose fibers embedded in a matrix of lignin. The properties of the two components are combined and the strength in tension of the fibers could be exploited to the fullest with the matrix action. The matrix permits to join together of the fibers, distributes the load, and protects the fibers from the external environment such as moisture.

In the aerospace field, interest in this type of material has rapidly risen during the last few years. More modern examples are reported. Sandwich structures are composed of at least three layers, two or more external layers called skins and the internal one that is the core of the sandwich. Usually, the material of the skins is high-strength stiffer, instead, the core material is composed of low-density flexible material. Sandwich configuration aims to move away the stiffer material from the neutral axis to increase the bending stiffness of the structure. Usually, the skins are composed of metal or fiber-reinforced composite layers, on the contrary, the core could be honeycomb, foam, web, or truss core to have the lower weight possible. In Figure 1.1 (a) sandwich configuration with a honeycomb core is reported.

Another type of composite material consists of layered structures where two or more layers of different materials are joined together. Layered structures are used with different aims and could be composed of metallic, ceramic, piezo-electric materials, or fiber-reinforced composite. The ceramic layers are usually involved in the thermal protection field. Particularly for reentry vehicles, supersonic aircraft, and engine components thermal protection. Indeed, usually, it is not possible to have the same material presenting both mechanical and thermal high properties. Therefore, layered structures are built of a mechanical structural layer protected by a ceramic one.

Linked to the use of ceramic as a thermal protection layer the Functionally Graded Material (FGM) is defined. FGMs are composite materials with a continuous material variation along the thickness and when ceramic layers are present are used for thermal coating. The variation in the in-thickness properties allows a gradual change in the material from one external layer to the other where a different external environment is present. Different from the classical laminated material the FGM configuration is not involved in delamination problems.

The piezoelectric layers permit to use of multilayer structures as sensors or actuators. The phenomenon of piezoelectricity is a peculiarity of a certain class of crystalline materials and consists of linear energy conversion between mechanical and electrical fields that exploit the multi-field coupling. The linear conversion between the two fields defines a direct or converse piezoelectric effect. The direct piezoelectric effect generates an electric polarization by applying mechanical stresses, on the contrary, the converse piezoelectric effect induces mechanical stresses or strains by applying an electric field.

The more diffused laminated structures family is the fiber-reinforced composite material one. As in the case of wood, the layer is composed of internal fibers that are the main load-carrying members and a matrix that keeps the fibers joined together, distributes loads, and protects the fibers from the external environment. Fibers are stiffer and stronger than the same material in bulk form. They could be longs or shorts with different properties and deposition techniques. Fibers are materials where the properties are maximized in a given direction and can be deposited with a chosen direction or in a random way. The matrix material usually is isotropic and homogeneous and could be polymeric or metallic depending on the applied load.

The most diffused fibers are carbon or glass but also graphite or boron can be used as fiber materi-

als. Long fibers are usually involved in the structural application and the better orientation angle was studied in the last years for every load condition. A representation of a laminate composed of two long fibers reinforced composite layers is reported in Figure 1.1 (b).

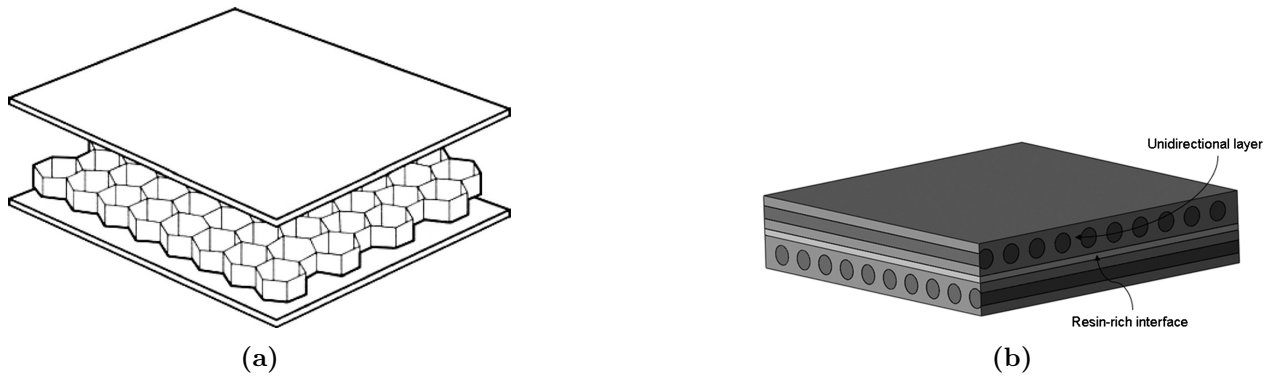


Figure 1.1: (a) Sandwich configuration with honeycomb core [1]. (b) Fiber reinforced composite laminate [2].

The introduction of a new class of composite material permits acting more on the angle orientation by changing the fiber deposition that will not be only straight. Variable angle tow (VAT) composite materials were introduced with the possibility of a fiber curvilinear path as clearly reported in Figure 1.2. Improving fiber path degrees of freedom leads to numerous advantages in structural efficiency improving the tailoring process and increasing the design space with an increase in the ratio of stiffness to mass. Due to the growing interest in the VAT class of material, a lot of surveys have been published during the last few years. Accurate stress studies of the VAT composite panels and shells, investigating the most accurate material theories, are mainly studied in [6] and [4]. Other studies are carried out to exploit the possibilities of the curvilinear fiber path studying the mechanical buckling and post-buckling behavior of VAT composite plate and numerous research have amply demonstrated the improvement in the buckling carrying capacity given to the use of VAT placement techniques compared to straight fibers deposition [7] [8].

Also, the well-established Carrera Unified Formulation was used for the investigation of the mechanical buckling and vibration analysis of VAT panels [9] [10].

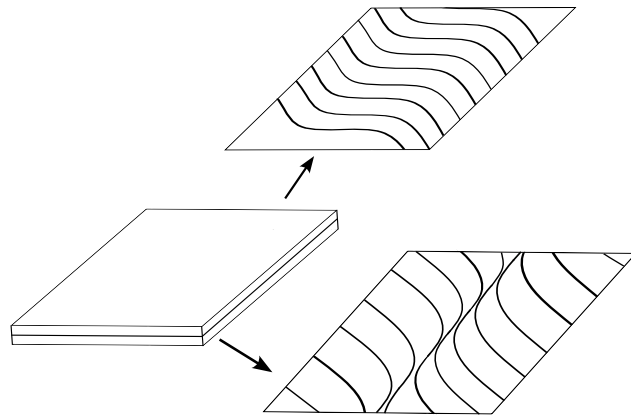


Figure 1.2: VAT laminate representation.

1.2 Thermal environment and thermal buckling

In the present thesis work, VAT composite plates are analyzed and the thermal buckling phenomenon is investigated to evaluate the buckling critical temperature. As explained, composite materials have superior strength and stiffness properties with respect to traditional materials but are often influenced by the environment. Those which involved an increase in material temperature induce expansion strains and the buckling critical load can be dramatically modified by the presence of an over-temperature. A thermal over-temperature acts on composite structures in usage and in manufacturing. Furthermore, structural composite materials are usually cured in an autoclave with high temperatures and pressure that can induce thermal stresses.

The thermal environment is present particularly for space applications where radiation heating is usually imposed on the structures and for high-speed aeronautical applications with a velocity of up to 2.2 Mach.

Using composite materials in space fields makes them subjected to an influential thermal environment. During the launch phase of a spacecraft, the thermal environment is maintained under moderate conditions and the maximum heating on the structure depends on the launch vehicle but is usually under control. After the first phase, the thermal environment has the most important effect on the structure, and considering a satellite, during its orbital life the thermal effect is the main applied load. The thermal conditions must not exceed the structural limits. Extreme conditions are influenced by the effect of solar radiation particularly when the orbital cycle causes a degradation in the thermal protection systems.

Composite materials can be used for different applications such as satellite structures in Lower Earth Orbit (LEO) where three sources of heating are present: the incoming solar radiation, Earth's infrared radiation, and the albedo, which is the solar radiation reflected by the Earth. Furthermore, there is great variability in the thermal condition of the structure considering its geographic position and the hour of the day.

In high-speed aircraft applications, the thermal environment is significant. The involved high speed induces heating on the structures and thermal consideration of the used material is necessary.

Considering thin structures such as panels, a thermal field can cause structure deflections and also

instability phenomena. Indeed, the plate can buckle under in-plane and compressive stresses that can be caused also by a thermal external load. Furthermore, in space structures, low tolerance is mandatory for some precision applications such as space telescopes.

Buckling is one of the principal modes of failure in thin structures such as plates and shells. It occurs with a sudden change in the plate/shell geometry at a critical load.

The term buckling is associated with an (observable) process whereby a given state of a deformable structure suddenly changes its shape. Brought about by a varying external load, this change in configuration often happens in a catastrophic way (i.e. the structure is destroyed at the end of the process). It may, however, also take place smoothly without causing permanent damage so that, when the external loading is removed, the structure can be restored to its original configuration. The change of shape observed during the buckling process is usually very pronounced and it occurs without a warning. Another important characteristic is that even in carefully monitored experiments, the beginning of failure (if it occurs) cannot be predicted with precision¹.

The study of the nonlinear response of flexible structures is a significant parameter for the investigation of thin plates because of their applications in numerous engineering fields and their influence on classical bending and instability problems. In the aerospace field, thin structures are frequently used particularly for the advantages in weight terms, and usually, instability phenomena occur first then static failures.

Over the years various works are done about the thermal buckling phenomena. Traditional metallic and composite materials are investigated under thermal load [11], and VAT buckling critical temperature is investigated with classical lamination theory and the finite element method in [12]. For FGMs, due to their applications, particular interest in thermal buckling is present [13] [14]. Also, anisotropic composite plates' free vibration response in a thermo-mechanical pre/post-buckled state is investigated in the CUF framework [15].

1.3 Present work overview

In the present work the Carrera Unified Formulation (CUF) is used to investigate the thermal critical buckling load of square VAT laminated plate and critical load and pre-buckling stresses are reported.

In Chapter 2 an introduction of the preliminary concepts necessary for the analyses schematization is explained. The constitutive equations are reported to allow an explanation of the multifield problem linking thermal and mechanical unknowns. Furthermore, the constitutive equations permit the definition of a relation between stresses and strains vector. Geometrical relations for the plate are reported using the Green-Lagrange tensor for non-linear problems and the main two-dimensional kinematic theories are illustrated. Finally, the difference between a coupled and decoupled approach is explained and the two formulations are reported by the use of the principle of virtual work.

In Chapter 3 the CUF framework used in the present analyses is reported for two-dimensional (2D) elements and the Q9 elements are selected for the analyses. The main expansion functions for the problem formulation are reported and High Order Theories (HOT) are explicated choosing the Lagrange Expansion (LE) functions combined with the Layer Wise (LW) approach. Fundamental Nuclei (FN) are obtained and reported for static, thermo-mechanical, and buckling problems.

In Chapter 4 the main mathematical approaches used for the material modelization are reported and the LW model is chosen for the present formulation. Furthermore, some considerations about the differences between straight fibers and VAT material rotation approaches are reported.

¹Definition taken from: E. Riks, "Buckling" Encyclopedia of Computational Mechanics, Vol 2, 2004 [19]

After the theoretical introduction, some validation results are presented. In Chapter 5 some analyses on traditional laminated material are carried out. In section 5.1.1 a simply supported square plate composed of isotropic layers is analyzed with a coupled analysis. The validation of the calculated thermal profile is reported with respect to the reference [3]. Moreover, convergence analysis is presented to choose the better discretization both in-plane and along the thickness, and relative stresses are represented. Following, in section 5.2 the thermo-elastic analysis is done for a carbon fiber reinforced composite laminate, and stress results are reported. Both, decoupled (5.2.1) and coupled (5.2.2) approaches are used to define their differences and choose the suitable approach for the after-analyses. Furthermore, the results are validated with 3D ABAQUS analyses.

Finally, in Chapter 6 VAT laminated are studied. Validation analyses for mechanical and thermo-buckling problems are reported comparing the present results with respect to the literature [4], [12]. The maximum critical buckling temperature varying the lamination angles is investigated. In the end, some comparisons between the better and the worst cases for the thermal buckling problem are done for Carbon/Epoxy and E-Glass/Epoxy symmetric plates.

Chapter 2

Preliminary concepts

The following chapter describes the preliminary concept necessary to understand the modelization of the problem that has to be solved. Considering a three-dimensional body the present work uses kinematic assumption to analyze the simplest 2D model. The geometrical equations make explicit the relationship between strains and displacements. Constitutive equations permit the description of the stresses by the definition of the strain. Furthermore, they are necessary to define the relationship between the mechanical and thermal fields.

Moreover, the thermo-mechanical problem is described in two main used ways: the decoupled and the coupled approaches.

2.1 Constitutive relations

The Constitutive equations for the multi-field problem are developed considering the free Gibbs energy per unit of volume G , the dissipation function F and the thermodynamic enthalpy density H . Considering the thermomechanical field, the involved variables are the increment in temperature with respect to a reference temperature θ , the strains ϵ , and the thermal gradient ϑ [16] [3].

$$G(U, \theta, \epsilon) = U - \theta\eta + \sigma_{ij}\epsilon_{ij} \quad (2.1)$$

$$F(\vartheta) = \frac{1}{2}k_{ij}\theta_i\theta_j - \tau_0\dot{q}_i \quad (2.2)$$

where \dot{q} indicates the temporal derivate of the heat flux. τ_0 is the thermal relaxation parameter; U is the internal energy per unit of volume; σ_{ij} is the stress tensor; η is the variation of entropy per unit of volume; k_{ij} is the thermal conductivity tensor. If stationary fluxes are considered boundary conditions, the flux can be set to zero. The thermodynamic enthalpy density is defined as:

$$H(U, \theta, \epsilon, \vartheta) = G - F \quad (2.3)$$

By substituting eq. 2.1 and 2.2 in the 2.3 it is possible to express the thermodynamic enthalpy as:

$$H(U, \theta, \epsilon, \vartheta) = U - \theta\eta + \sigma_{ij}\epsilon_{ij} - \frac{1}{2}k_{ij}\vartheta_i\vartheta_j. \quad (2.4)$$

Considering the variables it is possible to write H in a quadratic form using both, the Gibbs free energy and the dissipation function.

$$H = \frac{1}{2} \left(\theta^2 \frac{\partial^2 H}{\partial \theta^2} + \epsilon_{ij}\epsilon_{lm} \frac{\partial^2 H}{\partial \epsilon_{ij} \partial \epsilon_{lm}} + \theta\epsilon_{lm} \frac{\partial H^2}{\partial \epsilon_{lm} \partial \theta} + \theta\epsilon_{ij} \frac{\partial H^2}{\partial \epsilon_{ij} \partial \theta} - k_{ij}\vartheta_i\vartheta_j \right) \quad (2.5)$$

For the sake of simplicity, some coefficients can be defined as follow.

$$\chi = \frac{C\rho}{\theta_{ref}} = - \left[\frac{\partial^2 H}{\partial \theta^2} \right] \quad (2.6)$$

$$C_{ijlm} = \left[\frac{\partial^2 H}{\partial \epsilon_{ij} \partial \epsilon_{lm}} \right] \quad (2.7)$$

$$\lambda_{ij} = - \left[\frac{\partial H^2}{\partial \epsilon_{ij} \partial \theta} \right] \quad (2.8)$$

where: χ is only use for clarity of notation and is defined above. ρ is the matherial density, C is the specific heat per unit mass. θ_{ref} is the references temperature used for θ definition, C_{ijlm} indicates the elastic coefficient of the Hook law, λ_{ij} is the stresses-temperature coefficient which coupled the two fields.

It is possible to write the eq. 2.5 replacing the defined coefficients.

$$H = -\frac{1}{2}\theta^2\chi + \frac{1}{2}\epsilon_{ij}\epsilon_{lm}C_{ijlm} - \theta\epsilon_{ij}\lambda_{ij} \quad (2.9)$$

Considering the exact differential of H:

$$dH = -\eta d\theta + \sigma_{ij}d\epsilon_{ij} - q_i d\vartheta_i \quad (2.10)$$

It is now possible to write the constitutive equations:

$$\eta = - \left[\frac{\partial H}{\partial \theta} \right] = \chi\theta + \epsilon_{ij}\lambda_{ij} \quad (2.11)$$

$$\sigma_{ij} = \left[\frac{\partial H}{\partial \epsilon_{ij}} \right] = \epsilon_{lm}C_{ijlm} - \theta\lambda_{ij} \quad (2.12)$$

$$q_i = - \left[\frac{\partial H}{\partial \vartheta} \right] = k_{ij}\vartheta_j \quad (2.13)$$

The coupling functions λ_{ij} relate thermal and mechanic behavior. In the present section, with some thermodynamic considerations, the constitutive equations for the thermo-mechanical problem have been obtained. Following the constitutive relations will be used in the principle of virtual work to obtain a global description of the structural problem.

The thermo-mechanical problem can be described in two main ways. It can be analyzed in a decoupled or coupled manner. In the first case, the thermal contribution is calculated by a dedicated relation such as the Fourier equation or a linear assumption profile and it is considered as an external load. Instead, the coupled analysis considers the temperature as a variable of the problem. In a fully coupled study, Hooke's law considers both strain and temperature as unknowns, and the mutual influence between thermal and mechanical fields is considered.

Decoupled approach

In a partial coupling approach, only equation number 2.12 is considered and the temperature profile is defined using the Fourier law or axiomatic approach, so in the decoupled case, temperature affects stresses but not vice versa. Moreover, the temperature is only seen as an external load whose evolution is known. The decoupled study has some advantages in terms of simplicity and reduction

of the variables number. On the other hand, the temperature must be known at any point of the structure.

The expression of strains and stresses vector is defined as follows:

$$\boldsymbol{\varepsilon}^T = \{\epsilon_{xx} \ \epsilon_{yy} \ \epsilon_{zz} \ \epsilon_{xz} \ \epsilon_{yz} \ \epsilon_{xy}\} \quad (2.14)$$

$$\mathbf{S}^T = \{\sigma_{xx} \ \sigma_{yy} \ \sigma_{zz} \ \sigma_{xz} \ \sigma_{yz} \ \sigma_{xy}\} \quad (2.15)$$

It is worthwhile to decompose strain as the sum of mechanical and thermal components and indicate them by different subscripts, m indicates the mechanical component and θ the thermal one.

$$\{\varepsilon\} = \{\varepsilon_m\} + \{\varepsilon_\theta\} = \{\varepsilon_m\} - \{\alpha\}\theta \quad (2.16)$$

$$\{S\} = \mathbf{C}\{\varepsilon\} = \mathbf{C}(\{\varepsilon\}_m + \{\varepsilon_\theta\}) = \mathbf{C}\{\varepsilon_m\} - \mathbf{C}\{\alpha\}\theta = \mathbf{C}\{\varepsilon_m\} - \boldsymbol{\lambda}\theta = \{S_m\} + \{S_\theta\} \quad (2.17)$$

where α is the thermal expansion coefficient. With these considerations, it is possible to obtain the same results as equation 2.12 and clearly, divide the expression into the two components. It is to be noted that, thermal conductivities are neglected at the moment. The matrices are shown below, the material is considered to be orthotropic, homogeneous, and operating in the linear elastic range. It must be noted that the constitutive relation and the thermal conductivity are expressed in the local reference system.

$$\mathbf{C} = \begin{pmatrix} C_{11} & C_{12} & C_{13} & 0 & 0 & 0 \\ C_{21} & C_{22} & C_{23} & 0 & 0 & 0 \\ C_{31} & C_{32} & C_{33} & 0 & 0 & 0 \\ 0 & 0 & 0 & C_{44} & 0 & 0 \\ 0 & 0 & 0 & 0 & C_{55} & 0 \\ 0 & 0 & 0 & 0 & 0 & C_{66} \end{pmatrix} \quad (2.18)$$

$$\boldsymbol{\lambda}^T = \{\lambda_1 \ \lambda_2 \ \lambda_3 \ 0 \ 0 \ 0\} \quad (2.19)$$

With the eq. 2.18,2.19 the constitutive material coefficients for the mechanical and thermal problem are separately defined.

Coupled approach

As mentioned above, a coupled approach considers the over-temperature θ as a variable of the problem. The solution is reached when the equilibrium between the two mutually influenced fields, is found. In the coupled case, both the constitutive eq.s 2.11 and 2.12 are still used. Stresses and strain vectors are changed with respect to the previous case and represented below. The thermal component is added in both vectors.

$$\boldsymbol{\varepsilon}^T = \{\epsilon_{xx} \ \epsilon_{yy} \ \epsilon_{zz} \ \epsilon_{xz} \ \epsilon_{yz} \ \epsilon_{xy} \ \theta\} \quad (2.20)$$

$$\mathbf{S}^T = \{\sigma_{xx} \ \sigma_{yy} \ \sigma_{zz} \ \sigma_{xz} \ \sigma_{yz} \ \sigma_{xy} \ -\eta\} \quad (2.21)$$

In the coupled case constitutive relation between strains and stresses can be explained by the use of a matrix \mathbf{C} as follows:

$$\mathbf{S} = \mathbf{C}\boldsymbol{\varepsilon} \quad (2.22)$$

$$\mathbf{C} = \begin{pmatrix} C_{11} & C_{12} & C_{13} & 0 & 0 & 0 & -\lambda_1 \\ C_{21} & C_{22} & C_{23} & 0 & 0 & 0 & -\lambda_2 \\ C_{31} & C_{32} & C_{33} & 0 & 0 & 0 & -\lambda_3 \\ 0 & 0 & 0 & C_{44} & 0 & 0 & 0 \\ 0 & 0 & 0 & 0 & C_{55} & 0 & 0 \\ 0 & 0 & 0 & 0 & 0 & C_{66} & 0 \\ -\lambda_1 & -\lambda_2 & -\lambda_3 & 0 & 0 & 0 & -\chi \end{pmatrix} \quad (2.23)$$

It has to be noted that, in the coupled case there is an increase in the unknowns number, as consequence the dimensions of the constitutive matrix change from 6 x 6 to 7 x 7. Furthermore, a new coefficient is present linking the thermal field with itself. The matrices 2.23 2.18 and vector 2.19 are referred to the local reference system and must be rotated as described in the chapter 4 and represented in the eq.s 4.3, 4.4, 4.6.

2.2 Geometrical relations

In the following section, the geometrical relations are defined for a plate. As clear from the name, the geometrical relations depend on the considering geometry, and in the case of a 2D model plate or shell, relations can be defined. Considering the present work where a plate is analyzed, following only the plate geometrical relations are reported. The geometrical relations can be simplified depending on the analyzed problem field, usually, the first-order geometrical operator is used but in the case of non-linear problems, such as buckling ones the second-order geometrical link is necessary. Through the geometrical relations, a differential operator links vector $\boldsymbol{\varepsilon}$ and primary variables \mathbf{U} .

Decoupled approach

In the case of a decoupled approach, primary variables coincide with displacements which vector is represented below:

$$\mathbf{U}^T = (u \ v \ w) \quad (2.24)$$

the variables $\boldsymbol{\varepsilon}$ are directly obtained from the unknowns \mathbf{U} by the differential operator \mathbf{b} .

$$\boldsymbol{\varepsilon} = \mathbf{b}\mathbf{U} \quad (2.25)$$

$$\mathbf{b} = \begin{pmatrix} \frac{\partial}{\partial x} & 0 & 0 \\ 0 & \frac{\partial}{\partial y} & 0 \\ 0 & 0 & \frac{\partial}{\partial z} \\ \frac{\partial}{\partial z} & 0 & \frac{\partial}{\partial x} \\ 0 & \frac{\partial}{\partial z} & \frac{\partial}{\partial y} \\ \frac{\partial}{\partial y} & \frac{\partial}{\partial x} & 0 \end{pmatrix} \quad (2.26)$$

where the operator \mathbf{b} represents the first-order link between strain and displacements.

For buckling description, which is the purpose of the present investigation, it is extremely necessary to use the Green-Lagrange tensor which is a quadratic operator. Taking into account high-order terms of finite displacement, in the geometrical relations it is possible to evaluate the nonlinear

response and the stresses distributions. The relation remains the same but the tensor \mathbf{b} changes as follows:

$$\mathbf{b} = \begin{pmatrix} \frac{\partial}{\partial x} + \frac{1}{2} \left(\frac{\partial}{\partial x} \right)^2 & \frac{1}{2} \left(\frac{\partial}{\partial x} \right)^2 & \frac{1}{2} \left(\frac{\partial}{\partial x} \right)^2 \\ \frac{1}{2} \left(\frac{\partial}{\partial y} \right)^2 & \frac{\partial}{\partial y} + \frac{1}{2} \left(\frac{\partial}{\partial y} \right)^2 & \frac{1}{2} \left(\frac{\partial}{\partial y} \right)^2 \\ \frac{1}{2} \left(\frac{\partial}{\partial z} \right)^2 & \frac{1}{2} \left(\frac{\partial}{\partial z} \right)^2 & \frac{\partial}{\partial z} + \frac{1}{2} \left(\frac{\partial}{\partial z} \right)^2 \\ \frac{\partial}{\partial z} + \frac{\partial}{\partial x} \frac{\partial}{\partial z} & \frac{\partial}{\partial x} \frac{\partial}{\partial z} & \frac{\partial}{\partial x} + \frac{\partial}{\partial x} \frac{\partial}{\partial z} \\ \frac{\partial}{\partial y} \frac{\partial}{\partial z} & \frac{\partial}{\partial z} + \frac{\partial}{\partial y} \frac{\partial}{\partial z} & \frac{\partial}{\partial y} + \frac{\partial}{\partial y} \frac{\partial}{\partial z} \\ \frac{\partial}{\partial y} + \frac{\partial}{\partial x} \frac{\partial}{\partial y} & \frac{\partial}{\partial x} + \frac{\partial}{\partial x} \frac{\partial}{\partial y} & \frac{\partial}{\partial x} \frac{\partial}{\partial y} \end{pmatrix} \quad (2.27)$$

For the sake of simplicity, it is possible to split the tensor in the sum of linear and non-linear differential operators as follows.

$$\mathbf{b}_l = \begin{pmatrix} \frac{\partial}{\partial x} & 0 & 0 \\ 0 & \frac{\partial}{\partial y} & 0 \\ 0 & 0 & \frac{\partial}{\partial z} \\ \frac{\partial}{\partial z} & 0 & \frac{\partial}{\partial x} \\ 0 & \frac{\partial}{\partial z} & \frac{\partial}{\partial y} \\ \frac{\partial}{\partial y} & \frac{\partial}{\partial x} & 0 \end{pmatrix} \quad \mathbf{b}_{nl} = \begin{pmatrix} \frac{1}{2} \left(\frac{\partial}{\partial x} \right)^2 & \frac{1}{2} \left(\frac{\partial}{\partial x} \right)^2 & \frac{1}{2} \left(\frac{\partial}{\partial x} \right)^2 \\ \frac{1}{2} \left(\frac{\partial}{\partial y} \right)^2 & \frac{1}{2} \left(\frac{\partial}{\partial y} \right)^2 & \frac{1}{2} \left(\frac{\partial}{\partial y} \right)^2 \\ \frac{1}{2} \left(\frac{\partial}{\partial z} \right)^2 & \frac{1}{2} \left(\frac{\partial}{\partial z} \right)^2 & \frac{1}{2} \left(\frac{\partial}{\partial z} \right)^2 \\ \frac{\partial}{\partial x} \frac{\partial}{\partial z} & \frac{\partial}{\partial x} \frac{\partial}{\partial z} & \frac{\partial}{\partial x} \frac{\partial}{\partial z} \\ \frac{\partial}{\partial y} \frac{\partial}{\partial z} & \frac{\partial}{\partial y} \frac{\partial}{\partial z} & \frac{\partial}{\partial y} \frac{\partial}{\partial z} \\ \frac{\partial}{\partial x} \frac{\partial}{\partial y} & \frac{\partial}{\partial x} \frac{\partial}{\partial y} & \frac{\partial}{\partial x} \frac{\partial}{\partial y} \end{pmatrix} \quad (2.28)$$

where $\partial()/\partial(x, y, z)$ denotes the partial derivative. The equation 2.25 becomes:

$$\boldsymbol{\varepsilon} = (\mathbf{b}_l + \mathbf{b}_{nl}) \mathbf{U} \quad (2.29)$$

Coupled approach

In a coupled approach also temperature is a primary variable and the vector \mathbf{U} is:

$$\mathbf{U}^T = (u \ v \ w \ \theta) \quad (2.30)$$

The second-order split tensor is reported below, the only difference from the previous case is the presence of the link between the thermal field and itself. As clear from Matrix 2.31 the thermal link remains linear also in a non-linear analysis.

$$\mathbf{b}_l = \begin{pmatrix} \frac{\partial}{\partial x} & 0 & 0 & 0 \\ 0 & \frac{\partial}{\partial y} & 0 & 0 \\ 0 & 0 & \frac{\partial}{\partial z} & 0 \\ \frac{\partial}{\partial z} & 0 & \frac{\partial}{\partial x} & 0 \\ 0 & \frac{\partial}{\partial z} & \frac{\partial}{\partial y} & 0 \\ \frac{\partial}{\partial y} & \frac{\partial}{\partial x} & 0 & 0 \\ 0 & 0 & 0 & 1 \end{pmatrix} \quad \mathbf{b}_{nl} = \begin{pmatrix} \frac{1}{2} \left(\frac{\partial}{\partial x} \right)^2 & \frac{1}{2} \left(\frac{\partial}{\partial x} \right)^2 & \frac{1}{2} \left(\frac{\partial}{\partial x} \right)^2 & 0 \\ \frac{1}{2} \left(\frac{\partial}{\partial y} \right)^2 & \frac{1}{2} \left(\frac{\partial}{\partial y} \right)^2 & \frac{1}{2} \left(\frac{\partial}{\partial y} \right)^2 & 0 \\ \frac{1}{2} \left(\frac{\partial}{\partial z} \right)^2 & \frac{1}{2} \left(\frac{\partial}{\partial z} \right)^2 & \frac{1}{2} \left(\frac{\partial}{\partial z} \right)^2 & 0 \\ \frac{\partial}{\partial x} \frac{\partial}{\partial z} & \frac{\partial}{\partial x} \frac{\partial}{\partial z} & \frac{\partial}{\partial x} \frac{\partial}{\partial z} & 0 \\ \frac{\partial}{\partial y} \frac{\partial}{\partial z} & \frac{\partial}{\partial y} \frac{\partial}{\partial z} & \frac{\partial}{\partial y} \frac{\partial}{\partial z} & 0 \\ \frac{\partial}{\partial x} \frac{\partial}{\partial y} & \frac{\partial}{\partial x} \frac{\partial}{\partial y} & \frac{\partial}{\partial x} \frac{\partial}{\partial y} & 0 \\ 0 & 0 & 0 & 0 \end{pmatrix} \quad (2.31)$$

2.3 Principle of Virtual Displacements, PVD

The variational principles permit to write the governing equations of the problem and the relative boundary conditions. The Principle of Virtual Displacements (PVD) involves only a compatible displacement field. Considering a set of admissible configurations, a virtual variation on the displacement is applied and the only congruent and balanced configuration is reached. The PVD can be derived from the Hamilton principle which considers an energy balance of conservative forces without dissipation.

$$\delta \int_{t_0}^t (K - \Pi) dt = 0 \quad \implies \quad \delta \int_{t_0}^t K dt - \delta \int_{t_0}^t \Pi dt = 0 \quad (2.32)$$

where K is the kinetic energy and Π is the potential energy. δ is the variational operator and t is the time. For the sake of simplicity, the two terms are separately treated.

$$\begin{aligned} \delta \int_{t_0}^t K dt &= \delta \int_{t_0}^t \int_V \frac{1}{2} \rho \dot{u}_i \dot{u}_i dV dt = \int_{t_0}^t \int_V \rho \dot{u}_i \delta \dot{u}_i dV dt = \\ &= - \int_{t_0}^t \int_V \rho \ddot{u}_i \delta u_i dV dt + \int_S \rho \dot{u}_i \delta u_i dV dt \Big|_{t_0}^{t_1} \end{aligned} \quad (2.33)$$

where, integrating per part we obtain two terms. The first is on the domain, the latter consists of a boundary condition which is zero because δu is zero both in $t = t_0$ and $t = t_1$, so that:

$$\delta \int_{t_0}^t K dt = - \delta \int_{t_0}^t \int_V \rho \ddot{u}_i \delta u_i dV dt = - \int_{t_0}^t \delta L_{ine} dt \quad (2.34)$$

where δL_{ine} is the variation of the inertial work. If a stationary study is conducted, inertial work term is zero.

Furthermore, the variation of potential energy is written as a sum of the variation of the thermodynamic enthalpy density and the work done by applied external loads.

$$\delta \int_{t_0}^t \Pi dt = \delta \int_{t_0}^t \left[\int_V H dV - \int_A f_{jext} u_j dA \right] dt = \delta \int_{t_0}^t \int_V H dV dt - \int_{t_0}^t \delta L_{ext} dt \quad (2.35)$$

where f_{ext} are the external forces acting in j direction on the surface A . For the sake of simplicity only surfaces forces are considered but it is possible to add also the work done by volumes and/or thermal loads. δL_{ext} is the variation of the work done by the external loads.

Decoupled approach

In a decoupled approach, the expansion with respect to the primary variables of the enthalpy expression is the following. The equation is simplest than the coupled one, the disadvantage is that the thermal effect due to strain is neglected and the temperature has to be imposed at any point of the continuum as a known factor.

$$\begin{aligned} \delta \int_{t_0}^t \int_V H dV dt &= \int_{t_0}^t \int_V \left(\frac{\partial H}{\partial \theta} \delta \theta + \frac{\partial H}{\partial \epsilon} \delta \epsilon \right) dV dt = \int_{t_0}^t \int_V \delta \epsilon_m^T (\epsilon_m \mathbf{C} - \theta \lambda) dV dt = \\ &= \int_{t_0}^t \int_V \delta \epsilon_m^T (\mathbf{S}_m + \mathbf{S}_\theta) dV dt = \int_{t_0}^t \int_V \delta \epsilon_m^T \mathbf{S} dV dt = \int_{t_0}^t \delta L_{int} dt \end{aligned} \quad (2.36)$$

Thermodynamic enthalpy density expression is shown in the equation 2.5. In a decoupled approach, the derivative with respect to the temperature is zero because θ is not a variable, and the stress expressed in the eq. 2.12, is the only term that remains not null. As shown in the eq. 2.36, the virtual variation is applied only to the mechanical part of strains because the thermal part is considered known. The equation 2.32, for a steady state, can be written as follow:

$$\delta L_{int} = \delta L_{ext} \quad (2.37)$$

In the decoupled study, substituting the terms at the end of the equation 2.36 with the geometric and constitutive equations, thermal contribution becomes an external load.

$$\begin{aligned} \delta L_{int} &= \int_V \delta \epsilon_m^T \mathbf{S} dV = \int_V \delta \epsilon_m^T (\mathbf{S}_m + \mathbf{S}_\theta) dV = \int_V \delta \epsilon_m^T (\mathbf{C} \epsilon_m - \lambda \theta) dV = \int_V \delta \epsilon_m^T \mathbf{C} \epsilon_m dV + \\ &\quad - \int_V \delta \epsilon_m^T \lambda \theta dV = \int_V (\mathbf{b} \delta \mathbf{U})^T \mathbf{C} \mathbf{b} \mathbf{U} dV - \int_V (\mathbf{b} \delta \mathbf{U})^T \lambda \theta dV = \int_A \delta \mathbf{U}^T f_{ext} dA = \delta L_{ext} \end{aligned}$$

If an approximated resolution method, such as the Finite Element Method (FEM), is selected, displacements became independent from the volume and can be extracted from the integral. Therefore, the thermal effect introduced by the constitutive equations can be considered as an external load where all the terms are known.

$$\int_V (\mathbf{b} \delta \mathbf{U})^T \mathbf{C} \mathbf{b} \mathbf{U} dV = \int_V (\mathbf{b} \delta \mathbf{U})^T \lambda \theta dV + \int_V \delta \mathbf{U}^T f_{ext} dA \quad (2.38)$$

In a decoupled approach, as clear, the thermal contribution is considered as an external load whose profile along the thickness is known a priori. Hypothesizing that the temperature immediately

reaches the equilibrium configuration there are various approaches to describe the path along the thickness. The choice of one or other thickness description is due to material properties such as thermal conductivity and plate thickness. The profile can be assumed constant along the thickness, with the same temperature value at each point or with a variable shape following some different rules [5].

The more accurate analysis uses a temperature profile that changes along the thickness, and the profile can be a priori assumed linear or calculated using the Fourier equation. For thin plates the temperature profile may be assumed almost linear, conversely, for thick plates, the temperature behavior is very far from the linear one, and large errors can be committed if the temperature profile is assumed as linear. For a constant temperature profile, the temperature determination at each layer is obvious. More interesting is an assumed linear profile that is described by the following equation, where the value of the temperature at the bottom and top of the plate is known and equal to the imposed temperature, θ_{bottom} and θ_{top} indicate the imposed over-temperature with respect to the reference temperature, h is the thickness of the plate.

$$\theta(z) = \theta_{bottom} + \frac{\theta_{top} - \theta_{bottom}}{h} \cdot \left(z + \frac{h}{2} \right) \quad z \in \left[-\frac{h}{2}, \frac{h}{2} \right] \quad (2.39)$$

Independent of the number of layers and material composition the temperature trend is the same when an assumed profile is used.

By solving the Fourier heat conduction equation a more realistic profile is used. In the case of multilayered structures, it is necessary to solve the equation for each layer separately. Considering the generic layer k , the equation is the following.

$$K_1^k \frac{\partial^2 \theta}{\partial x^2} + K_2^k \frac{\partial^2 \theta}{\partial y^2} + K_3^k \frac{\partial^2 \theta}{\partial z^2} = 0 \quad (2.40)$$

where K_1^k K_2^k K_3^k are the thermal conductivity coefficients of the layer k material. It is necessary to impose the thermal continuity at each interface:

$$\theta_{bottom}^{k+1} = \theta_{top}^k \quad for \quad k = 1, \dots, N_l - 1 \quad (2.41)$$

Coupled approach

Considering the coupled case, the enthalpy expression expansion changes and, the use of the equation 2.11 makes possible extensive variable concerning thermal field (entropy) introduction into the equation with θ as a primary variable. Considering a coupled approach, a division of the thermal and mechanical strain/stress components is not possible because the elements influence each other.

$$\begin{aligned} \delta \int_{t_0}^t \int_V H dV dt &= \int_{t_0}^t \int_V \left(\frac{\partial H}{\partial \theta} \delta \theta + \frac{\partial H}{\partial \epsilon} \delta \epsilon \right) dV dt = \\ &= \int_{t_0}^t \int_V (-\eta \delta \theta + (\epsilon_{lm} C_{ijlm} - \theta \lambda_{ij}) \delta \epsilon) dV dt = \int_{t_0}^t \int_V (-\eta \delta \theta + \delta \epsilon^T \boldsymbol{\sigma}) dV dt = \\ &= \int_{t_0}^t \int_V \delta \boldsymbol{\epsilon}^T \mathbf{S} dV dt = \int_{t_0}^t \delta L_{int} dt \quad (2.42) \end{aligned}$$

Introducing the constitutive and geometrical relations and the equality between external and internal load, the equation became as follows.

$$\int_{t_0}^t \delta L_{int} dt = \int_V (\mathbf{b} \delta \mathbf{U})^T \mathbf{C} \mathbf{b} \mathbf{U} dV = \int_A \delta \mathbf{U}^T f_{ext} dA = \int_{t_0}^t \delta L_{ext} dt \quad (2.43)$$

2.4 Plate theories

In mechanics, the plate theories allow the behavior description of structures characterized by one dimension, which is typically the thickness, at least one order of magnitude lower than the in-plane dimensions. The plate theories permit simplifying the problem from a three-dimensional (3D) to a two-dimensional (2D) one, eliminating the unknown ' z ' dependence (where ' z ' is the thickness direction). The ' z ' behavior can be made explicit by the use of several methodologies such as asymptotic or axiomatic approaches. For the latter, the distribution along the thickness will be expressed by a polynomial expansion in the ' z ' direction. Various theories have been developed for the expansion, using different assumptions and approaches. Linear expansion is given by classical theories such as the Classical laminated theory (CLT) or the First Shear Deformation Theory (FSDT), higher-order models can provide more accurate solutions obviously with a higher computational cost [17]. The Carrera Unified Formulation (CUF) can collect all the different expansions orders models with an indicial wording. More details are available in [18] and are explained in Chapter 3. The plate geometry is represented in Figure 2.1 to allow the theory explanation.

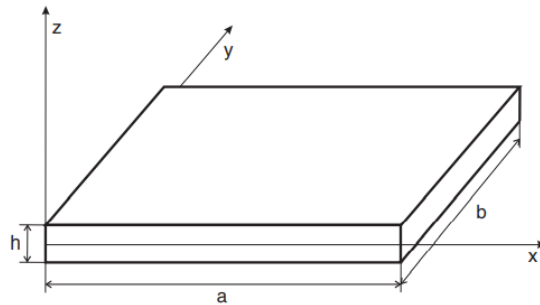


Figure 2.1: *Plate geometry and references system.*

2.4.1 Kirchhoff plate theory

The Kirchhoff plate theory allows us to describe the behavior of thin plates where shear slides are neglected. The three-dimensional behavior is reduced to a two-dimensional one by the introduction of some kinematic hypotheses.

- There is not strain in the thickness direction which means there is not elongation.
- Plane sections normal to the reference surface remain plane after deformation, implying that the displacement can be expressed through a translation and rotation.
- The transverse normals rotate remaining perpendicular to the middle-surface after deformation, which means there shear deformations γ_{xz} γ_{yz} are disregarded.
- The normal stress through the thickness are ignored which is a plane-stress condition.

The present theory whose hypotheses are explained is implemented in the numerical codes as CLT. The kinematic field is the following:

$$\begin{cases} u(x, y, z) = u^0(x, y) - zu_{,x}(x, y) \\ v(x, y, z) = v^0(x, y) - zv_{,y}(x, y) \\ w(x, y, z) = w^0(x, y) \end{cases} \quad (2.44)$$

where the subscript $,x$ indicates the derivative with respect to x . u^0 v^0 w^0 are the displacements on the plate reference surface, typically as reference the surface is considered the middle one. The kinematics terms are reported in Figure 2.2.

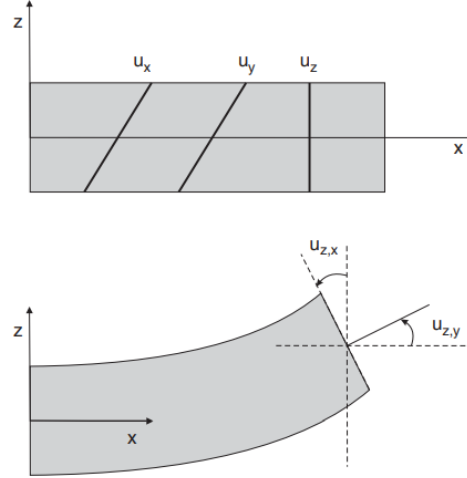


Figure 2.2: *Distribution of displacements in Classical Plate Theory.*

In the CLT theory rotations are linked to the translations by derivative. The approach permits simplifies the problem by reducing the degrees of freedom without expanding the principal variables. On the other hand, the derivation degree of the equations describing the problem increases, and, with the FEM approach the shape functions are more complex.

2.4.2 Reissner Mindlin plate theory

The Reissner Mindlin plate theory is a classical theory useful to describe the behavior of a thin plate/relatively thick plate. The introduced hypotheses are the follows:

- There is not strain in the thickness direction which means thickness remains constant during deformation.
- Plane sections normal to the reference surface remain plane after deformation, this implies the displacement can be expressed through a translation and rotation.
- Plane-stress condition.

The kinematic field is schematized by means of the following five independents variables u^0 v^0 w^0 ϕ_x ϕ_y which are reported in Figure 2.3 and consider also the in-plane shear strains with a first-order expansion.

$$\begin{cases} u(x, y, z) = u^0(x, y) + z\phi_x(x, y) \\ v(x, y, z) = v^0(x, y) + z\phi_y(x, y) \\ w(x, y, z) = w^0(x, y) \end{cases} \quad (2.45)$$

The Reissner Mindlin plate theory is implemented in shell finite elements by all the commercial codes called FSDT.

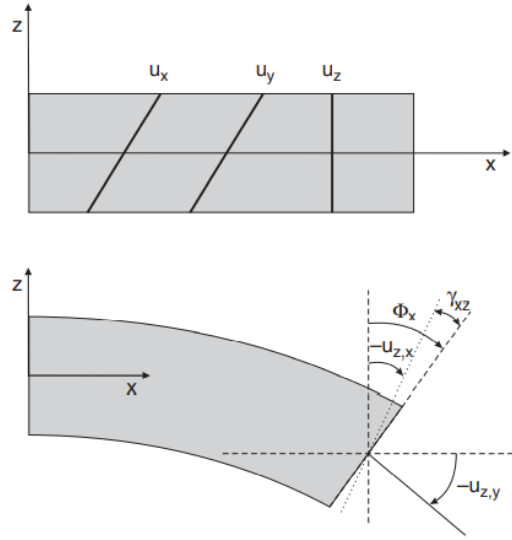


Figure 2.3: *Distribution of displacements in First shear deformation theory.*

In the FSDT considering relatively thick plates, the description is more accurate than in CLT. Using the FEM method the FSDT theory is preferred over the CLT for the lower derivation order of the equilibrium equations.

2.4.3 High Order Theories (HOT)

High Order Theories (HOT) describe the in ' z ' behavior by the use of different expansions with different complexity and computational cost level. CLT and FSDT are the simplest theories that describe the kinematics of two-dimensional problems. Refined theories can represent kinematics better and can not require correction factors. Furthermore, classical theories reached more problems in the description of thick plates and shells. The order of expansion can be changed considering the case problem using only the necessary terms.

Different expansion functions can describe displacement fields and the two most used functions are the Taylor Expansion (TE) and the Lagrange Expansion (LE).

Taylor Expansion (TE)

The Taylor polynomial Expansions (TE) use a complete model to describe the trough-the-thickness displacement field. The expansion order is indicated as N . For instance, the second-order model ($N=2$) describes a parabolic displacement field and is represented below.

$$\begin{aligned}
 u(x, y, z) &= u_0(x, y) \parallel + zu_1(x, y) \parallel + z^2u_2(x, y) \\
 v(x, y, z) &= v_0(x, y) \parallel + zv_1(x, y) \parallel + z^2v_2(x, y) \\
 w(x, y, z) &= \underbrace{w_0(x, y)}_{N=0} \parallel + \underbrace{zw_1(x, y)}_{N=1} \parallel + \underbrace{z^2w_2(x, y)}_{N=2}
 \end{aligned} \tag{2.46}$$

With an $N=2$ Taylor expansion, the displacement field has nine two-dimensional variables. The same procedure can be used for higher expansion orders such as the fourth, fifth, or, N th orders. A representation of the different order displacement field is represented below in Fig. 2.4.

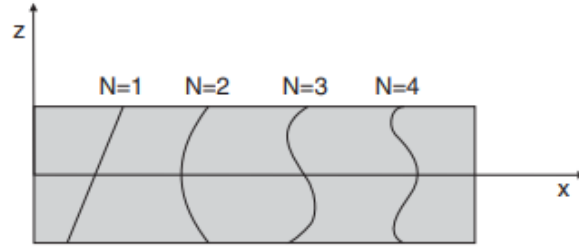


Figure 2.4: *Distribution of displacements for different orders of expansion.*

Lagrange Expansion (LE)

The second class of models for plates is based on Lagrange polynomials and are called Lagrange Expansion (LE) and have two principal features:

- The variables and boundary conditions can be imposed above the physical surfaces of the structures.
- The unknown are the components of the displacement which do not include rotations and high-order variables.

As said, the two-dimension model considers, typically, a reference surface and the variables are defined above the surface. Instead with the Lagrange model, the behavior is defined on the top and bottom surfaces of the structures and it is possible to apply the Boundary Conditions (BCs) to pure displacement components. Furthermore, in a multilayered structure the Layer-Wise (LW) approach, described in Chapter 4, assumes the use of the LW model which can be easily imposed. The Lagrange kinematic assumption is above described.

$$\begin{cases} u(x, y, z) = F(z)_t u_t(x, y) + F(z)_b u_b(x, y) \\ u(x, y, z) = F(z)_t u_t(x, y) + F(z)_b u_b(x, y) \\ u(x, y, z) = F(z)_t u_t(x, y) + F(z)_b u_b(x, y) \end{cases} \quad (2.47)$$

where $F(z)$ indicates the Lagrange Expansion function, and the subscripts b and t represent the displacement components at the bottom and top of the layer.

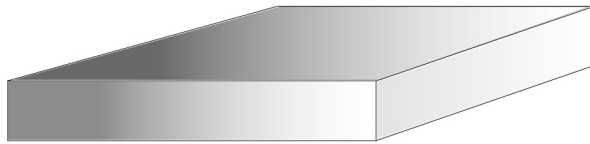
For the sake of clarity, it is preferred to use a natural coordinate system, therefore the $F(z)$ functions have the same description for all the cases.

$$F(\zeta)_t = \frac{1 + \zeta}{2} \quad (2.48)$$

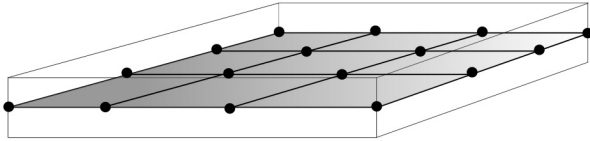
$$F(\zeta)_b = \frac{1 - \zeta}{2} \quad (2.49)$$

with Lagrange Expansion, it is possible to impose BCs on the bottom and top displacements to guarantee compatibility conditions.

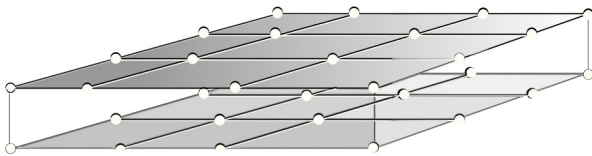
Figure 2.5 represents the main differences between the various kinematic approaches. Particularly, as said before Taylor and Lagrange's expansions consider two different models for the transformation from a 3D to a 2D structure.



3D CAD



Taylor expansion model



Lagrange expansion model

Figure 2.5: *Differences between CAD, Lagrange and Taylor for plate.*

Chapter 3

Carrera Unified Formulation (CUF) and Finite Element (FE) method

The CUF provides one-dimensional (beam) and two-dimensional (plate and shell) theories that go beyond classical theories. The method is based on a condensed notation expressing the displacement fields in terms of base functions whose forms and orders are arbitrary. Furthermore, it is possible to schematize the structural problem with an index model that represents the displacement fields over the cross section (beam) or along the thickness (plate/shell). The condensed notation can express all the described above theories and permits the definition of the fundamental nuclei (FNs). The FNs can be assembled, following two building loops whose description is thoroughly explained in [18]. The nuclei allow the assembly of all the FEM matrices and vectors involved in the equilibrium equations without a dependence concerning the theory of structures employed. The FNs stem from the 3D elasticity equations via the PVD and can be easily obtained for the 3D, 2D, and 1D cases. The CUF is a unified framework that can be used to derive any FEM model for any structural element with the use of FNs which allows the obtaining of a compact form. Furthermore, the present formulation makes possible a multifield load's easy implementation and multilayered structures study.

3.1 Introduction to CUF for 2D theories

The CUF is introduced by the use of an index notation that extends the classical FEM (i,j) and the theory of structures (τ,s). Therefore, thanks to the CUF the whole displacement field is expressed by the use of these four indexes.

As clear from the previous chapter, plate theories are characterized by an assumption that makes explicit the in-the-thickness behavior. The relation can be done by the use of linear or high-order polynomials or by other functions like Lagrange ones. In all these cases, the displacement field is expressed by the sum of an unknown function depending on the in-plane coordinates and a known z -function.

Considering repeated indexes denote a sum and using i and τ for the displacement and j and s for the differential variation, every 2D structure theory can be written as follow.

$$\mathbf{U}(x, y, z) = F_{\tau}(z)\mathbf{u}_{\tau}(x, y) \quad \tau = 1, 2, \dots, N \quad (3.1)$$

where, F_τ are functions of the thickness coordinate z and \mathbf{u}_τ is the displacement vector which depends on the in-plane coordinates x, y . The order of expansion determines the number of different sum elements N . The z functions can be arbitrary and it is possible to express all the different theories such as TE or LE without a formal change in the expression. It is possible to describe also CLT or FSDT displacement fields which are particular cases of Taylor Expansion, by the use of (i) the rearranging of rows and columns of the stiffness matrix, (ii) penalization of the stiffness terms related to w_1 which is zero.

3.1.1 The FE formulation and the FN

In the present section, a formulation of the displacement field to explicit the stiffness, and loading arrays in weak form using the FEM approach is reported. In a displacement problem, the FEM approach enables obtaining an approximated solution by referring to a finite number of nodes in which the solution is calculated. By the use of the shape functions N_i , the link between nodes displacement and displacement field is a priori determined.

The elastic problem is explicit in the first chapter. Internal and external works can be expressed using the relations reported above and the stiffness matrix and load array are defined. The internal work is reported in eq. 3.2 where only the linear part of the geometric relations are considered.

$$\delta L_{int} = \int_V \delta \boldsymbol{\varepsilon}^T \mathbf{S} dV = \int_V (\mathbf{b}_i \delta \mathbf{U})^T \mathbf{C} (\mathbf{b}_i \mathbf{U}) dV \quad (3.2)$$

Using the FE approach the shape function can make explicit the (x,y) behavior and the relation is:

$$\mathbf{u}(x, y) = N_i(x, y) \mathbf{q}_i \quad (3.3)$$

where \mathbf{q}_i is the vector of the displacement components in the nodes and $N_i(x, y)$ is the Shape Function whose behavior is known and function of the in-plane coordinates. i is an index referred to in the FEM approach which goes from 1 to the number of nodes. The FE method permits to have the solution of the structural problem in a weak form referring to the displacement in a point of the structure to the value of the variable in the nodes through the shape functions. The 2D elements of the FEM could be TRIA or QUAD elements respectively with three or four edges. In the present study, QUAD elements are used for the convergence of the solution. It is possible to use different numbers of nodes for each element, and QUAD4, QUAD9, or QUAD16 are defined. However, independently from the number of elements, the shape functions are the Lagrange function which permits a simple description of the displacement behavior. The formula of the shape functions for a 9 nodes element is the following [5]:

$$\begin{aligned} N_1 &= \frac{1}{4} (\xi^2 - \xi) (\eta^2 - \eta) & N_2 &= \frac{1}{2} (1 - \xi^2) (\eta^2 - \eta) \\ N_3 &= \frac{1}{4} (\xi^2 + \xi) (\eta^2 - \eta) & N_4 &= \frac{1}{2} (\xi^2 + \xi) (1 - \eta^2) \\ N_5 &= \frac{1}{4} (\xi^2 + \xi) (\eta^2 + \eta) & N_6 &= \frac{1}{2} (1 - \xi^2) (\eta^2 + \eta) \\ N_7 &= \frac{1}{4} (\xi^2 - \xi) (\eta^2 + \eta) & N_8 &= \frac{1}{2} (\xi^2 - \xi) (1 - \eta^2) \\ & & N_9 &= (1 - \xi^2) (1 - \eta^2) \end{aligned}$$

where the shape functions are defined in the natural coordinate system. In Figure 3.1 different QUAD elements are represented with relative nodes. In the QUAD4 element, the FEM concept is

represented considering a generic point in the element domain. The unknowns in the generic point depend on the ones calculated on the nodes of the discretization by the use of the shape functions.

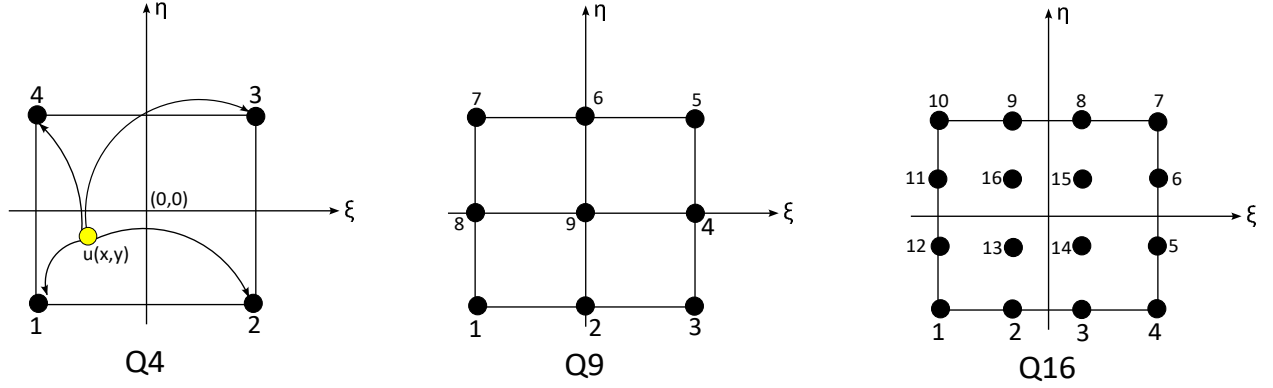


Figure 3.1: *QUAD element representation. Element numeration and displacement dependence on a random point of the element from all nodes.*

Replacing the 3.1 and the 3.3 in the 3.2 we can extract the FEs. The indices j and s are the same as i and τ but referred to the virtual variations.

$$\begin{aligned}
 \int_V (\mathbf{b}_l \delta \mathbf{u})^T \mathbf{C} (\mathbf{b}_l \mathbf{u}) dV &= \int_{\Omega} \int_h (\mathbf{b}_l F_s(z) \delta \mathbf{u}_s(x, y))^T \mathbf{C} \mathbf{b}_l F_{\tau}(z) \mathbf{u}_i(x, y) d\Omega dz = \\
 &= \int_{\Omega} \int_h (\mathbf{b}_l F_s(z) N_j(x, y) \delta \mathbf{q}_{sj})^T \underbrace{\mathbf{C} \mathbf{b}_l F_{\tau}(z) N_i(x, y)}_{\mathbf{B}_l^{\tau i}} \mathbf{q}_{\tau i} d\Omega dz = \int_{\Omega} \int_h \delta \mathbf{q}_{sj}^T \mathbf{B}_l^{sjT} \mathbf{C} \mathbf{B}_l^{\tau i} \mathbf{q}_{\tau i} d\Omega dz = \\
 &\quad \underbrace{\delta \mathbf{q}_{sj}^T \left(\int_{\Omega} \int_h \mathbf{B}_l^{sjT} \mathbf{C} \mathbf{B}_l^{\tau i} d\Omega dz \right)}_{\mathbf{K}^{\tau sij}} \mathbf{q}_{\tau i} \quad (3.4)
 \end{aligned}$$

where $\mathbf{K}^{\tau sij}$ is the 3×3 FNs stiffness matrix (4×4 if a thermo-mechanical coupled approach is considered). The FN is invariant with respect to the plate theory. The nucleus is formally the same in all applied theories, and for the building of the stiffness matrix, FNs are composed as represented in Figure 3.2.

For the sake of clarity, a fundamental nucleus component of the pure static mechanical problem is represented in eq.3.5. All the elements of the FN can be obtained in the same way from the eq. 3.4. In order to obtain the global nucleus referred to in the structures reference system the constitutive matrix changed. The used constitutive matrix coefficients are the rotated coefficients referred to the global reference system whose rotation is described in the section 4.1. For the sake of simplicity, only the extended expression of the first term of the FN is reported, the other FNs are written in Appendix A.

$$\begin{aligned}
 K_{xx}^{\tau sij} &= C_{11} \int_{\Omega} N_{i,x} N_{j,x} d\Omega \int_h F_{\tau} F_s dz + C_{16} \int_{\Omega} N_{i,x} N_{j,y} d\Omega \int_h F_{\tau} F_s dz + \\
 &+ C_{16} \int_{\Omega} N_{i,y} N_{j,x} d\Omega \int_h F_{\tau} F_s dz + C_{44} \int_{\Omega} N_i N_j d\Omega \int_h F_{\tau,z} F_{s,z} dz + C_{66} \int_{\Omega} N_{i,y} N_{j,y} d\Omega \int_h F_{\tau} F_s dz
 \end{aligned} \quad (3.5)$$

For the load array, the virtual external load is considered.

$$\delta L_{ext} = \int_{\Omega} \delta \mathbf{u}^T p(x, y) dS = \int_{\Omega} \delta \mathbf{U}_{sj}^T F_s(z) N_j^T(x, y) p(x, y) dS = \delta \mathbf{U}_{js}^T \mathbf{P} \quad (3.6)$$

where \mathbf{P} is the nodal load array. Therefore, the static problem can be written as follows:

$$\begin{aligned} \delta L_{int} &= \delta L_{ext} \\ \delta \mathbf{q}_{sj}^T \mathbf{K}^{\tau sij} \mathbf{q}_{\tau i} &= \delta \mathbf{q}_{js}^T \mathbf{P} \\ \mathbf{K}^{\tau sij} \mathbf{q}_{\tau i} &= \mathbf{P} \end{aligned} \quad (3.7)$$

where $\mathbf{U}_{\tau i}$ are the nodal displacement of the FEM elements.

3.1.2 Coupled thermo-mechanical problem through CUF and FNs

Unlike the pure mechanical case, the stiffness fundamental nucleus of the thermo-mechanical is a 4×4 matrix, where the last row and the last column are related to the thermal unknowns. The composition of the nucleus is analogous to the purely mechanical case and the introduction of the CUF with the FEM approach has the same formal expression represented in the eq. 3.4. For the sake of simplicity, a graphical representation of the FNs construction is reported in Figure 3.2. Where the FN is represented and the CUF building loop is clearly reported. The yellow terms are the purely mechanical ones, in blue, the pure thermal components are reported and in green the coupling terms.

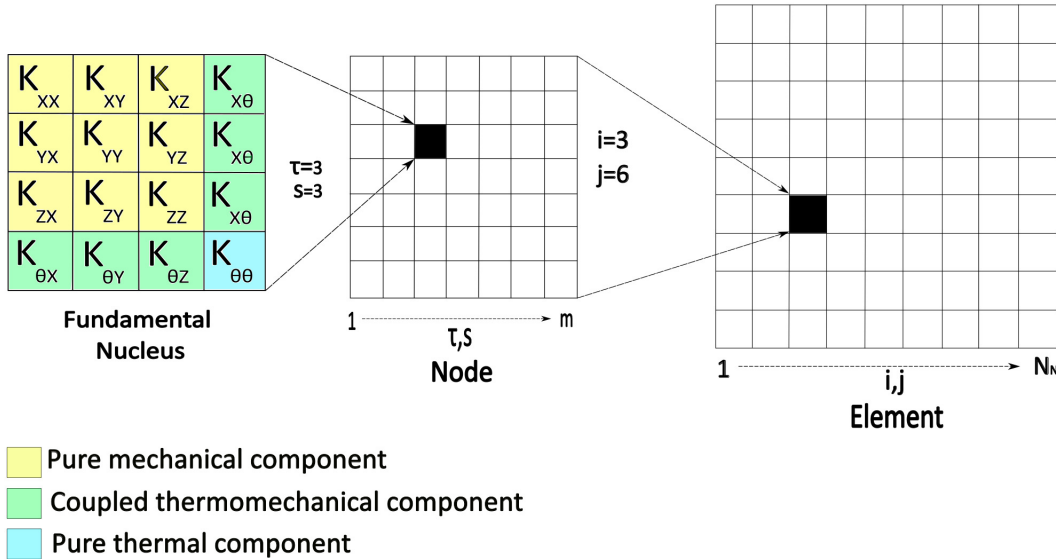


Figure 3.2: Automatic implementation of the stiffness matrix through CUF.

The pure mechanical components of the nucleus are the same reported in eq. 3.5, as reported in the section 3.1.1, and the first element of the thermo-mechanical contributions is reported in eq. 3.8, the whole FNs components are reported in Appendix A.

$$K_{x\theta}^{\tau sij} = -\lambda_1 \int_{\Omega} N_i N_{j,x} d\Omega \int_h F_{\tau} F_s dz - \lambda_6 \int_{\Omega} N_i N_{j,y} d\Omega \int_h F_{\tau} F_s dz \quad (3.8)$$

It is clear, from the above-described stiffness matrix elements, that the coupled thermo-mechanical problem has a mutual influence between mechanical and thermal unknowns.

The present section investigated the thermal static problem by the use of the CUF fundamental nucleus. Assembling the whole stiffness matrix the problem is defined and can be solved.

3.1.3 Buckling FNs

Buckling is one of the principal modes of failure in thin structures such as plates and shells. It occurs with a sudden change in the pate/shell geometry at a critical load.

The plate can buckle under in-plane and compressive stresses that can be caused also by a thermal external load.

Due to the unstable behavior, for a buckling study, a nonlinear problem has to be solved. The nonlinear static equilibrium equations can be easily obtained from the PVD as done in the previous cases. Formally the principle does not change but involving a nonlinear phenomenon the \mathbf{b} tensor includes the Green-Lagrange terms and both, linear and non-linear components of the derivative tensor are introduced in the PVD. The form of the eq. 3.2 changes as follows.

$$\begin{aligned} \delta L_{int} &= \int_V \delta \boldsymbol{\varepsilon}^T \mathbf{S} dV = \int_V ((\mathbf{b}_l + \mathbf{b}_{nl}) \delta \mathbf{u})^T \mathbf{C} ((\mathbf{b}_l + \mathbf{b}_{nl}) \mathbf{u}) dV = \\ &= \int_V \delta \left((\mathbf{B}_l^{sj} + \mathbf{B}_{nl}^{sj}) \mathbf{q}_{sj} \right)^T \mathbf{C} \left((\mathbf{B}_l^{\tau i} + \mathbf{B}_{nl}^{\tau i}) \mathbf{q}_{\tau i} \right) dV = \\ &= \delta \mathbf{q}_{sj}^T \underbrace{\int_V \left(\mathbf{B}_l^{sj} + 2\mathbf{B}_{nl}^{sj} \right)^T \mathbf{C} \left(\mathbf{B}_l^{\tau i} + \mathbf{B}_{nl}^{\tau i} \right) dV}_{\mathbf{K}_s^{\tau sij}} \mathbf{q}_{\tau i} \quad (3.9) \end{aligned}$$

It is important to know that $\delta \mathbf{B}_{nl} = 2\mathbf{B}_{nl}$. For clearance the matrices \mathbf{B}_l and \mathbf{B}_{nl} obtained from the eq. 3.9 are reported below written in terms of the fundamental nucleus.

$$\mathbf{B}_l^{sj} = \begin{pmatrix} F_s N_{j,x} & 0 & 0 \\ 0 & F_s N_{j,y} & 0 \\ 0 & 0 & F_{s,z} N_j \\ F_{s,z} N_j & 0 & F_s N_{j,x} \\ 0 & F_{s,z} N_j & F_s N_{j,y} \\ F_s N_{j,y} & F_s N_{j,x} & 0 \end{pmatrix} \quad (3.10)$$

$$\mathbf{B}_{nl} = \frac{1}{2} \begin{pmatrix} u_{x,x} F_s N_{j,x} & u_{y,x} F_s N_{j,x} & u_{z,x} F_s N_{j,x} \\ u_{x,y} F_s N_{j,y} & u_{y,y} F_s N_{j,y} & u_{z,y} F_s N_{j,y} \\ u_{x,z} F_{s,z} N_j & u_{y,z} F_{s,z} N_j & u_{z,z} F_{s,z} N_j \\ u_{x,x} F_{s,z} N_j + u_{x,z} F_s N_{j,x} & u_{y,x} F_{s,z} N_j + u_{y,z} F_s N_{j,x} & u_{z,x} F_{s,z} N_j + u_{z,z} F_s N_{j,x} \\ u_{x,y} F_{s,z} N_j + u_{x,z} F_s N_{j,y} & u_{y,y} F_{s,z} N_j + u_{y,z} F_s N_{j,y} & u_{z,y} F_{s,z} N_j + u_{z,z} F_s N_{j,y} \\ u_{x,x} F_s N_{j,y} + u_{x,y} F_{s,z} N_j & u_{y,x} F_s N_{j,y} + u_{y,y} F_{s,z} N_j & u_{z,x} F_s N_{j,y} + u_{z,y} F_{s,z} N_j \end{pmatrix}$$

$\mathbf{K}_s^{\tau sij}$ is the stiffness secant matrix fundamental nucleus and is composed as indicated below. With the building loops by the index τ, s, i, j it is possible to obtain the secant stiffness matrix \mathbf{K}_s which

depends on the unknowns.

$$\begin{aligned}
 \mathbf{K}_{ll}^{\tau sij} &= \int_V \mathbf{B}_l^{sjT} \mathbf{C} \mathbf{B}_l^{\tau i} dV \\
 \mathbf{K}_{lnl}^{\tau sij} &= \int_V \mathbf{B}_l^{sjT} \mathbf{C} \mathbf{B}_{nl}^{\tau i} dV \\
 \mathbf{K}_{nll}^{\tau sij} &= \int_V 2\mathbf{B}_{nl}^{sjT} \mathbf{C} \mathbf{B}_l^{\tau i} dV \\
 \mathbf{K}_{nlnl}^{\tau sij} &= \int_V 2\mathbf{B}_{nl}^{sjT} \mathbf{C} \mathbf{B}_{nl}^{\tau i} dV \\
 \mathbf{K}_s^{\tau sij} &= \mathbf{K}_{ll}^{\tau sij} + \mathbf{K}_{lnl}^{\tau sij} + \mathbf{K}_{nll}^{\tau sij} + \mathbf{K}_{nlnl}^{\tau sij}
 \end{aligned} \tag{3.11}$$

Using the PVD as reported in eq.3.1.1 and introducing the nodal load vector \mathbf{P} it is possible to obtain the nonlinear governing equation 3.12.

$$\mathbf{K}_s \mathbf{q} = \mathbf{P} \tag{3.12}$$

where \mathbf{q} is the nodal displacement vector. For the approximated solution of the nonlinear problem, an iterative process has to be followed. The equation 3.12 permits obtaining, without further derivations, both the equilibrium residual and the iterative matrix. The stiffness secant matrix is easily obtained from internal virtual work and permits a nonlinear equilibrium conditions description of the structural theory but usually is non-symmetric, and not uniquely defined. Due to the reported considerations, the secant method is not so diffused, particularly because the common numerical software has assembling, memorizing, and resolution classical routines that are simplified for symmetric stiffness matrix. Using a non-symmetric matrix makes necessary the introduction of new and heavier algorithms [20].

Usually, the resolution of the nonlinear problem is done by a linearized resolution scheme that uses the tangent method and the definition of a new stiffness matrix called tangent matrix.

From the linearization of the PVD, it is possible to obtain a new expression of the nonlinear equation with a symmetric tangent stiffness matrix that could be used to solve the non-linear problem in an iterative linearized scheme [21] with some advantages with respect to the stiffness one. If a conservative external load is applied, the linearization of the external virtual load is zero. Therefore, it is necessary to linearize only the virtual internal work as follows.

$$d(\delta L_{int}) = \int_V d(\delta \boldsymbol{\varepsilon}^T \mathbf{S}) dV = \int_V \delta \boldsymbol{\varepsilon}^T d\mathbf{S} dV + \int_V d(\delta \boldsymbol{\varepsilon}^T) \mathbf{S} dV \tag{3.13}$$

Assuming that the material coefficients remain constant, the strain differential is reported in the equation 3.14. The first term of the equation 3.13 is easily obtained as reported below:

$$d\mathbf{S} = d(\mathbf{C}\boldsymbol{\varepsilon}) = \mathbf{C}d\boldsymbol{\varepsilon} = \mathbf{C}d((\mathbf{B}_l^{\tau i} + \mathbf{B}_{nl}^{\tau i}) \mathbf{q}_{\tau i}) = \mathbf{C}(\mathbf{B}_l^{\tau i} + 2\mathbf{B}_{nl}^{\tau i}) d\mathbf{q}_{\tau i} \tag{3.14}$$

Replacing the 3.14 in the first term of the 3.13 it is possible to develop the first part of the tangent matrix.

$$\begin{aligned}
 \int_V \delta \boldsymbol{\varepsilon}^T d\mathbf{S} dV &= \delta \mathbf{q}_{sj} \int_V \left(\mathbf{B}_l^{sj} + 2\mathbf{B}_{nl}^{sj} \right) \mathbf{C} \left(\mathbf{B}_l^{\tau i} + 2\mathbf{B}_{nl}^{\tau i} \right) dV \, d\mathbf{q}_{\tau i} = \\
 &= \delta \mathbf{q}_{sj}^T \int_V \left(\mathbf{B}_l^{sjT} \mathbf{C} \mathbf{B}_l^{\tau i} + 2\mathbf{B}_{nl}^{sjT} \mathbf{C} \mathbf{B}_l^{\tau i} + 2\mathbf{B}_l^{sjT} \mathbf{C} \mathbf{B}_{nl}^{\tau i} + 4\mathbf{B}_{nl}^{sjT} \mathbf{C} \mathbf{B}_{nl}^{\tau i} \right) dV \, d\mathbf{q}_{\tau i} = \\
 &= \delta \mathbf{q}_{sj}^T \left(\underbrace{\mathbf{K}_{ll}^{\tau sij}}_{\mathbf{K}_0^{sj\tau i}} + \underbrace{\mathbf{K}_{nll}^{\tau sij} + 2\mathbf{K}_{lnl}^{\tau sij} + 2\mathbf{K}_{nlnl}^{\tau sij}}_{\mathbf{K}_{T1}^{\tau sij}} \right) d\mathbf{q}_{\tau i} \quad (3.15)
 \end{aligned}$$

where $\mathbf{K}_0^{sj\tau i}$ and $\mathbf{K}_{T1}^{sj\tau i}$ are the first two terms of the fundamental nucleus of the tangent stiffness matrix. The second term of the equation 3.13 can be written by applying the differential operator to the strain vector.

$$\begin{aligned}
 \int_V d(\delta \boldsymbol{\varepsilon}^T) \mathbf{S} dV &= \begin{Bmatrix} dq_{x\tau i} \delta q_{xsj} \\ dq_{y\tau i} \delta q_{ysj} \\ dq_{z\tau i} \delta q_{zsj} \end{Bmatrix}^T \int_V \mathbf{B}_{nl}^{*T} \mathbf{S} dV = \begin{Bmatrix} dq_{x\tau i} \delta q_{xsj} \\ dq_{y\tau i} \delta q_{ysj} \\ dq_{z\tau i} \delta q_{zsj} \end{Bmatrix}^T \int_V \mathbf{B}_{nl}^{*T} (\mathbf{S}_l + \mathbf{S}_{nl}) dV = \\
 &= \delta \mathbf{q}_{sj}^T \int_V \text{diag} \left(\mathbf{B}_{nl}^{*T} (\mathbf{S}_l + \mathbf{S}_{nl}) \right) dV \cdot d\mathbf{q}_{\tau i} = \delta \mathbf{q}_{sj}^T \left(\mathbf{K}_{\sigma l}^{\tau sij} + \mathbf{K}_{\sigma nl}^{\tau sij} \right) d\mathbf{q}_{\tau i} = \delta \mathbf{q}_{sj}^T \mathbf{K}_{\sigma}^{\tau sij} d\mathbf{q}_{\tau i} \quad (3.16)
 \end{aligned}$$

where \mathbf{B}_{nl}^* is reported below.

$$\mathbf{B}_{nl}^* = \begin{pmatrix} F_s N_{j,x} F_{\tau} N_{i,x} & F_s N_{j,x} F_{\tau} N_{i,x} & F_s N_{j,x} F_{\tau} N_{i,x} \\ F_s N_{j,y} F_{\tau} N_{i,y} & F_s N_{j,y} F_{\tau} N_{i,y} & F_s N_{j,y} F_{\tau} N_{i,y} \\ F_{s,z} N_j F_{\tau,z} N_i & F_{s,z} N_j F_{\tau,z} N_i & F_{s,z} N_j F_{\tau,z} N_i \\ F_s N_{j,x} F_{\tau,z} N_i + F_{s,z} N_j F_{\tau} N_{i,x} & F_s N_{j,x} F_{\tau,z} N_i + F_{s,z} N_j F_{\tau} N_{i,x} & F_s N_{j,x} F_{\tau,z} N_i + F_{s,z} N_j F_{\tau} N_{i,x} \\ F_s N_{j,y} F_{\tau,z} N_i + F_{s,z} N_j F_{\tau} N_{i,y} & F_s N_{j,y} F_{\tau,z} N_i + F_{s,z} N_j F_{\tau} N_{i,y} & F_s N_{j,y} F_{\tau,z} N_i + F_{s,z} N_j F_{\tau} N_{i,y} \\ F_s F_{\tau} N_{i,x} N_{j,y} + F_s F_{\tau} N_{i,y} N_{j,x} & F_s F_{\tau} N_{i,x} N_{j,y} + F_s F_{\tau} N_{i,y} N_{j,x} & F_s F_{\tau} N_{i,x} N_{j,y} + F_s F_{\tau} N_{i,y} N_{j,x} \end{pmatrix} \quad (3.17)$$

The complete tangent stiffness matrix \mathbf{K}_t is reported below where, based on the fundamental nucleus and using the building loops based on the indexes τ, s, i, j the complete matrix can be built.

$$\mathbf{K}_t = \mathbf{K}_0 + \mathbf{K}_{T1} + \mathbf{K}_{\sigma} \quad (3.18)$$

For a simplified resolution method, the analysis can consider the critical buckling load as the load at which more than one adjacent equilibrium configuration exists. This load corresponds to the called bifurcation point. Be careful that, in the case of defect-sensitive structures such as cylindrical structures, the reached load corresponding to the bifurcation point could be higher than the real buckling critical load.

Following this consideration, in a linearized analysis, the critical load value can be found solving a linear eigenvalue problem. The simplest approach can be used for the study of both thin and thick plates, more complex is the application to cylindrical problems. It is important to note that the linearized analysis makes sense if the buckled configuration path has a bifurcation point [22]. For

the sake of clearance, a representation of the difference between the bifurcation and no-bifurcation point is reported in Figure 3.3. The presence of the bifurcation point is typical of beam and panel behavior.

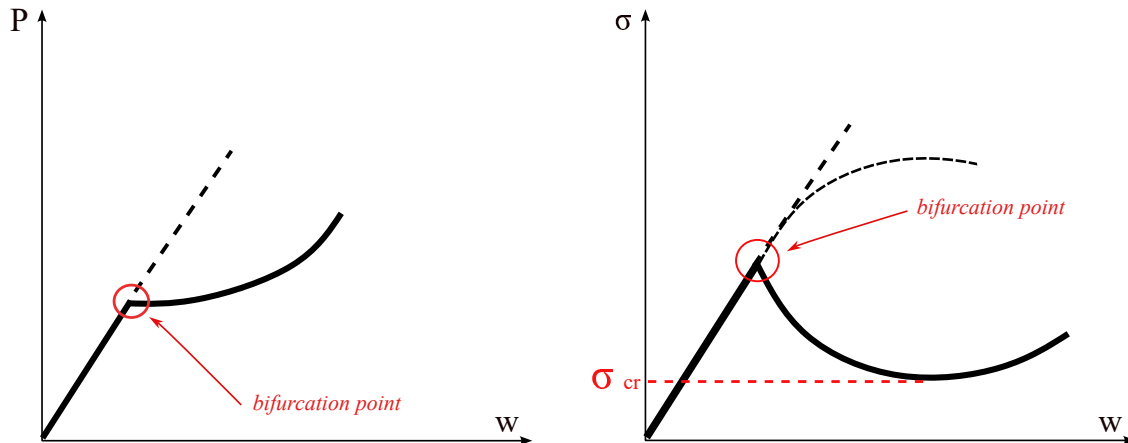


Figure 3.3: Representation of the ideal buckling representing the cases of bifurcation. On the left plate/beam behavior, on the right typical cylinder buckling behavior where bifurcation point can not be considered as critical load. w represents the in plane deflection.

Linearizing the developed non-linear problem permits obtaining a simple formulation of the problem that considers the presence of the two equilibrium configurations. Therefore, the approach can be used for the study of the critical load but can not carry out post-buckling information.

The linearized problem is carried out as follows.

$$\mathbf{K}_t = \mathbf{K}_0 + \cancel{\mathbf{K}_{nl}} + 2\cancel{\mathbf{K}_{lnl}} + 2\mathbf{K}_{nl} + \mathbf{K}_{\sigma l} + \cancel{\mathbf{K}_{\sigma nl}} \simeq \mathbf{K}_0 + \lambda \mathbf{K}_{\sigma l} \quad (3.19)$$

where λ is a multiplicative coefficient necessary after the simplification and used to involve the load dependence to the linear component in the equation. λ is a multiplier factor. If F is the analysis applied load, λF represents the critical buckling load. By linearizing the stiffness matrix components the only ones that remain are \mathbf{K}_0 and $\mathbf{K}_{\sigma l}$. As explained in [23] the matrix obtained allows the definition of the problem as follows.

$$(\mathbf{K}_0 + \lambda \mathbf{K}_{\sigma l}) \mathbf{q} = 0 \quad (3.20)$$

In order to solve the problem without the trivial solution an eigenvalue problem is defined as following:

$$|\mathbf{K}_0 + \lambda \mathbf{K}_{\sigma l}| = 0 \quad (3.21)$$

Where the symbol $|\cdot|$ indicates the eigenvalue problem.

The present section has described the classical buckling problem. Considering thermal buckling the problem could be reported in the same way as the mechanical one. Furthermore, the \mathbf{K}_{σ} , which contains the linear stresses of the static problem became dependent on thermal stresses.

Chapter 4

Introduction to multilayered structures

Classical Plate Theories (CPT) have been introduced for thin isotropic plates. The CLT and the FSDT use a linear description of the displacement field along the thickness. For a better description high order deformation theories can be used where, by means of the use of quadratic, cubic, or higher variations or non-polynomial expansions the phenomenon description along the thickness is improved. When a multilayered configuration is studied, improving the polynomial degree may not be enough because new effects arise with respect to the one-layered structure in terms of transverse anisotropy. In multilayered structures, the presence of different materials causes transverse discontinuous mechanical properties, and displacements show rapid changes and different slopes at every interface called the Zig-Zag effect(ZZ). Because of the constitutive relations, also transverse continuity, required by Chauchy (Interlaminar Continuity IC) is not guaranteed. Also, HOT can not represent ZZ and IC requirements (called C_z^0). The CPTs use Equivalent Single Layer Models (ESLM) where the number of unknown variables remains independent of the number of layers. A possible manner to naturally include the C_z^0 requirements could be implemented by applying CPT at a layer level. Each one can be seen as an independent plate and displacement continuity at each interface became an imposed constraint. This approach is called Layer Wise (LW) method. More details about the material in-thickness description are available in [25].

4.1 Multilayered structures

The description of multilayered structures represents a challenge for the introduction of some mechanics peculiarities. Furthermore, it is necessary to study the applicability of the traditional theories and approaches developed for classical isotropic and homogeneous materials to multilayered structures. A description of the principal phenomena introduced from the multilayered structures can be found in [26].

As it is clear from the lamination description, the orientation of the single layer could be different between each layer where the local principal direction is typically indicated by the fiber one. The constitutive matrix defined in Chapter 2 and the relative material coefficients are given in the material reference system 1,2,3 reported in Figure 4.1. For a global description, the properties in the local reference system must be referred to the global reference system by using rotation matrices $\mathbf{T}_1, \mathbf{T}_2$ where the axis ' z' ' corresponds to the direction 3 and α is the clockwise rotation needed to

superpose the 1,2 axes to x,y as reported in Fig. 4.1.

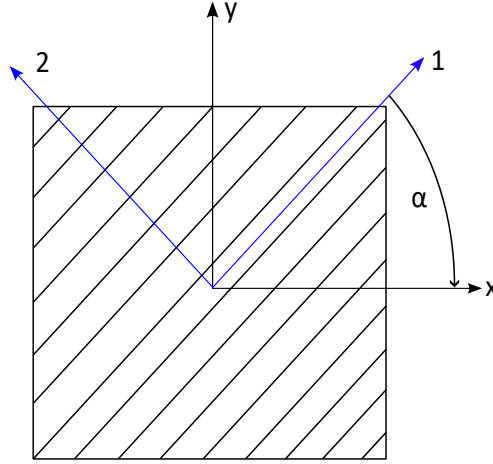


Figure 4.1: Rotation angle α and representation of the lamina rotation from a lamina to a global reference system.

$$\mathbf{T}_1 = \begin{pmatrix} \cos^2(\alpha) & \sin^2(\alpha) & 0 & 0 & 0 & -\sin(2\alpha) \\ \sin^2(\alpha) & \cos^2(\alpha) & 0 & 0 & 0 & \sin(2\alpha) \\ 0 & 0 & 1 & 0 & 0 & 0 \\ 0 & 0 & 0 & \cos(\alpha) & -\sin(\alpha) & 0 \\ 0 & 0 & 0 & \sin(\alpha) & \cos(\alpha) & 0 \\ \sin(\alpha)\cos(\alpha) & -\sin(\alpha)\cos(\alpha) & 0 & 0 & 0 & \cos^2(\alpha) - \sin^2(\alpha) \end{pmatrix} \quad (4.1)$$

$$\mathbf{T}_2 = (1) \quad (4.2)$$

By the application of the rotation matrices, it is possible to define the material properties in the global reference system x,y,z . In eq.s 4.3, 4.4, and 4.5 the rotations are applied for a decoupled approach. In the decoupled framework eq. 4.5 is used for a pure thermal problem.

$$\begin{pmatrix} C_{11} & C_{12} & C_{13} & 0 & 0 & C_{16} \\ C_{21} & C_{22} & C_{23} & 0 & 0 & C_{26} \\ C_{31} & C_{32} & C_{33} & 0 & 0 & C_{36} \\ 0 & 0 & 0 & C_{44} & C_{45} & 0 \\ 0 & 0 & 0 & C_{54} & C_{55} & 0 \\ C_{61} & C_{62} & C_{63} & 0 & 0 & C_{66} \end{pmatrix}_{x,y,z} = \mathbf{T}_1 \begin{pmatrix} C_{11} & C_{12} & C_{13} & 0 & 0 & 0 \\ C_{21} & C_{22} & C_{23} & 0 & 0 & 0 \\ C_{31} & C_{32} & C_{33} & 0 & 0 & 0 \\ 0 & 0 & 0 & C_{44} & 0 & 0 \\ 0 & 0 & 0 & 0 & C_{55} & 0 \\ 0 & 0 & 0 & 0 & 0 & C_{66} \end{pmatrix}_{1,2,3} \mathbf{T}_1^T \quad (4.3)$$

$$\{\lambda_1 \ \lambda_2 \ \lambda_3 \ 0 \ 0 \ \lambda_6\}_{x,y,z} = \mathbf{T}_2 \{\lambda_1 \ \lambda_2 \ \lambda_3 \ 0 \ 0 \ 0\}_{1,2,3} \mathbf{T}_1^T \quad (4.4)$$

$$\chi_{x,y,z} = \mathbf{T}_2 \chi_{1,2,3} \mathbf{T}_2^T \quad (4.5)$$

For a coupled thermo-elastic analysis the matrix reported in eq. 2.23 becomes the following where all the terms describing the problem are reported in the same matrix.

$$\mathbf{C} = \begin{pmatrix} C_{11} & C_{12} & C_{13} & 0 & 0 & C_{16} & -\lambda_1 \\ C_{21} & C_{22} & C_{23} & 0 & 0 & C_{26} & -\lambda_2 \\ C_{31} & C_{32} & C_{33} & 0 & 0 & C_{36} & -\lambda_3 \\ 0 & 0 & 0 & C_{44} & C_{45} & 0 & 0 \\ 0 & 0 & 0 & C_{54} & C_{55} & 0 & 0 \\ C_{61} & C_{62} & C_{63} & 0 & 0 & C_{66} & -\lambda_6 \\ -\lambda_1 & -\lambda_2 & -\lambda_3 & 0 & 0 & -\lambda_6 & -\chi \end{pmatrix} \quad (4.6)$$

4.2 Variable angle tow (VAT)

VATs are new advanced composite materials where the applied fiber allows a curvilinear path to improve efficiency and adapt the composite properties, stiffness, and strength to the more opportune adapting the lamination to the boundary conditions. Furthermore, it is possible to have better after-load configuration. The VAT methodology is not new but in recent years is discovered again with new manufacturing technology such as the Automated Fibre Placement (AFP) technique and the Continuous Tow Shearing (CTS) process which allow fiber orientation to change with respect to more directions. It is possible to modify the direction of the fibers in one or more layers to redirect the load fluxes and improve the structural performance in different configurations such as the stresses distribution around a hole, the maximization of the buckling load of panels, or the reduction of the losses in in-plane compressive stiffness in the post-buckling state [27].

Referring to the material description and the constitutive coefficients, from the previous section it is clear that a global characterization is necessary and it depends on the fiber orientations. Considering a VAT panel, fibers change from one point to another and the constitutive coefficients can not be described using a simple rotation matrix.

Considering a linear fiber angle variation over the lamina the orientation of the fibers is described by the eq. 4.7 using the notation taken from [6]:

$$\theta(x') = \Phi + T_0 + \frac{T_1 - T_0}{d}|x'| \quad (4.7)$$

where Φ indicates the rotation of the local reference system with respect to a certain reference direction, x' is the coordinate of the new rotated system, and T_0 and T_1 are two different reference angles with a characteristic distance indicated with d . These variables are defined such that the fiber orientation angle at a certain point is T_0 and varies along the direction x' oriented by an angle Φ from the original coordinate axis x , the fiber reached an angle T_1 at a characteristic distance d from the reference point. The fiber orientation is expressed by a $\theta(x')$ where $x' = x \cos \Phi + y \sin \Phi$. The parameter d is equal to $a/2$ and $b/2$ when $\Phi = 0^\circ$ or $\Phi = 90^\circ$ where a and b are the edge length of the 2D structures reported in Figure 4.2. In Figure 4.2 geometry and the curvilinear path are reported with all the variables describing the VAT direction problem.

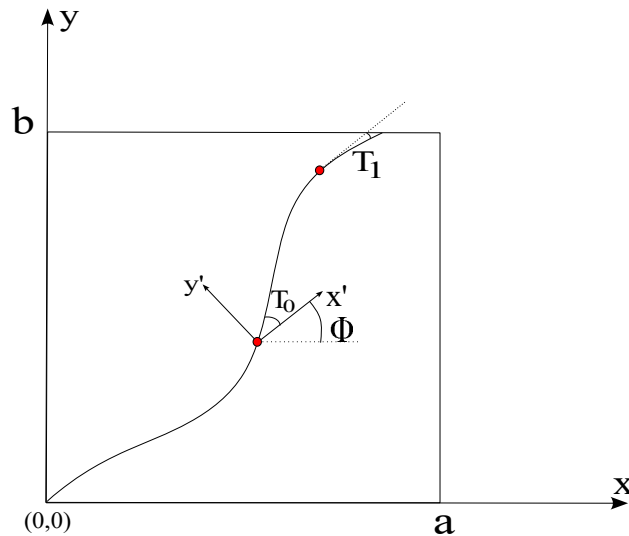


Figure 4.2: Description of the fiber orientation in VAT curvilinear path.

As clear, in the case of VAT layers, it is not possible to rotate the lamina with a single rotation matrix as in a straight configuration. Therefore, it is necessary to consider a different rotation from one point to another depending on the local fiber orientation. To do the opportune rotations the FE discretization is carried out of dimension that allows the orientation description of a single mesh element as constant as represented in Figure 4.3. In Figure 4.3 the mesh discretization allows us to consider fiber orientation as defined by a constant angle value for each mesh element.

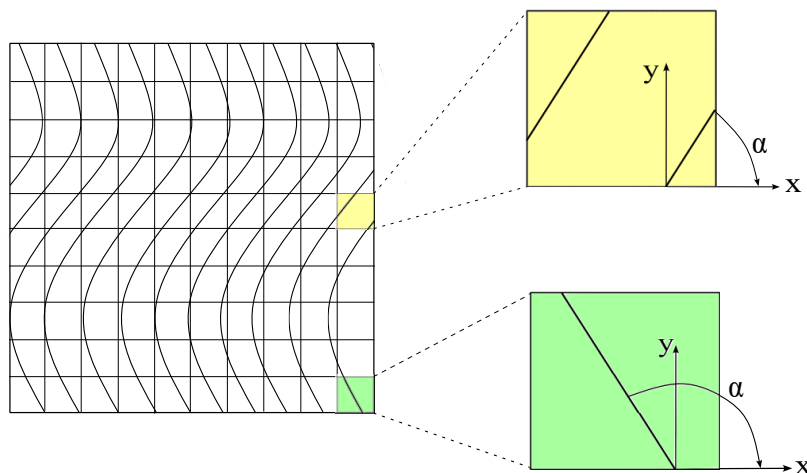


Figure 4.3: Discretization and local rotation angle for a VAT panel.

4.3 Equivalent Single Layer Method

In the Equivalent Single Layer approach (ESL) the stiffness matrix is obtained considering a homogenization of the constitutive properties of the single layer. The properties from all the different layers are simply summed and the behavior of the multilayer is studied as a single-layer plate with a material characterized by the same variables assumed for the entire cross-section. The homogeniza-

tion of the properties is graphically represented in Figure 4.4 where a FN is graphically reported. Considering, for example, the first term of equation 3.5, the integer in 'z' is influenced by the layer thickness and material as reported in eq. 4.8 whose material configuration is represented in Figure 4.4.

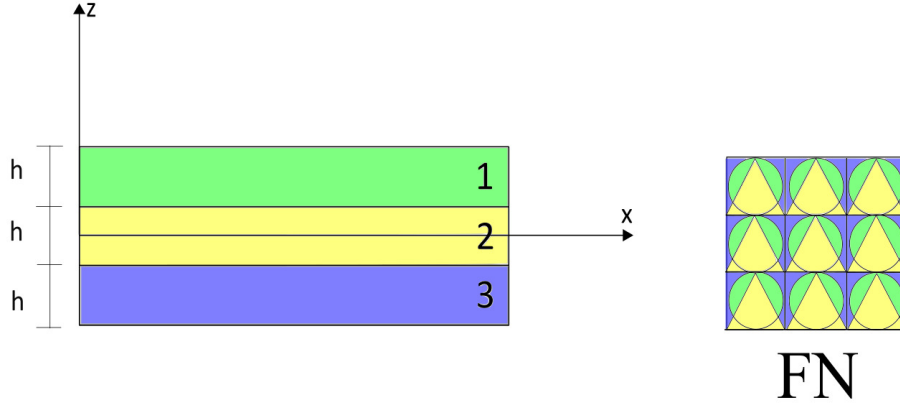


Figure 4.4: Lamination example with an ESL FN representation.

$$\begin{aligned}
 C_{11} \int_{\Omega} N_{i,x} N_{j,x} d\Omega \int_h F_{\tau} F_s dz = \\
 = \int_{\Omega} N_{i,x} N_{j,x} \left(\int_{\frac{h}{2}}^{\frac{3}{2}h} C_{11}^{(1)} F_{\tau} F_s dz + \int_{-\frac{h}{2}}^{\frac{h}{2}} C_{11}^{(2)} F_{\tau} F_s dz + \int_{-\frac{3}{2}h}^{-\frac{h}{2}} C_{11}^{(3)} F_{\tau} F_s dz \right) d\Omega \quad (4.8)
 \end{aligned}$$

4.4 Layer Wise methods (LW)

By the use of a Layer Wise method (LW), each different layer is described by its own set of variables where the continuity is imposed at each interface. Furthermore, the LW approach makes it possible to represent the ZZ effect due to the different materials permitting it to represent the discontinuity of the derivatives of the displacements. To impose the BC between the different layers, the Lagrange theory is used for the plate model, indeed, the relative polynomials are very useful to interpolate the displacement at the top and the bottom position of the layer. Every single layer considers its own material and at the interface, the compatibility is imposed by the following relation which allows the definition of the FN and the stiffness matrix with the overlap of the components referred to the interface as clearly represented in Figure 4.5.

$$\mathbf{u}_t^k = \mathbf{u}_b^{k+1} \quad (4.9)$$

where the subscripts t and b represent respectively the top and bottom, u is the displacement at each node and k is an index that indicates the considered layer.

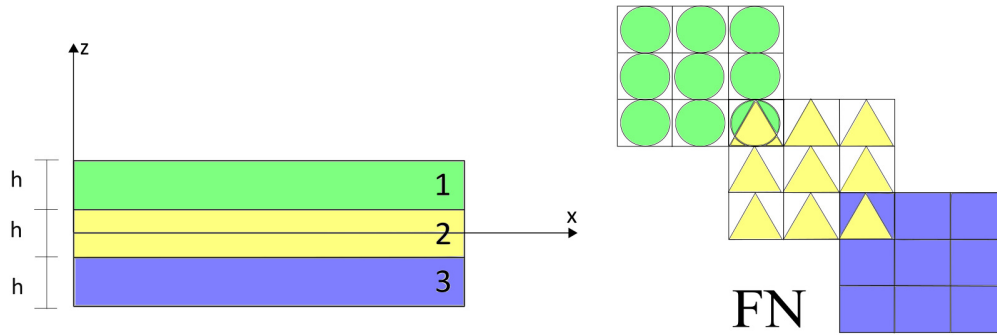


Figure 4.5: *Lamination example with an layer wise FN representation.*

As clear from Figure 4.5, the use of the LE with the LW approach permits the description of laminated material behavior in a better way than using an ESL approach. On the other hand, the use of the LW approach involves an increase in the dimensions of the matrix of the FN and consequently of the stiffness matrix. This is related also to the increase in the unknowns due to the use of the LE.

Chapter 5

Thermo-mechanical analyses for isotropic and laminated composite plate

5.1 Coupled analysis of isotropic laminates

A first analysis is presented to validate the present method in a coupled static thermo-mechanical analysis. The considered model is represented in Figure 5.1 and is composed by different layers of isotropic material. For the analysis a discretization with Q9 in-plane elements and LE in-thickness functions are used. The influence of the expansion order is investigated in the present section. Furthermore, to accurately describe the thermal stresses due to the applied over-temperature, a first convergence analysis is carried out. Therefore, the better number of elements is chosen for a realistic problem description with good computational cost. First of all, a temperature profile taken from the literature [3] is compared with the one calculated by the present method to validate the analysis and the model. The shown results are taken from the x and y center point of the plate.

5.1.1 Validation of the analysis

A simply supported square plate is analyzed, the edge dimensions are $a=b=100$ mm, thickness $t=1$ mm. It is composed by two symmetric external aluminum layers each one of 0.24 mm, and two central layers composed of steel each one with a thickness of 0.26 mm. The aluminum material coefficients are the following, $E = 73000MPa$, $\nu = 0.34$, $\alpha = 25 \cdot 10^{-6}K^{-1}$, $K = 180 \cdot 10^{-3}W/(mmK)$ $\rho = 2800 \cdot 10^{-9}Kg/mm^3$. Steel material coefficients are: $E = 210000MPa$, $\nu = 0.3$ $\alpha = 11.1 \cdot 10^{-6}K^{-1}$ $K = 13 \cdot 10^{-3}W/(mmK)$ $\rho = 7860 \cdot 10^{-9}Kg/mm^3$.

A thermal external load is imposed on the top and bottom of the plate with a variation to the external reference temperature of about -10 *degrees* for the bottom and +10 *degrees* for the top of the plate. The plate is bounded along the external edges of the bottom surface and consequently displacements could be not symmetric.

The plate geometry and applied BCs are represented in a section view in Figure 5.1.

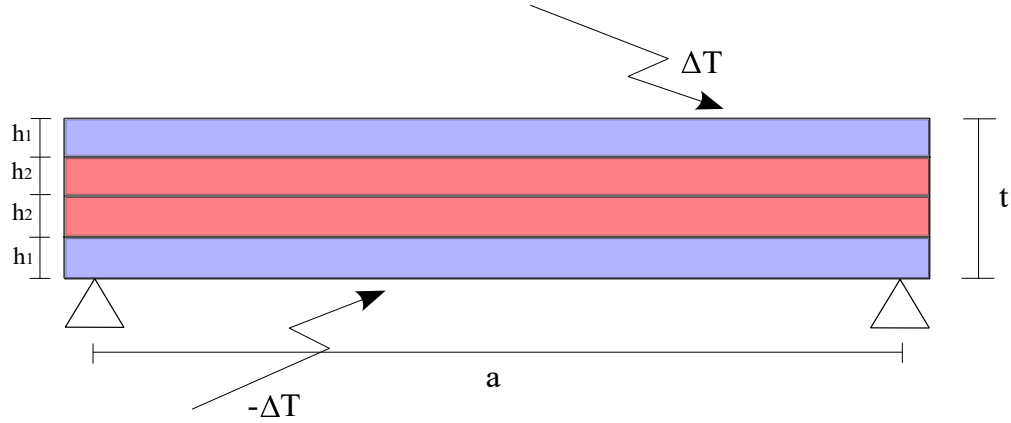


Figure 5.1: Geometry, material and BCs representation of the analyzed plate.

The published temperature profile is represented with the black square in Figure 5.2 and is taken from *Some Results on Thermal Stress of Layered Plates and Shells by Using Unified Formulation* [3]. In the same graph, it is reported the temperature profile calculated with the present method using a coupled approach and modeling the problem with a mesh discretization of 20 x 20 Q9 elements with 1 LE3 in-thickness expansion each layer.

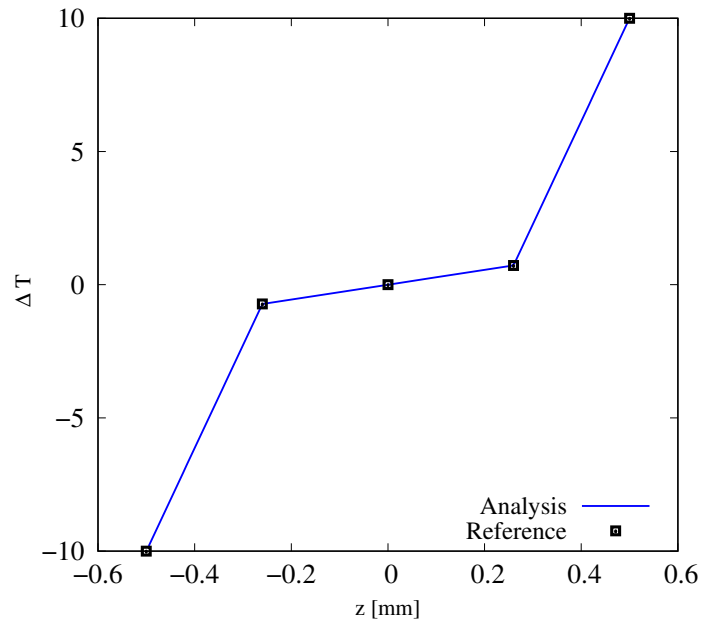


Figure 5.2: Temperature profile from references [3] and calculated temperature profile with a surface discretization of 20x20 Q9 elements and in-thickness expansion with 4 LE 3. Aluminum external material, steel internal material.

Table 5.1: *Over temperature results for model validation. Surface discretization with 20x20 Q9 elements and in-thickness expansion with 4 LE 3, aluminum external material, steel internal material.*

z [mm]	-0.26	0	0.26
ΔT present work	-0.718	0	0.718
ΔT reference [3]	-0.72	0	0.72

It is clear from the reported Figure 5.2 and Table 5.1, that the two temperature profiles are perfectly overlapped. The profile calculated with the coupled approach is influenced also by the mechanical stresses. However, the conductivity of the material is the most important term in the temperature profile generation and makes evident the presence of two different materials. From the two different slopes of the thermal profile, it is clear that there are two materials with different conductivity coefficients. Thanks to the slope of the profile, it is also evident that the external material has an higher conductivity than the internal one.

The validation of the approach for the analysis of the coupled thermo-mechanical analysis is done and in the following section, some results from the convergence analysis are reported.

5.1.2 Convergence study: surfaces elements Q9

The following graphs represent the stresses (Fig. 5.5), and the displacement in the ' z ' direction (Fig. 5.3) of the same plate but with different discretization. Geometry and material are unchanged from the previous case, the only difference is the lamination. In the following case, the external layers are composed of steel and the inner layers are of aluminum, no change in the thickness is present. A convergence analysis is carried out by increasing the number of QUAD9 elements on the surfaces from 64 to 625 and comparing the stress behavior of the different discretizations. The in-thickness expansion is modeled by four three-order Lagrange functions. The number of elements is increased to find a better trade-off between results and computational cost. The different curves are compared and the best number of elements fitting the surface behavior is discovered. The in-thickness expansion is kept constant and does not change in the present convergence analysis. The convergence trend is better represented by the logarithmic graph in Fig. 5.4 where the relative displacement to the reference value of the 25 x 25 analysis is reported as a function of the number of elements. For the sake of clarity, the displacement values are also collected in Table 5.2. The displacements in the x and y direction are not reported because their low value could be subjected to numerical problems and are not interesting in the present work.

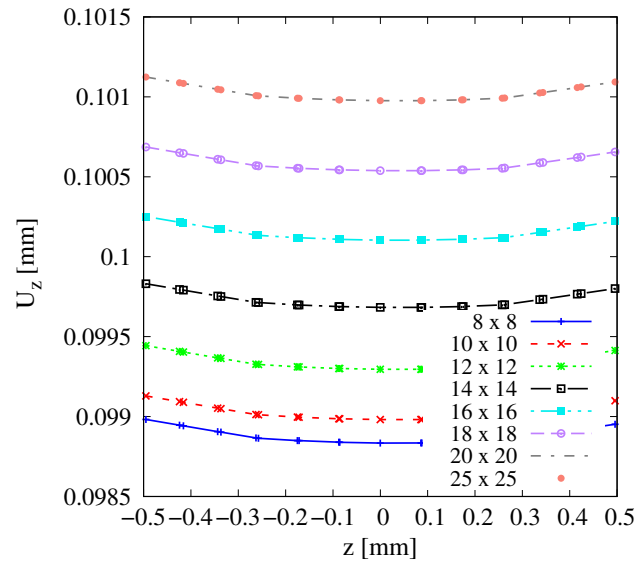


Figure 5.3: Displacement convergence. Variation of the discretization number of Q9 elements along the plane, 4 LE3 in-thickness expansion. Steel external material, aluminum internal material.

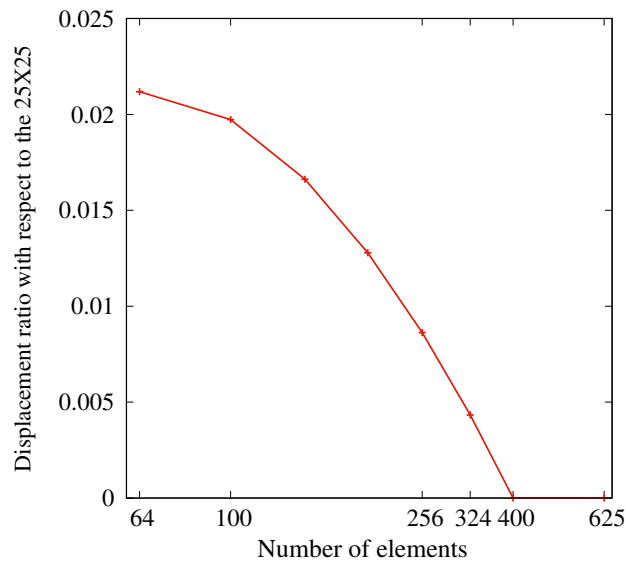


Figure 5.4: Convergence analysis in x -logarithmic way. Variation in the discretization number of Q9 elements along the plane, 4 LE3 in-thickness expansion. Steel external material, aluminum internal material.

Table 5.2: Maximum displacement value for each surface discretization. In-thickness expansion 4LE3. Steel external material, aluminum internal material.

Elements number [Q9]	8x8	10x10	12x12	14x14	16x16	18x18	20x20	25x25
Max displacement [mm]	0.0990	0.0991	0.0994	0.0998	0.1003	0.1007	0.1011	0.1011

For a better representation of the influence due to the in-plane discretization also the stress trends are reported. It is clear that considering an isotropic material, the stresses in x and y directions are the same. This will not be true in the following section when orthotropic materials are introduced.

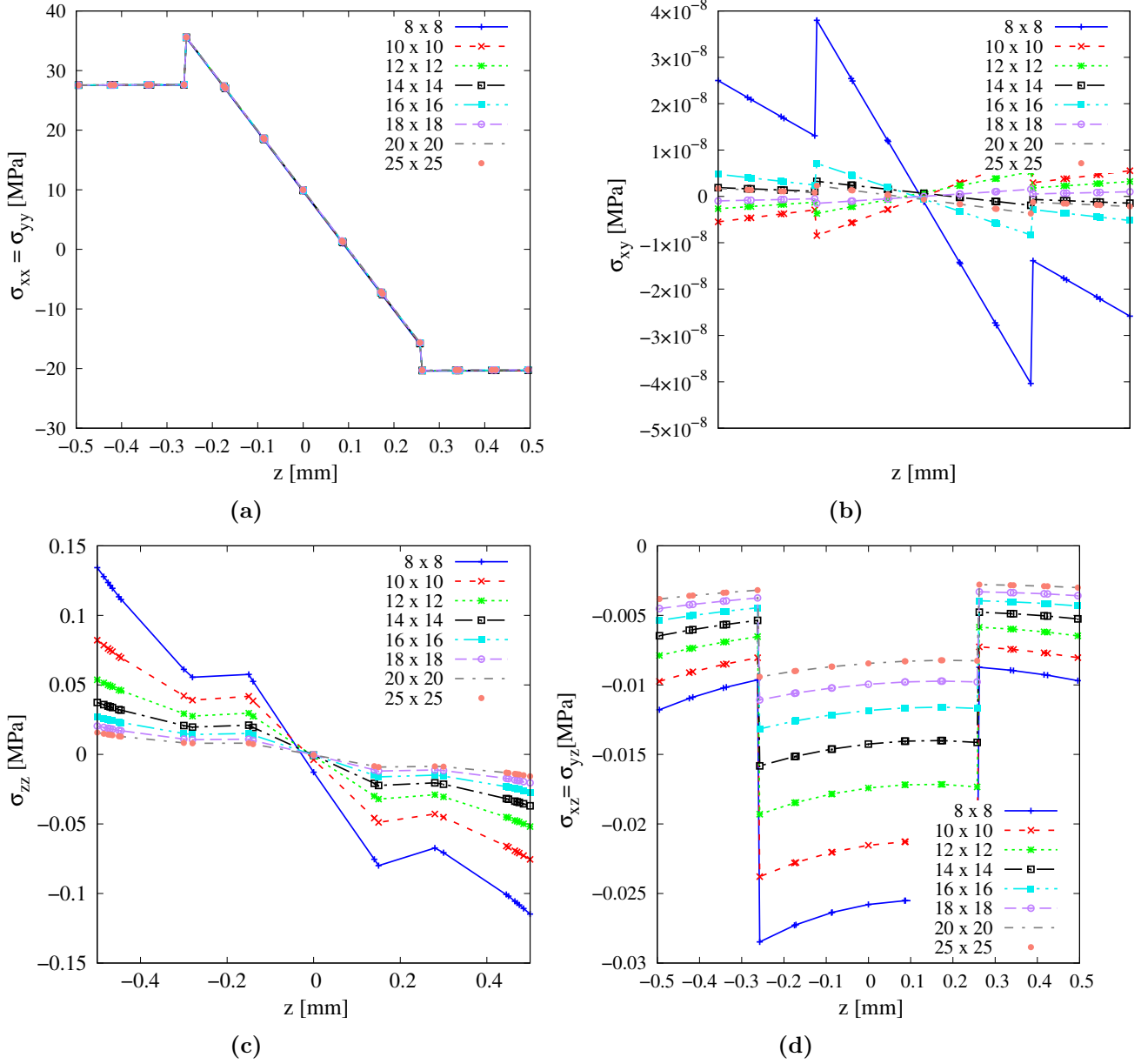


Figure 5.5: Thickness expansion: one LE3 for each layer, convergence study on surface mesh with Q9 elements. σ_{xx}, σ_{yy} (a), σ_{xy} (b), σ_{zz} (c), σ_{xz}, σ_{yz} (d), steel external material, aluminum internal material.

The graphs reported in Fig. 5.5 representing the results obtained with the 20×20 and with the 25×25 mesh discretizations are perfectly overlapped and it is clear that the convergence is reached with a 20×20 Q9 mesh discretization. The graphs in Figure 5.5 show that the plate is composed of three different layers (the two inner layers are considered as one single thicker layer) with two

interfaces and each stress figure displays a trend in which the interfaces are clear and easily visible. Some stress trends are not symmetric because of the different signs of the over-temperature on the external faces. Furthermore, it is important to consider the σ_{xy} behavior. The convergence analysis shows a fluctuating trend where the sign of the stress change at each analysis, even so, it reaches a convergence value by increasing the number of elements. It is important to consider that the value of the stress is too much lower than the others and it could be possible that some numerical problems are involved.

5.1.3 Convergence study of the expansion along the thickness

Following is presented a study about the in-thickness expansion functions. As explained in Section 2.4 the most diffused high-order theories are the ones that describe the along-the-thickness behavior through the Taylor or the Lagrange functions. In the present work, LE is chosen for exploiting the advantage of LW material description.

The Lagrange expansion functions can be of different orders and in the following work, the order of expansion that can better represents the thermal stresses is investigated. Following some results are reported for displacement convergence in Fig. 5.6 and stresses convergence in Fig. 5.7.

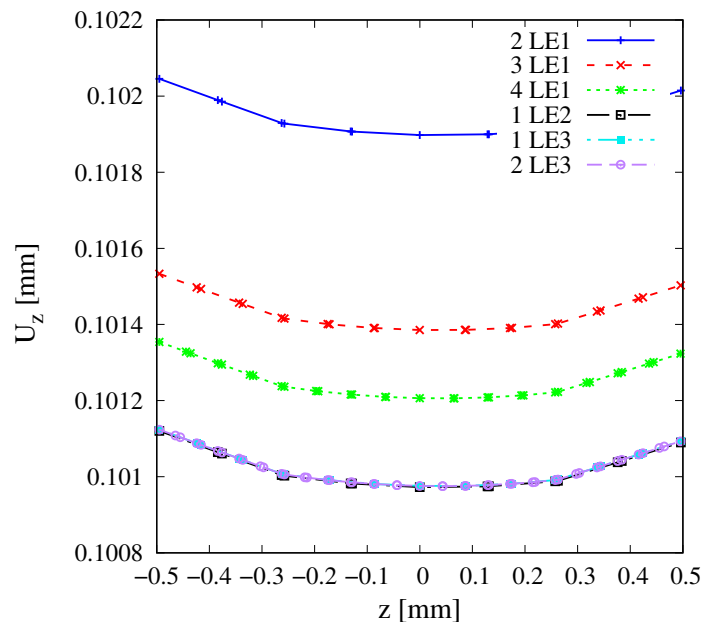


Figure 5.6: Convergence analysis with along the thickness theory LE1, LE2 and LE3, surface mesh 20×20 Q9. Displacement in z -direction. The legend is referred to the expansions used for each layer, steel external material, aluminum internal material.

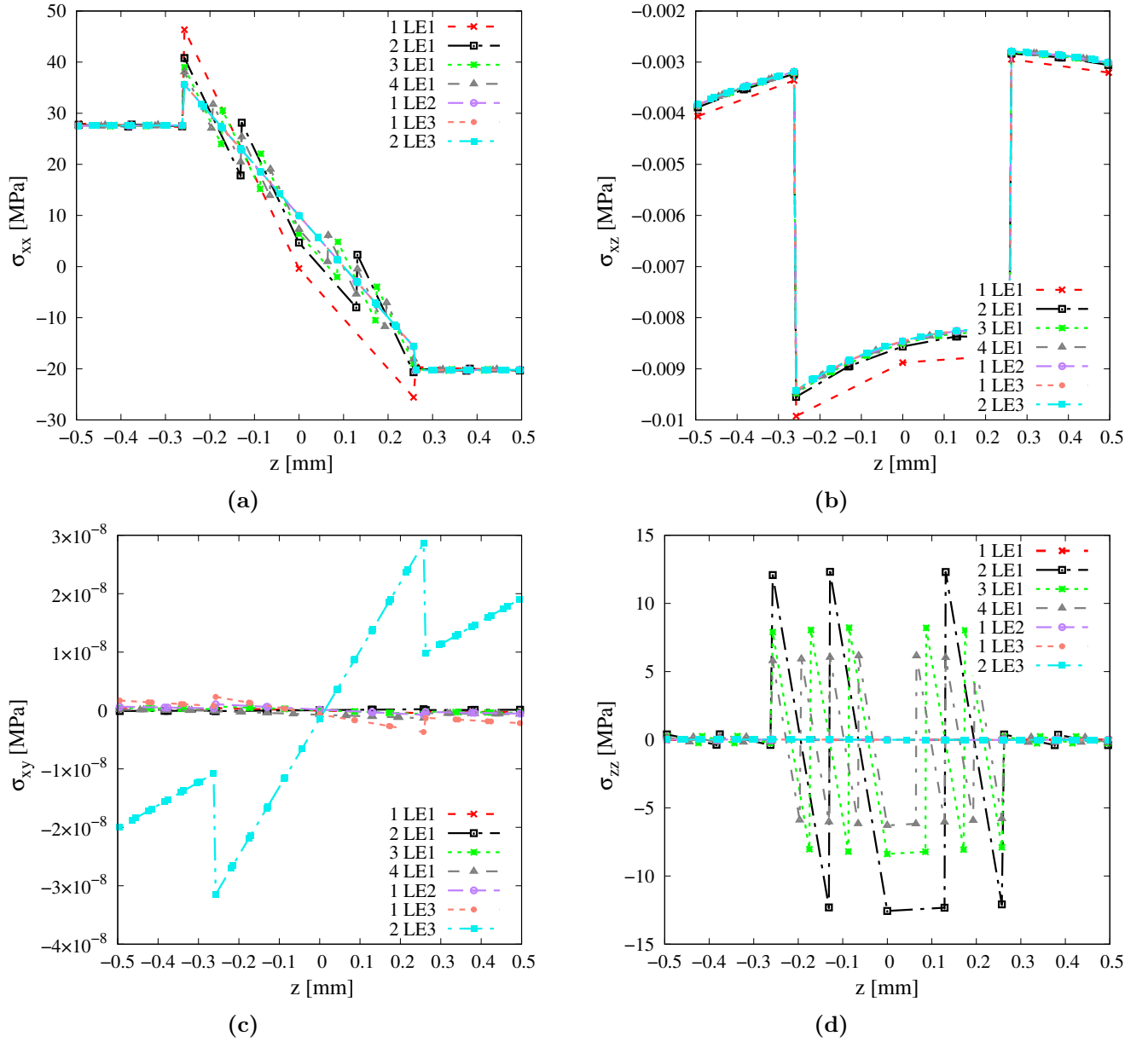


Figure 5.7: Convergence analysis with along the thickness theory $LE1, LE2$ and $LE3$, surface mesh 20×20 $Q9$. σ_{xx}, σ_{yy} (a), σ_{xz}, σ_{yz} (b), σ_{xy} (c), σ_{zz} (d). The legend is referred to the expansions used for each layer, steel external material, aluminum internal material.

The LE1 expansion can not easily reach a convergence. Furthermore, the linear slope imposed on the displacement from the LE1 causes a constant behavior of the stresses for each layer that are not realistic and can not fit the real stresses trend presenting the problems represented above with some oscillation around the solution. Particularly, considering the σ_{zz} stress trend is clear that a first order expansion introduces errors in the description reaching higher value with several orders of magnitude higher than the equilibrium results. It is clear that the LE3 in-thickness expansion is better than the others but good results are reached also using the LE2 element, for clearance the following graphs reported in Figure 5.8 are useful to determinate the best in-thickness expansion

configuration where all the LE1 functions are not reported.

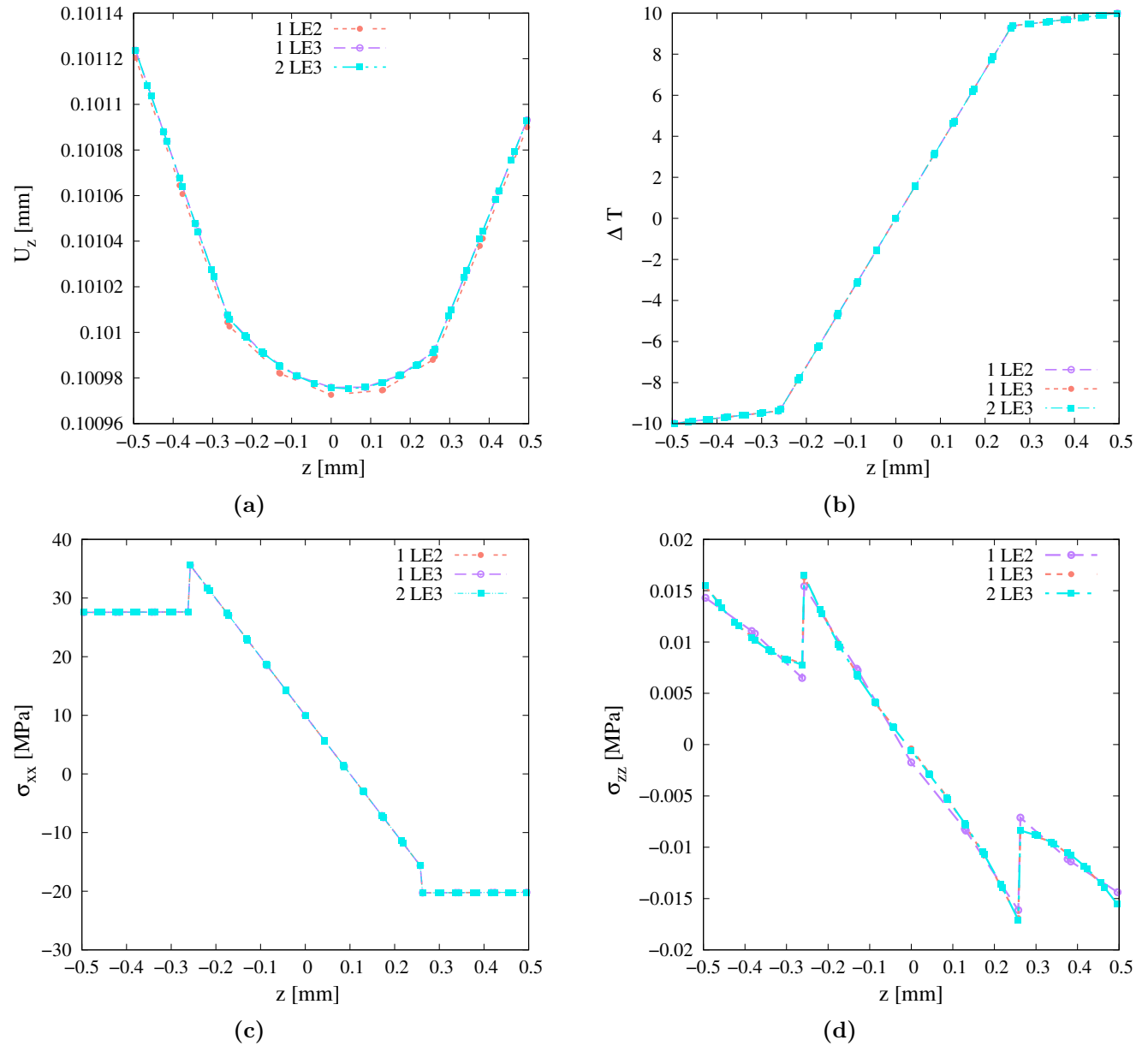


Figure 5.8: Convergence analysis with along the thickness theory LE2 and LE3, surface mesh 20×20 Q9. (a) Displacement, (b) Temperature profile, σ_{xx} , σ_{yy} (c), σ_{zz} (d). The legend is referred to the number of element used for each layer, steel external material, aluminum internal material.

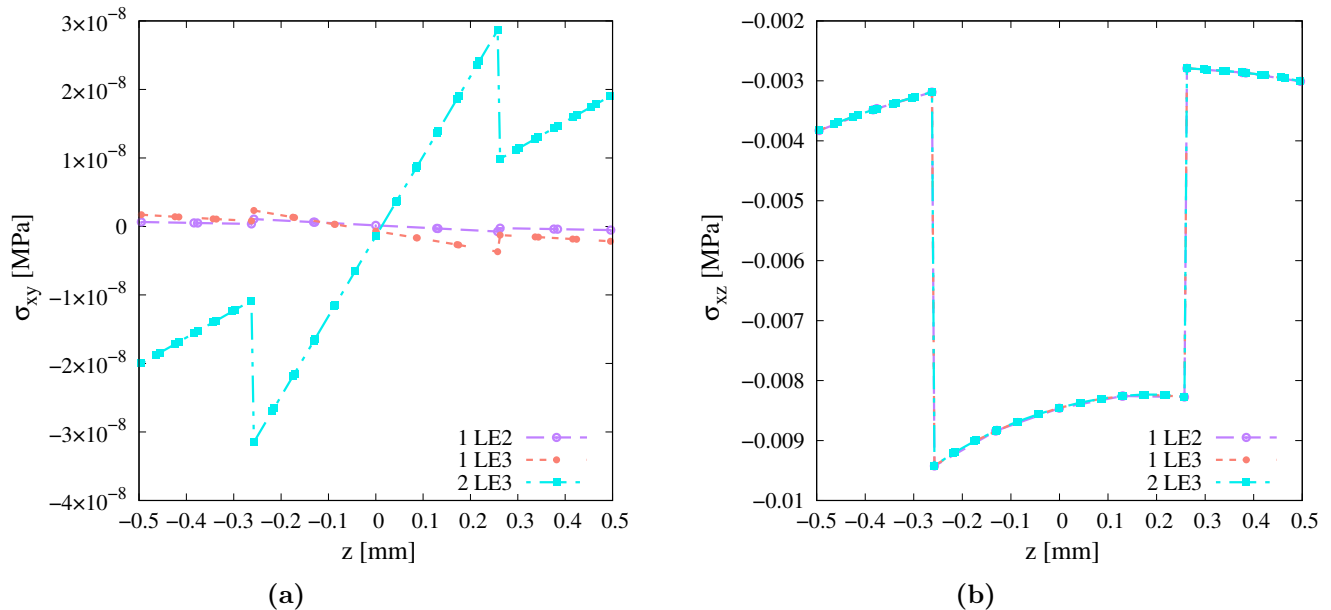


Figure 5.9: Convergence analysis with along the thickness theory LE2 and LE3, surface mesh 20×20 Q9. σ_{xy} (a), σ_{xz} (b). The legend is referred to the number of element used for each layer, steel external material, aluminum internal material.

Some analyses about the convergence of the in-thickness expansion are carried out by [28] and demonstrate also in [29]: at least a parabolic expansion for the displacements (u, v, w) is required to capture the linear thermal strains that are related to linear through-the-thickness temperature distribution. In the present work a thin plate composed of metallic material is considered and clearly, the temperature profile will be linear also increasing the accuracy of the in-thickness discretization. Considering a thicker plate with a less conductive material, it is possible to describe the change in the shape of the temperature profile. A study with a decoupled approach can be carried out for the studied plate using a Fourier description but also an assumed linear temperature profile permit to obtaining good results. Considering all the reported results the better modelization configuration is given using a 20×20 Q9 in-plane mesh and one LE3 expansion for each layer.

5.1.4 Best mesh results 20×20 1 LE3 each layer

As clear from the results above, the best analysis is given by a mesh with 20×20 elements where increasing the number of elements, results do not change and, only the computational cost increases. The best results are reported in Figure 5.10, only some stresses results, not clear in the previous graphs are represented.

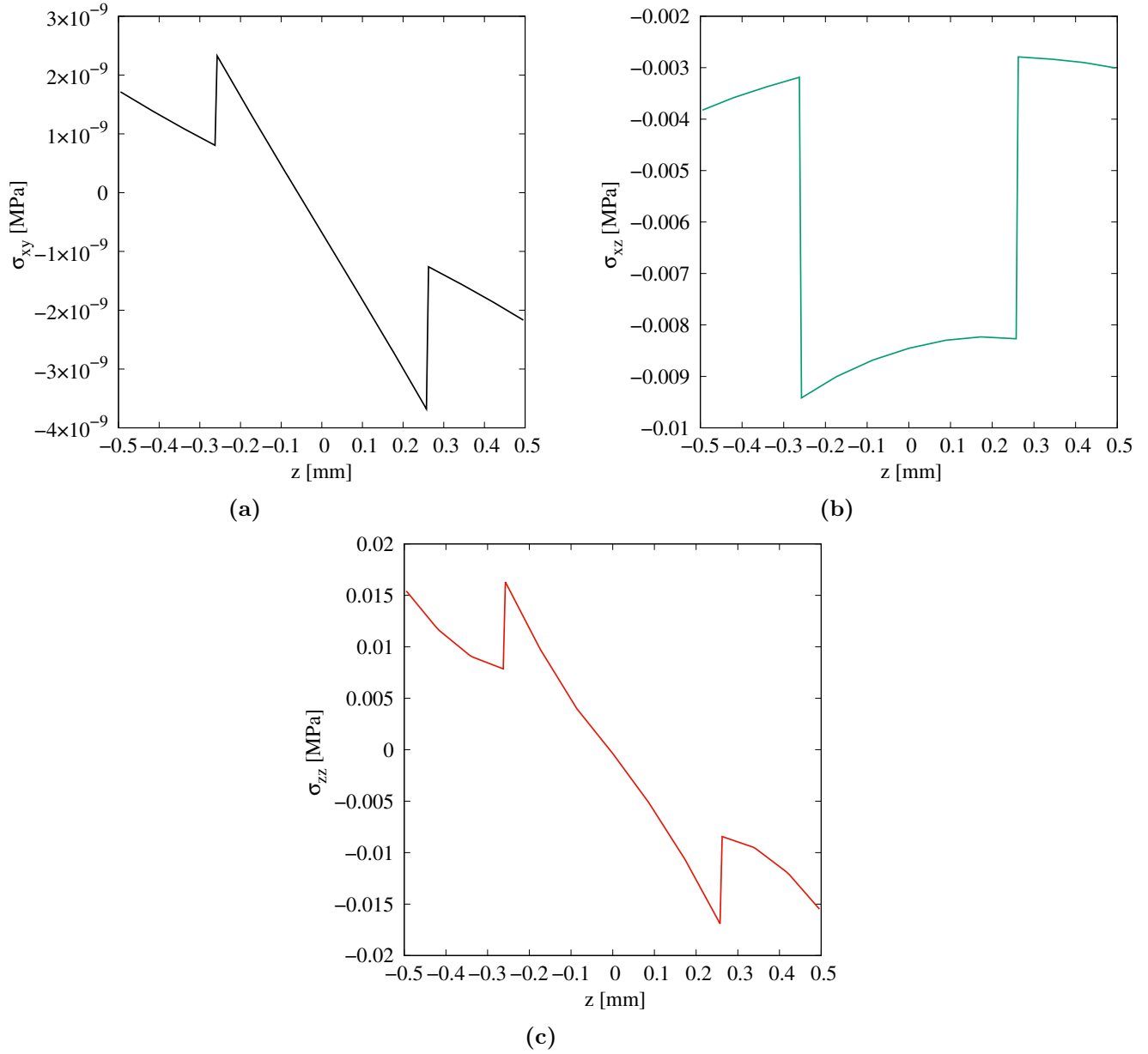


Figure 5.10: Results with along the thickness theory 1 LE3 for each layer, surface mesh 20x20 Q9. σ_{xy} (a) , $\sigma_{xz} = \sigma_{yz}$ (b), σ_{zz} (c).

5.2 Decoupled and coupled thermo-mechanical analysis of composite multilayered plate

In the present section, the same geometrical configuration is analyzed both with the decoupled and coupled approaches and the main results are reported below. The analyzed plate is a four-layer square plate with lamination $[0^\circ/90^\circ/90^\circ/0^\circ]$ (rotation angle with respect to the ' x' ' axis). The pinned plate is composed of carbon-epoxy material whose properties are reported in Table 5.3. The

constraints are imposed on all the lateral surfaces. The over-temperature is constant over all the plate surface (x, y) and is $\theta = 1$ for the decoupled analysis and $\theta_b = -1^\circ$, $\theta_t = 1^\circ$ for the coupled one. To make a comparison between the two approaches, in the decoupled analysis section some results about the same configuration (geometry and BCs) analyzed with the coupled approach are reported.

The edges dimensions are $a=b=50$ mm and $\frac{a}{h}=50$ with a thickness of 1 mm. In order to compare and validate the analysis a numerical model created with ABAQUS is used.

Both the analyses, the coupled and decoupled ones are done with the same software, and the model is created using 3D elements. A shell modelization can not permit the representation of the along-thickness stresses trend, particularly because the FSDT (implemented in the numerical common software) theory considers the ' z '- direction strains equal to zero, and the imposition of a plane stress condition is imposed to avoid numerical problems. Due to the thermal external load and the value of the thermal expansion coefficients reported in Tab. 5.3 the along-the-thickness strain is the more influential component and determines the deflection and the stresses. The mentioned hypotheses imply the useless comparison between the simple shell approach and the CUF method that can represent the in-thickness behavior with LE along the thickness. For the reported reasons a 3D approach for the ABAQUS model is preferred in the following work to reach a better comparison with the present method results. The used material properties are reported in Table 5.3.

Table 5.3: *Material coefficients taken from [5]*

Carbon/Epoxy	coefficients
E_{11}	250000 MPa
E_{22}	10000 MPa
E_{33}	10000 MPa
ν_{12}	0.25
ν_{13}	0.25
ν_{23}	0.25
G_{12}	5000 MPa
G_{13}	5000 MPa
G_{23}	2000 MPa
α_1	$1.0 \times 10^{-6} K^{-1}$
α_2	$1125.0 \times 10^{-6} K^{-1}$
α_3	$1125.0 \times 10^{-6} K^{-1}$
K_{11}	36.42 W/(mK)
K_{22}	0.96 W/(mK)
K_{33}	0.96 W/(mK)

5.2.1 Decoupled approach

For a decoupled study, considering a global external temperature assumed homogeneous through the whole plate an assumed constant profile is imposed along the thickness without any errors. A convergence study is carried out to reach better mesh discretization and is reported in Table 5.4.

5.2. DECOUPLED AND COUPLED THERMO-MECHANICAL ANALYSIS OF COMPOSITE MULTILAYERED PLATE

Table 5.4: Convergence study using the present method. The displacement and the stresses are taken in the center of the palate and $z=\pm h/2$.

Mesh [Q9]	10x10	20x20	30x30	40x40	46x46
u_z [mm]	$\pm 0.7051 \times 10^{-3}$	$\pm 0.7052 \times 10^{-3}$	$\pm 0.7051 \times 10^{-3}$	$\pm 0.7051 \times 10^{-3}$	$\pm 0.7051 \times 10^{-3}$
σ_{xx} [MPa]	-3.264	-3.173	-3.144	-3.131	-3.126

From the results reported in Table 5.4, a mesh of 30×30 is chosen to ensure a good convergence of the analysis using the present method. It is clear that the displacement and the good trend of the stresses are reached. For the sake of clearance, the convergence stresses trends are reported following in Figure 5.11.

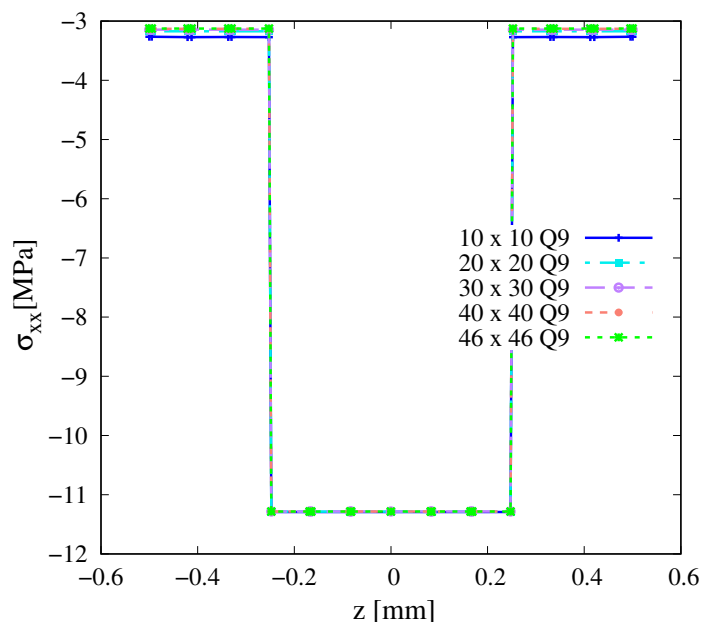


Figure 5.11: σ_{xx} convergence study graphical representation. Decoupled analysis carried out by the present method.

The same convergence analysis is done for the ABAQUS problem and is reported in Table 5.5 where displacements and σ_{xx} are reported with the relative number of elements and DOFs to evaluate its computational cost.

Table 5.5: Convergence study in ABAQUS. The displacement and the stresses are taken in the center of the plate and $z=-h/2$.

Number of elements	120000	1280000	3000000
u_z [mm]	-0.70787×10^{-3}	-0.70509×10^{-3}	-0.70509×10^{-3}
σ_{xx} [MPa]	-3.12204	-3.12193	-3.12166
DOFs	1575639	4341627	9789039

The ABAQUS analysis is carried out by modeling the entire plate imposing a zero-degree temper-

ature predefined field in the initial step and modifying the field in the second step to one degree. The thermal load is applied on the entire plate and a simple 3D static analysis is carried out. The high DOFs number and the analysis computational cost do not permit increasing the element number. However, the number of elements used for the analysis is determined to obtain accurate results with a realistic computational cost and is superfluous to reduce the element dimensions. Considering the results reported in Table 5.5, the second case reported, with 1280000 elements is chosen and the analysis results are following reported in Fig.s 5.12, 5.13, 5.14 and Tab. 5.6. The choice is mandatory because the first analysis can not be considered, indeed, some numerical problems occur due to the elements' dimensions that are not cubic. Furthermore, the third analysis from Table 5.5 presents a bigger computational cost with few advantages.

It could be interesting to compare the degrees of freedom present in the ABAQUS model and the DOF of the present method necessary to have realistic results. The number of variables present in the ABAQUS model is 4341627 to obtain satisfactorily and adhere to the true most of the results. The present model can carry out a realistic representation of the phenomena with 145119 DOF. As expected, from the reported example is clear that the use of the present method with the in-thickness expansion permits a good representation of the phenomena with a lower computational cost than a 3D approach. The classical 2D simple approach is too simplistic to obtain realistic results but the 3D analysis is very heavy for the analysis of a laminate plate. The use of the present method permits carrying out a plate approach analysis with an along-the-thickness expansion that can explain the shear and in-thickness structure behavior. The results trends are reported in the graphs below in Fig.s 5.12, 5.13, 5.14 and some punctual values are collected in Table 5.5.

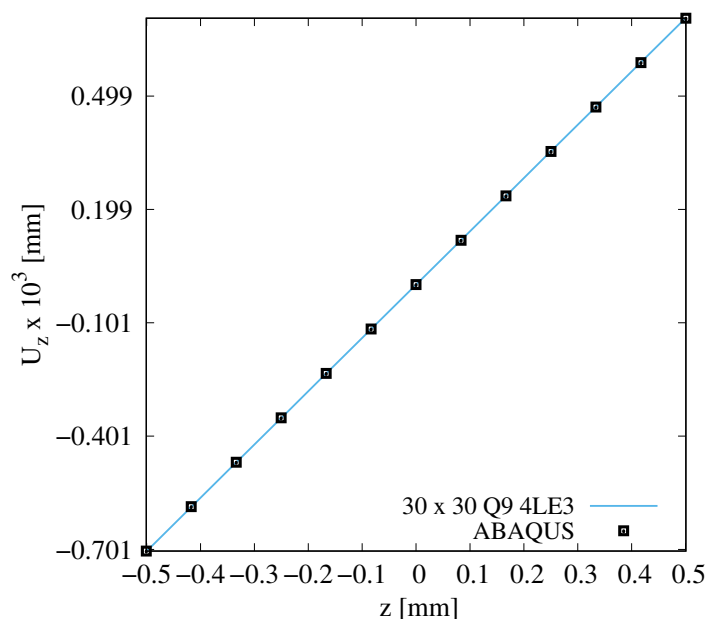


Figure 5.12: Displacement z -direction. Comparison between 30×30 Q9 with thickness expansion 1 LE3 each layer and ABAQUS analysis.

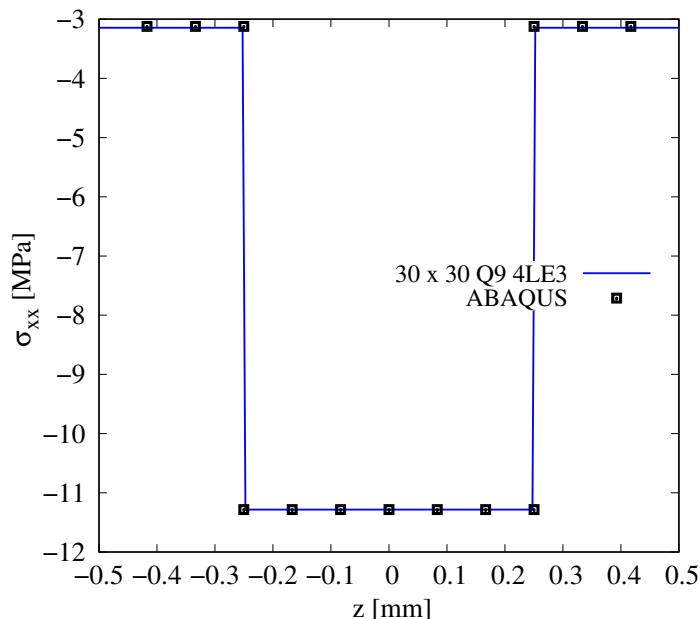


Figure 5.13: σ_{xx} . Comparison between 30 x 30 Q9 with thickness expansion 1 LE3 each layer and ABAQUS analysis.

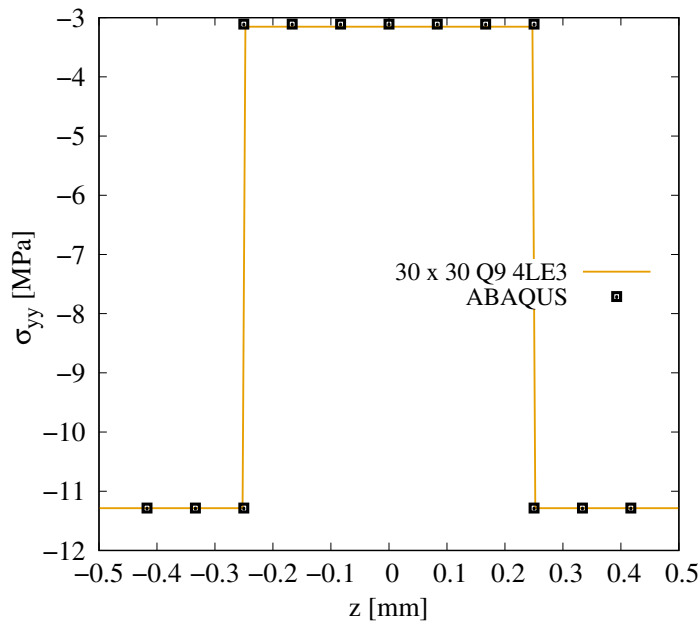


Figure 5.14: σ_{yy} . Comparison between 30 x 30 Q9 with thickness expansion 1 LE3 each layer and ABAQUS analysis.

The decoupled approach is used to analyze a plate with a constant temperature profile representing a global over-temperature around the whole plate. Shear stresses are neglectable with respect to the axial one (and could be subjected to numerical problems) and there are not reported in the graphs. From the stress trends presented in Figures 5.13, 5.14, it is clear the position of the

5.2. DECOUPLED AND COUPLED THERMO-MECHANICAL ANALYSIS OF COMPOSITE MULTILAYERED PLATE

interfaces of the different layers, is also clear that the same orthotropic material, used with different orientations has different properties. As expected, the stresses trend are both negative, the sign of the axial stresses could be an indicator of the good trend of the analysis. Indeed, the material with a positive expansion coefficient, with an increase in the applied temperature, tends to expand and is subjected to a stress compression state. Considering the present lamination which is symmetric and the symmetrical BC configuration it is clear that the stress trends are symmetrical concerning the middle plane of the plate. The z displacement, instead, is not symmetric because the plate presents the same displacement value but with an opposite sign considering two points equally distanced from the middle plane. The difference in the displacement sign is caused by the constant temperature applied on the plate and by the constraints that blocked the deflection out of the plane. The present case can be analyzed also through a coupled approach and the two analyses have to be about the same results considering that the coupled calculated temperature profile has the same path as the one imposed in the decoupled and the coupling terms are small. Consequentially, the same analysis is carried out with a coupled approach and the main results are reported in Table 5.6. Present method results are reported for coupled and decoupled analyses and are compared to the ABAQUS results for both cases. Also, the DOFs of each analysis are reported to evaluate the computational cost.

In a coupled analysis, the thermal profile along the thickness is calculated in the analysis but the present particular thermal boundary condition imposes a constant thermal profile independently from the material conductivity.

Table 5.6: Comparison between coupled and decoupled approaches applied to the same plate.

		Decoupled		Coupled	
		30 x 30 Q9 4LE3	ABAQUS 3D	30 x 30 Q9 4LE3	ABAQUS 3D
$u_z[mm]$	$z = -h/2$	-0.70510×10^{-3}	-0.70509×10^{-3}	-0.70513×10^{-3}	-0.70510×10^{-3}
	$z = 0$	0	0	0	0
	$z = +h/2$	0.70510×10^{-3}	0.70509×10^{-3}	0.70513×10^{-3}	0.70510×10^{-3}
$\sigma_{xx}[MPa]$	$z = -h/2$	-3.1440	-3.1216	-3.1440	-3.1385
	$z = 0$	-11.2844	-11.2831	-11.2844	-11.2844
	$z = +h/2$	-3.1440	-3.1216	-3.1440	-3.1385
$\sigma_{yy}[MPa]$	$z = -h/2$	-11.2847	-11.2828	-11.2847	-11.2838
	$z = 0$	-3.1529	-3.1096	-3.1529	-3.1308
	$z = +h/2$	11.2847	-11.2828	-11.2847	-11.2838
DOFs		145119	4341627	193492	5788836

As expected and clear from Table 5.6, a decoupled approach is preferred over a coupled one. The results are the same but in the coupled analysis the DOFs increase with the relative computational

cost without any improvements in the accuracy of the results. The considerations due to the results collected in Table 5.6 are important for the following analyses. Indeed, they allow us to choose the better approach for the following problems.

5.2.2 Coupled approach

In the coupled analysis reported in the present subsection, only imposed over-temperature is used and the temperature profile becomes a variable of the problem. Consequentially, no explicit dedicate equation is solved and the constitutive eq.s 2.12 and 2.11 are considered. The BCs are different from the previous analysis, and due to the different external load the results of the last two analyses (Subsection 5.2.1 and 5.2.2) are not comparable to compare the two approaches. The displacement and stress results, both, from the present method and ABAQUS, are reported below. For the first analysis, a convergence study is carried out and a mesh grid of 30×30 elements is taken to ensure the convergence of the solution as represented in Table 5.7.

Table 5.7: *Convergence study using the present method. The displacement is taken in the center of the plate and $z = 0$, σ_{xz} in the point C (-12.5, -12.5) mm, reference system reported in Figure 5.16.*

Mesh [Q9]	10x10	20x20	30x30	40x40
u_z [mm]	-0.5411×10^{-3}	-0.3153×10^{-3}	-0.2403×10^{-3}	-0.2037×10^{-3}
σ_{xz} [MPa]	1.592×10^{-3}	-3.218×10^{-3}	-2.145×10^{-3}	-1.896×10^{-3}

From the results in Table 5.7 is clear that there is a good convergence trend. It is possible to use the 30×30 results considering a trade-off between the lower computational cost and good results along the thickness. Following in Figure 5.15 the representation of the displacements and stresses convergence is reported for explaining graphically the necessity to use at least the 30×30 mesh discretization. Differently than the analysis in Section 5.2.1 the σ_{xz} stresses are reported for a convergence analysis due to the type of deflection caused by the different BCs.

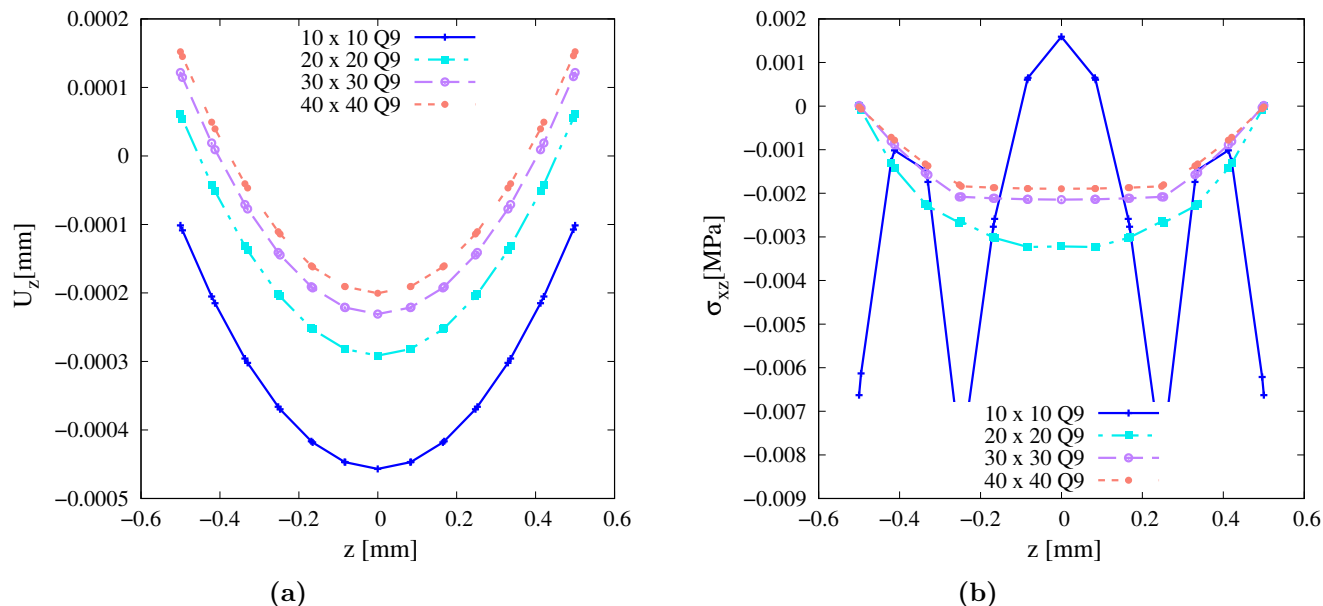


Figure 5.15: Convergence study graphical representation. Coupled analysis carried out by the present method, (a) u_z , (b) σ_{xz} .

Increasing the analysis number of the finite elements could allow for obtaining a result close to the realistic behavior of the plate. However, there is little difference between the chosen results and the more accurate one which makes the increase in computational cost unnecessary. Reporting the 10×10 mesh results, some problems are clear considering the stresses trend, particularly, the shear stresses have to be zero in the boundary of the plate but in the first discretization case it not occurs. As clear also from the table, a good trade-off in the results is present considering the 30×30 mesh discretization. Furthermore, from Figure 5.15 (b) it is clear that 10×10 mesh is not enough for the shear stresses representation, and only from the 30×30 mesh the interfaces between the layers are represented. Figures 5.17, 5.18, 5.2.2, 5.2.2, 5.22, 5.22 will represent the results taken from the present analysis.

The setup of the ABAQUS analysis is different from the previous analysis. A *Coupled Temp-Displacement* analysis is achieved and relative finite elements are selected, a zero predefined field is imposed in the first step and thermal BCs are introduced in the analysis field. The software solved both the thermal and mechanical problems in a coupled manner. Therefore, the over-temperature profile is presented as a result taken from the analysis. The mesh discretization is the same as the previous analysis but the DOFs increase due to the presence of the temperature as unknown. The stress results are taken from the point $C = (-12.5, -12.5)mm$ considering the reference system reported in Figure 5.16. Instead, displacement and temperature results in Fig.s 5.16 5.17 are taken in the point $O=(0,0)$.

5.2. DECOUPLED AND COUPLED THERMO-MECHANICAL ANALYSIS OF COMPOSITE MULTILAYERED PLATE

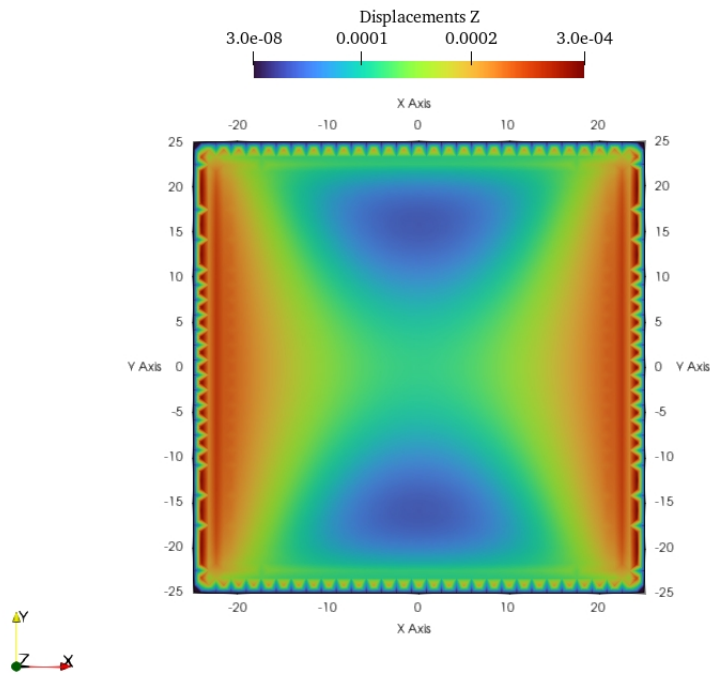


Figure 5.16: Displacement taken from present analysis reported in mm. Coupled approach.

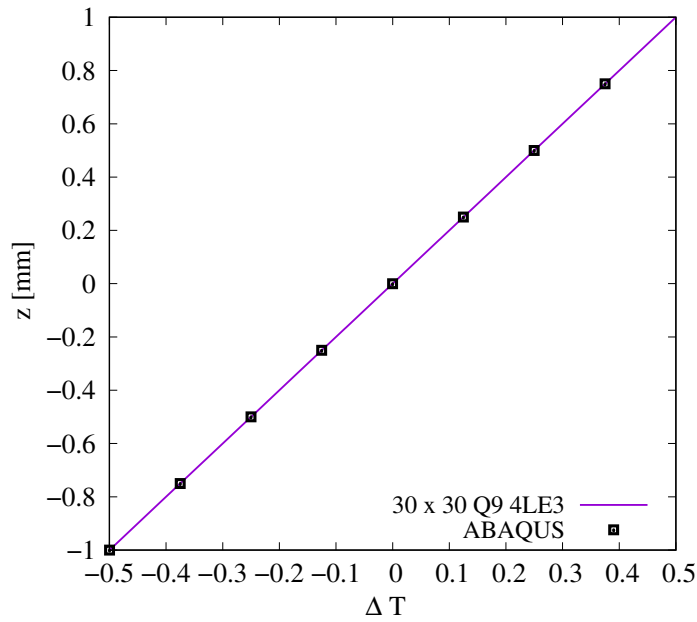


Figure 5.17: Over-temperature profile from point O. Comparison between the present method with thickness expansion 1 LE3 each layer and ABAQUS analysis.

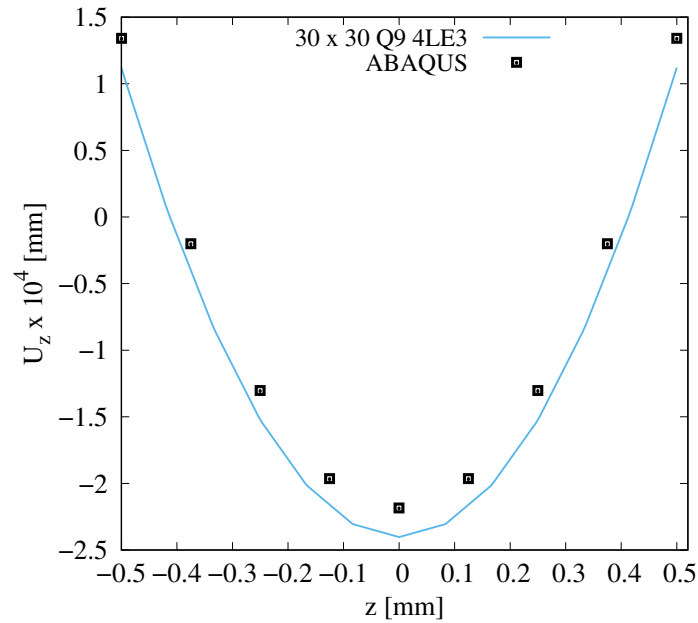


Figure 5.18: Displacement along the thickness from point O. Comparison between the present method with thickness expansion 1 LE3 each layer and ABAQUS analysis.

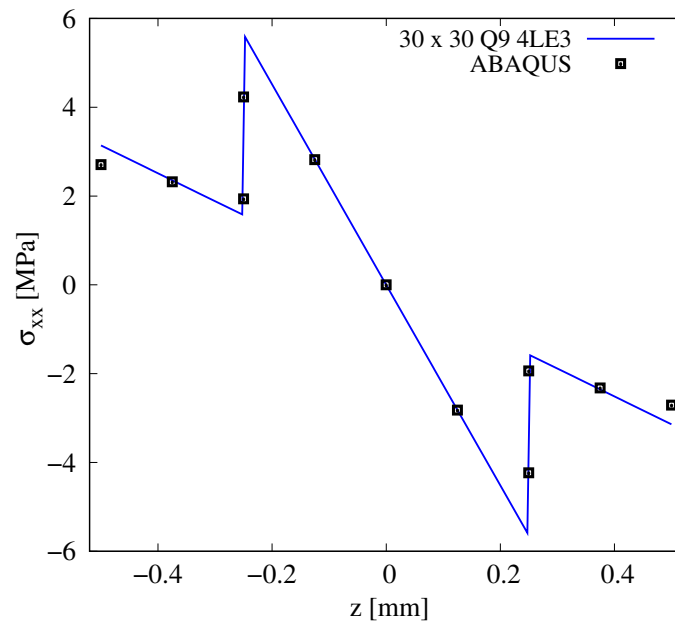


Figure 5.19: σ_{xx} along the thickness from point C. Comparison between the present method with thickness expansion 1 LE3 each layer and ABAQUS analysis.

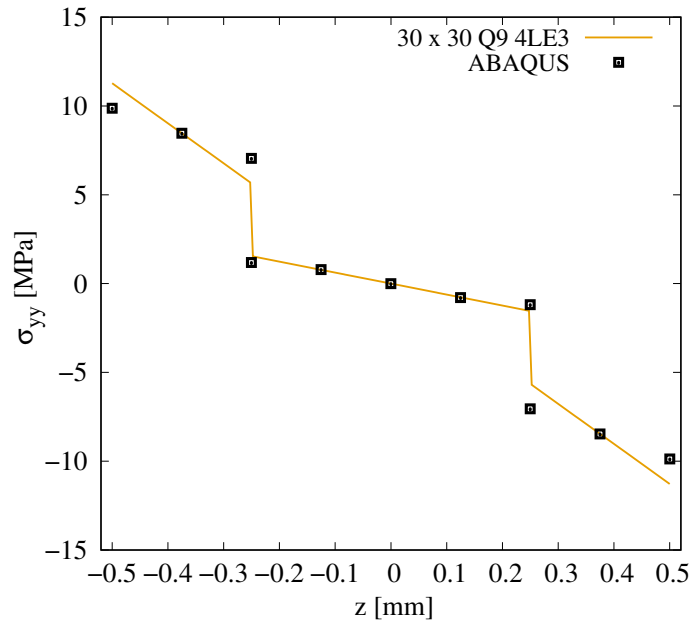


Figure 5.20: σ_{yy} along the thickness from point C. Comparison between the present method with thickness expansion 1 LE3 each layer and ABAQUS analysis.

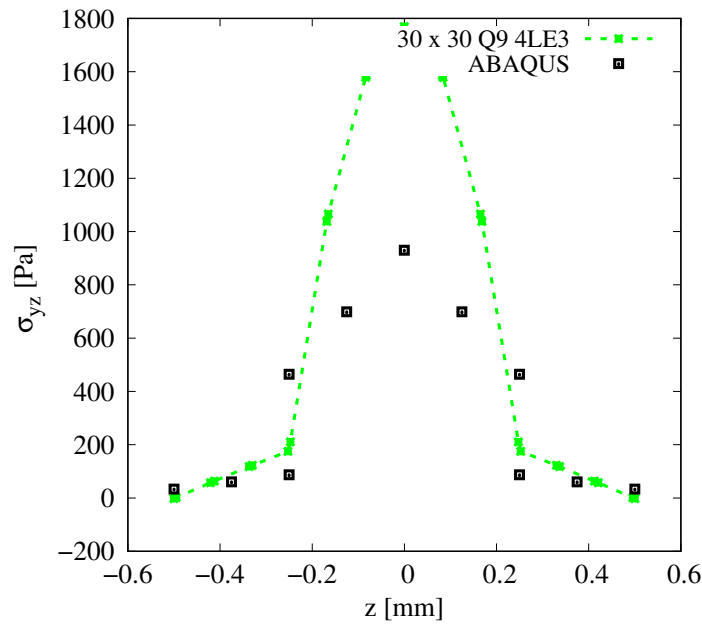


Figure 5.21: σ_{yz} along the thickness from point C. Comparison between the present method with thickness expansion 1 LE3 each layer and ABAQUS analysis.

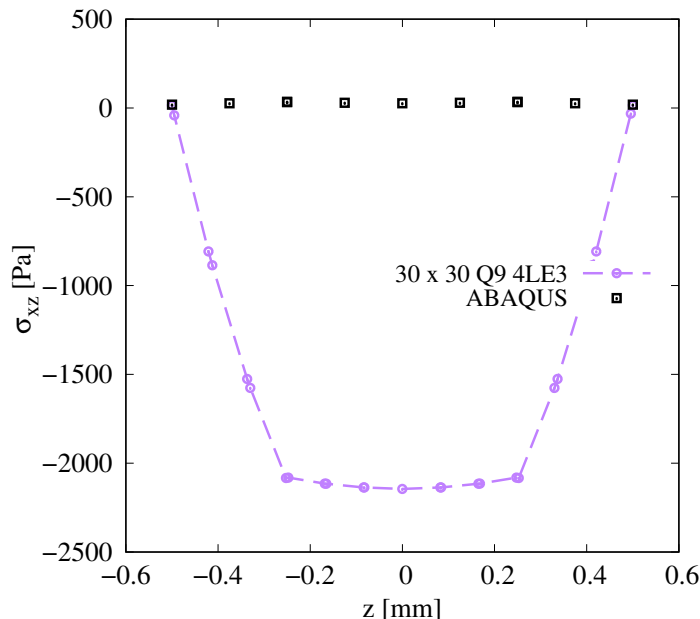


Figure 5.22: σ_{xz} along the thickness from point C. Comparison between the present method with thickness expansion 1 LE3 each layer and ABAQUS analysis.

The coupled analysis allows for obtaining clear results of the plate behavior under thermal load. Particularly, the temperature profile is linear also solving the coupled equations because of the thin plate and the high conductivity of the material. Moreover, the in-thickness conductivity is the same for all the layers.

Some shear and along-the-thickness stresses are not represented because of their little value. The only represented shear stress are the σ_{yz} in Fig. 5.21 and σ_{xz} in Fig. 5.22. It is clear from stress behavior that, the σ_{yz} path is the same as the one obtained with ABAQUS but, the difference is the entity that is bigger in the present analysis. The mentioned difference is caused by the better representation of the thermal shear stresses done by the present method. In the case of σ_{xz} in Fig. 5.22 the reported stress makes evident the difference between ABAQUS and present method results. As evident from Figures 5.21 and 5.22 the 3D ABAQUS model is more rigid than the one represented with the present method and implies that in the first case, the stresses are underestimated. More clear is the σ_{xz} trend where the stress behavior in the ABAQUS model is nearly zero instead, through the present analysis it is possible to have a non-zero value. The ABAQUS model is done with solid elements but due to the low value of the plate thickness, only one layer of elements for each lamina is used for the analysis. Therefore, the shear behavior along the thickness is not well represented. In the center of the plate, where the bending reached the maximum value, the shear stresses are approximately null but in point C where the stresses are represented, the bending is minimized and the stresses are not zero as represented with the present method results.

As clear from the displacement, the plate is subjected to a bending deflection with a maximum in the center of the plate. Therefore, the stresses are about zero in the center of the plate.

The results reported in Table 5.6 and in Figure 5.16 allow us a consideration. Due to the bending deflection of the present analysis, a buckling analysis makes more sense for the BCs configuration used in Section 5.2.1 where bending is not present.

Chapter 6

Thermo-mechanical and thermo-buckling analyses of VAT composite plate

In the present chapter, some analyses on VAT laminated material are reported. As described in Chapter 4, VAT composites are new layered materials that are more and more of interest in the aerospace field. The increase in the stacking degrees of freedom permits the improvement of the quality of the final product by exploiting the new production techniques and adapting the properties to the ultimate use of the structure and the applied type of load.

In order to validate the VAT integration approach used in the following analyses, a pure mechanical analysis is done and the results are reported in Section 6.1. Moreover, the buckling critical temperature of the plate is investigated and compared with the reference [12] in Section 6.3. At the end of the present chapter, optimum orientation for retarding buckling is investigated for Carbon/Epoxy and E-Glass/Epoxy laminates, and relative stresses are reported.

6.1 Pure mechanical static analysis for VAT composites

In the present section, a validation analysis for a simple static analysis on VAT composite material is carried out with the present method. Geometry and BCs are taken from [4] which is used as literature to compare the results. The pure mechanical analysis for the VAT problem is investigated to validate the increase in the complexity of the numerical description.

The analyzed structure is a square plate with edge $a = b = 1m$ with a $h = 0.1m$ thickness. The two layers are composed of a Graphite/Epoxy composite whose properties are reported below, the plate is simply supported along the whole four edges and there is an applied external mechanical pressure equal to $P_z = 10kPa$. The material properties are $E_1 = 137.9GPa$, $E_2 = E_3 = 8.96GPa$, $G_{12} = G_{13} = 7.1GPa$, $G_{23} = 7.1 GPa$, $\nu_{12} = \nu_{13} = 0.3$, $\nu_{23} = 0.49$ and the present lamination is $[0 < 90, 45 >, 0 < 0, 45 >]$ where, referring to the VAT presentation in the Chapter 4 the first layer has $\Phi = 0$, $T_0 = 90$ and $T_1 = 45$. The lamination graphical representation is reported in Figure 6.1. The referring results are taken in the point $Q = (-0.25, -0.25)[m]$ with respect to the central reference system reported in Figure 6.2.

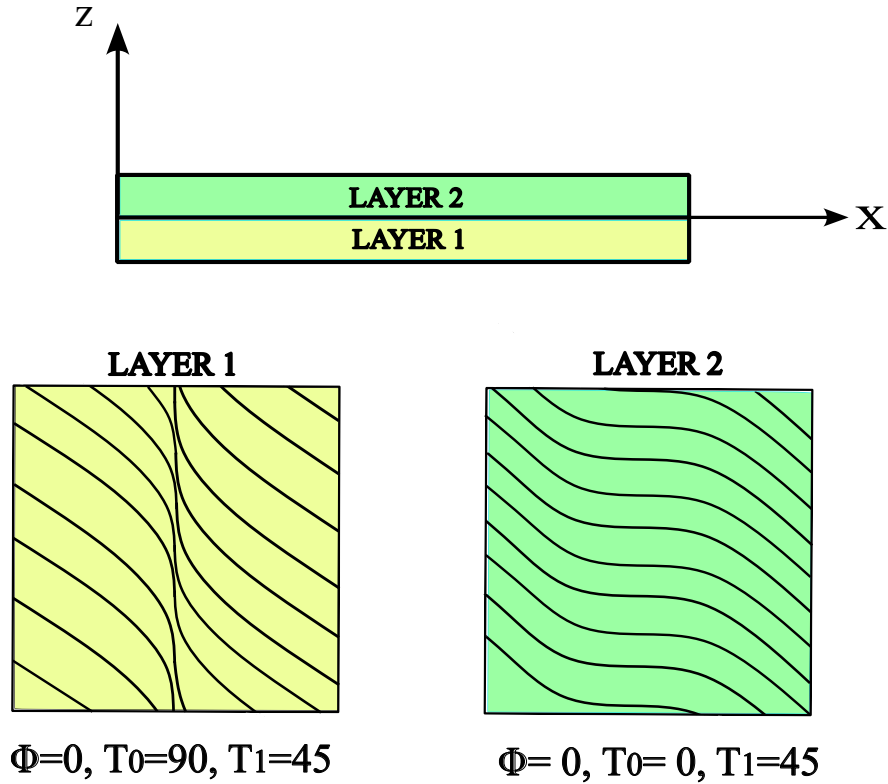


Figure 6.1: *VAT stacking sequence representation.*

The deflected configuration of the plate is reported in Figure 6.2. As expected, the pressure generates a downward deflection with a maximum in the central part of the plate.

Following, the results obtained with the present analysis are reported and compared to the literature [4]. The convergence of the results is reached with a 14×14 Q9 in plane mesh with an in-thickness expansion of 1 LE3 for each layer. The comparison is done both, with the graphs reported in Fig. 6.4 and comparing the stresses value in some datum points of the plate which results are collected in Tables 6.1 and 6.2. The Table collects the NX Nastran results of the literature and the present method analysis in some different points. The graphs in Figure 6.4 report the trend of the present method analysis and the literature one with respect to a z dimensionless coordinate. In Figure 6.2 the deflection in z -direction is reported taken from the present analysis with the relative reference system.

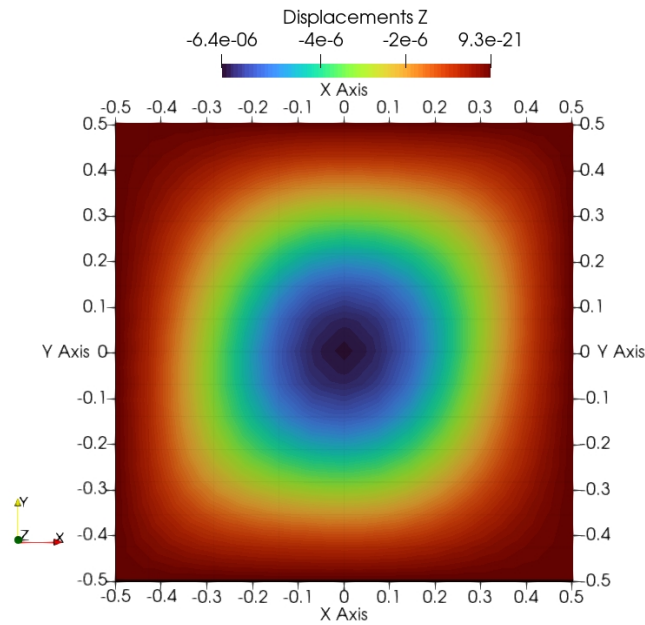


Figure 6.2: z -displacement [m] simply supported, two layers, plate. External pressure 10kPa, in plane mesh of 14 x 14 Q9 elements, 2LE3 along the thickness. $[0 < 90, 0 >, 0 < 0, 45 >]$.

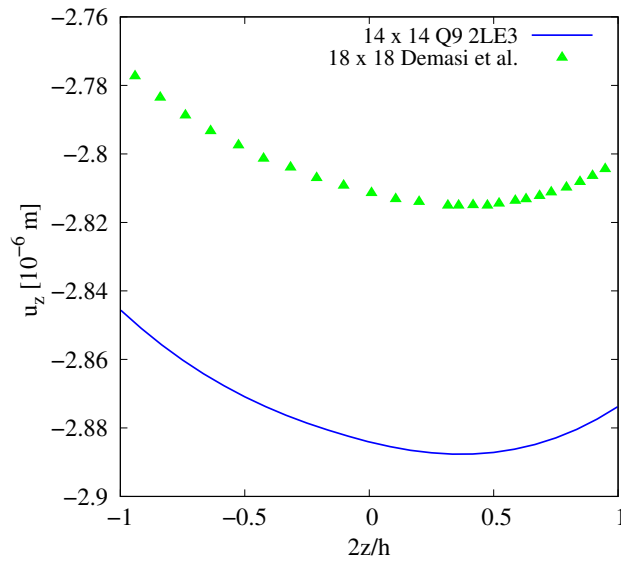


Figure 6.3: Displacement along z -direction. Comparison between the present method using a mesh 14 x 14 Q9 along the thickness expansion 2LE3 and references results [4].

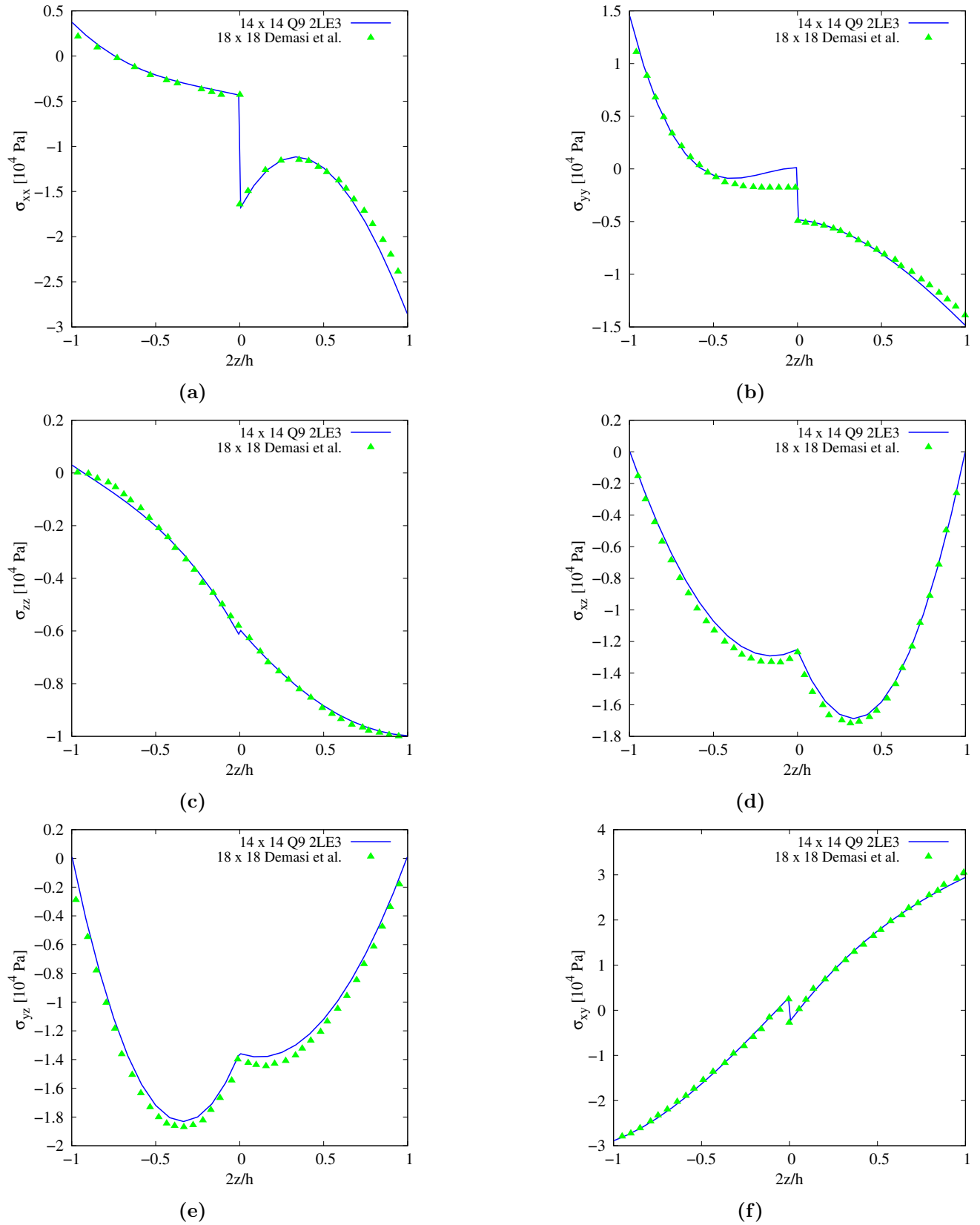


Figure 6.4: $\sigma_{xx}(a), \sigma_{yy}(b), \sigma_{zz}(c), \sigma_{xz}(d), \sigma_{yz}(e), \sigma_{xy}(f)$ comparison between the present method using a mesh 14×14 Q9 along the thickness expansion $2LE3$ and references results [4].

As clear from the graphs reported in Figure 6.4, the stress trend of the present analysis overlaps the literature results with a good approximation. The reference results are obtained using a unified formulation with triangular (TRIA) finite element with 15 nodes. Some differences in the element stiffness could be present in the comparison particularly because a TRIA element could be stiffer than a QUAD one. The following Tables 6.1, 6.2 permit us to compare the present analysis results to NX NASTRAN ones present in the Demasi et al. [4]. In the reference case the analysis is done with 3D solid elements, details are not here reported.

Table 6.1: *Simply supported square plate displacement results comparison with respect to the literature [4]. Results taken in the point Q at datum thickness position.*

	u_x	u_y	u_z
$2z/h$	-0.72	-0.79	0.37
NX NASTRAN [4] [m]	-5.0572×10^{-7}	-0.5477×10^{-7}	-2.8237×10^{-6}
14 x 14 Q9 2LE3 model [m]	-5.0588×10^{-7}	-0.5393×10^{-7}	-2.8876×10^{-6}

Table 6.2: *Simply supported square plate stresses results comparison with respect to the literature [4]. Results taken in the point Q at datum thickness position.*

	σ_{xx}	σ_{yy}	σ_{zz}	σ_{xz}	σ_{yz}	σ_{xy}
$2z/h$	0.53	0.89	0.79	0.32	-0.32	0.74
NX NASTRAN [4] [10^4 Pa]	-1.3239	-1.2726	-0.9822	-1.7198	-1.8697	2.3835
14 x 14 Q9 2LE3 model [10^4 Pa]	-1.2869	-1.3170	-0.9724	-1.6871	-1.8302	2.3982

With the present analysis, a validation of the model about the implementation of the VAT material is done. As explained in Chapter 4 the main difference with respect to the traditional material is about the x,y dependence of the material constitutive properties due to the rotation matrix. It is clear from the reported results that the introduction of the VAT mathematical complication is solved with good results.

6.2 VAT thermo-mechanical decoupled analysis

Following, the model analyzed in Section 5.2.1 where geometry, material, and BCs are described, is considered and analyzed again but the modelization of the stacking sequences is obtained using a VAT approach.

In the already reported analysis, the model was described by the traditional straight fiber path with the staking sequence $[0/90]_s$ where the orientation angle of the fiber is constant in the single layer and the material properties can be considered as constant in the plane. With the following new analysis, a validation of the VAT numerical approach for a thermo-static analysis is done because the same straight fiber path is described using the mathematical model represented in the equation 4.7. Where, also if the model presents a straight fiber configuration the mathematical model considers the material properties as variables along the layer plane, important for the validation is the mathematical implementation of the material.

To verify the VAT integration approach that is necessarily different from the traditional one, the lamination is represented by a VAT material with lamination $[0 < 0, 0 >, 0 < 90, 90 >]_s$. Furthermore, a validation of the VAT results is obtained by comparing them with the traditional approach

results obtained in Section 5.2.

A decoupled approach is chosen because of the external load applied. A constant over-temperature along the whole thickness is chosen due to its more interest in buckling problems. Moreover, as evidenced in Table 5.6 about the same results are reached with the decoupled approach and the coupled one but a lower computational cost is spent with the decoupled analysis.

Following some results are reported comparing the one obtained with the present VAT analysis, the decoupled 30 x 30 Q9 4LE3, coupled 30 x 30 Q9 4LE3, and the ABAQUS decoupled one. Considering the external load and the way to deflect, the stress results are taken in the central point of the plate and represented along the z axis. These results are compared with the one reported in Subsection 5.2.1. The mesh discretization of the present analysis with VAT material modelization is a 30 x 30 Q9 4LE3.

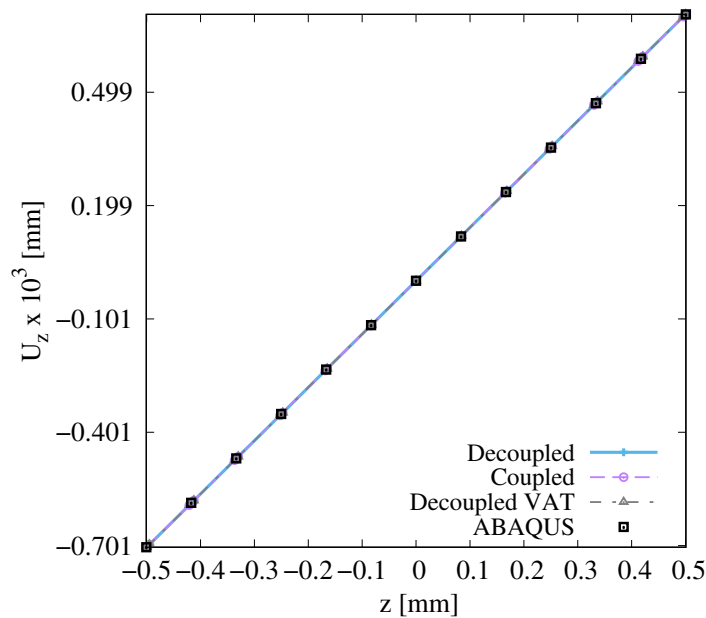


Figure 6.5: Displacement along the thickness. Comparison between different approaches. Discretization for the present method 30 x 30 Q9 4LE3. Carbon/Epoxy [0/90/90/0].

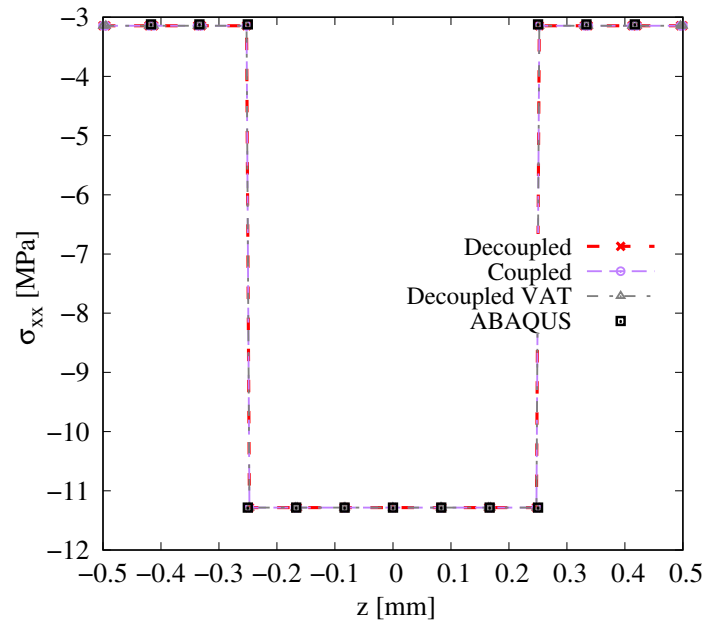


Figure 6.6: σ_{xx} along the thickness. Comparison between different approaches. Discretization for the present method 30×30 Q9 4LE3. Carbon/Epoxy [0/90/90/0].

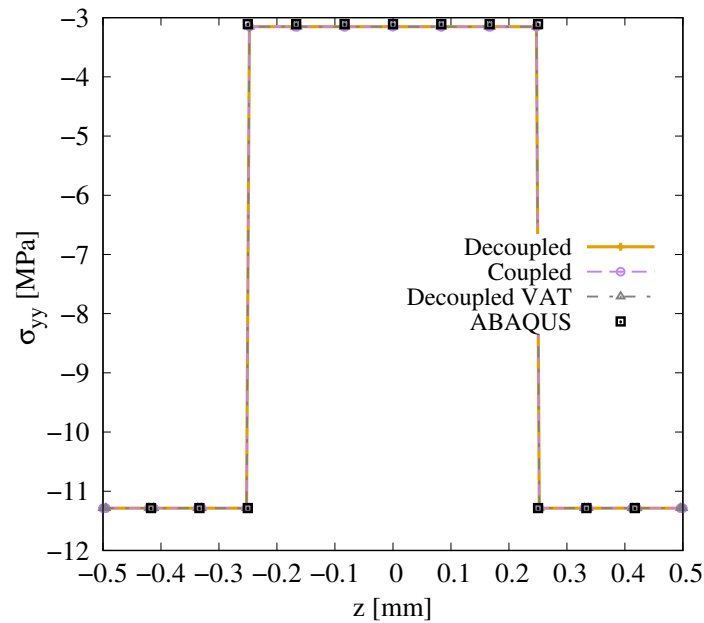


Figure 6.7: σ_{yy} along the thickness. Comparison between different approaches. Discretization for the present method 30×30 Q9 4LE3. Carbon/Epoxy [0/90/90/0].

The results reported in Figs 6.5, 6.6 and 6.7 represent the in-plane stress trend and displacement. Shear stresses are not reported because of their little value. As clear from the trends, the results are perfectly overlapped, and the different models and approaches permit the description of the same geometry and load case. The reported analyses are useful to validate the VAT numerical approach

which is more complex than the traditional one. After the validation of the numerical method in a static decoupled analysis the thermal buckling analysis is done. As described, the buckling analysis is based on an eigenvalue problem and the first eigenvalue represents the critical buckling temperature.

6.3 Thermal buckling

In the present section, a thermal buckling analysis is carried out. As explained in Subsection 3.1.3 the non-linear operator is introduced and linearizing the non-linear equation that describes the phenomenon eigenvalue problem is solved. From this consideration, and using an external thermal load of 1 degree, the first eigenvalue represents directly the buckling thermal critical load.

For the validation analysis a lamination of $[45/45]_s$ is used, the configuration corresponds to the best straight fiber path to retard buckling deflection. Therefore, the results are useful not only for the method validation but also for the following work to compare the VAT-optimized critical load with the better critical temperature obtained in a traditional fiber deposition configuration. Furthermore, it is possible to evaluate the incrementation in the critical temperature changing the deposition and the convenience of the VAT composite application.

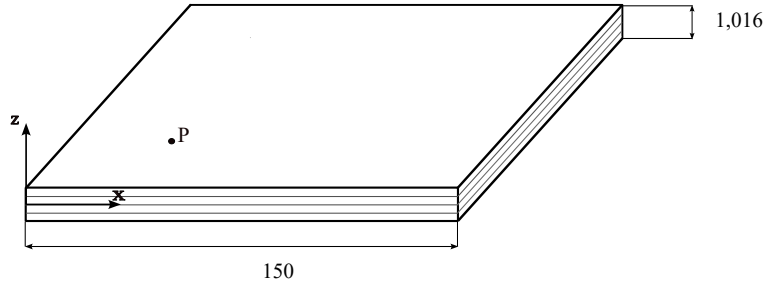
More important for the validation is the mathematical implementation of the material. To verify the VAT integration approach also for the thermal components, the lamination is represented by a VAT material with lamination $[0 < 45, 45 >, 0 < 45, 45 >]_s$. The analysis is useful to compare the results and validate the VAT approach with the traditional one that was validated in the previous chapters.

A decoupled approach is chosen because of the external load applied. A constant over-temperature along the whole thickness is chosen and as evidenced in Table 5.6 about the same results are reached with the decoupled approach if compared with the coupled one with a lower computational cost.

The following analyses consider a four-layer square plate with an edge of 150 mm and a thickness of 1.016 mm. The dimensions of the plate are reported in Figure 6.8. A 1-degree external over-temperature is applied. The first plate has a Carbon/Epoxy composite material and the layers of the second are composed of E-Glass/Epoxy whose properties reported in Table 6.3 are considered. The optimization will be done for both materials instead the convergence study is done only for the first material because geometry and BCs remain the same.

The analysis is carried out using Q9 plate elements and for the convergence analysis, the LE along the thickness is used. After the in-plane convergence study, also the in-thickness expansion theory is changed by comparing the results of the Lagrange and Taylor expansions. The plate is simply supported along the middle line of the edges but some clamped results are reported only for comparison.

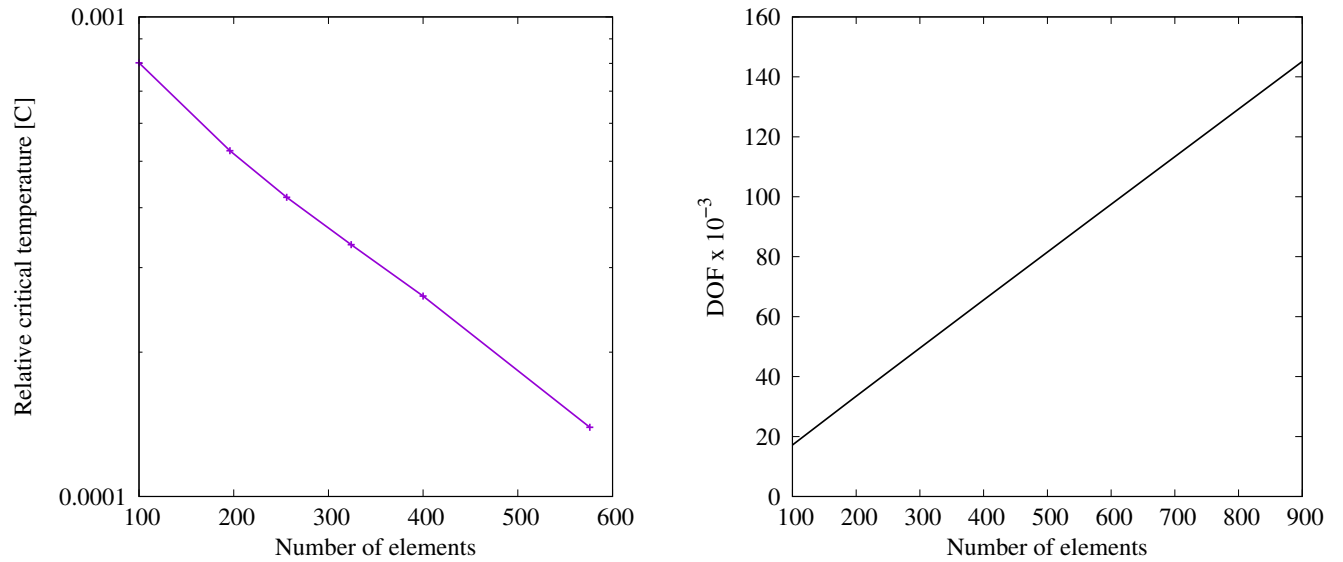
Geometry, material, and BCs are taken from [12] where the critical buckling temperature and the optimum configuration are calculated. In the reference, a CLT model with 20×20 Q4 elements along the plate is used to analyze the present configuration. The [12] results are about the buckling critical load and for the present case it is equal to 42.21 deg. In the following work, different discretizations and high-order theories are used to describe the model, and better modelization is chosen. The model will be compared with the literature and lower critical temperature is expected from the present analysis. Indeed, a more accurate model that uses for example LW approach for the material modelization, Lagrange expansion along the thickness and plate element with nine nodes instead of the four, can provide a lower critical temperature as a result of the eigenvalue problem. Geometry and material properties are reported respectively in Figure 6.8 and Table 6.3, and the results are calculated in the point $P = (37.5, 37.5)[\text{mm}]$ as represented in Figure 6.8.

**Figure 6.8:** Plate [mm].**Table 6.3:** Materials properties used in the analysis.

	E_1 [GPa]	E_2 [GPa]	ν_{12}	G_{12} [GPa]	α_{11} [1/C x 10^{-6}]	α_{22} [1/C x 10^{-6}]
Carbon/Epoxy	147	10.3	0.27	7.0	-0.9	27.0
E-Glass/Epoxy	41	10.04	0.28	4.3	7.0	26.0

As done in the previous chapters a convergence analysis is necessary to obtain realistic results. The convergence study is done considering the in-plane mesh and some considerations of the in-thickness expansion function are carried out. Taylor expansion results are investigated but, the LE is not varied because as established in Subsection 5.1.1 a better representation of the thermal shear stresses is possible at least with a three-order in thickness expansion.

Table 6.4 and Figure 6.9 describe the obtained results and the optimum is chosen considering both, the computational cost and the accuracy of the results. Figure 6.9 (a) is semi-logarithmic and represents the relative error of the critical temperature with respect to the more accurate one that is the 30 x 30, varying the in-plane discretization ($\frac{T_i - T_{30}}{T_{30}}$ where i is the discretization). Furthermore, the number of the DOFs of the problem analyzed with the present method is reported. For the sake of clarity, numerical values are represented in Table 6.4. In the second part of Table 6.4, reference results are reported. The reference model is analyzed with a CLT approach and a comparison with the Taylor expansion models is done.



(a) Convergence rate considering $Q9$ plate elements. y logarithmic axes.

(b) Number of DOF related with the increase in elements number.

Figure 6.9: Convergence study for the thermal buckling analysis.

Table 6.4: Convergence study considering $Q9$ elements for the present work and $LE3$ expansion along the thickness. CLT and $Q4$ elements are used in reference.

Number of elements	Critical temperature [$^{\circ}C$]	DOFs
100	42.286	17199
196	41.765	32799
256	41.589	42471
324	41.445	53391
400	41.322	65559
576	41.120	93636
900	40.885	145119
References [12]		
400 [Q4]	42.213	-

In Figure 6.10 the z displacement of the present analysis is reported, displacement in the x and y direction are not represented because are neglectable to the others and there are both so low to be subjected to numerical problems. The analysis is done also in ABAQUS and displacement results are reported in the same figure.

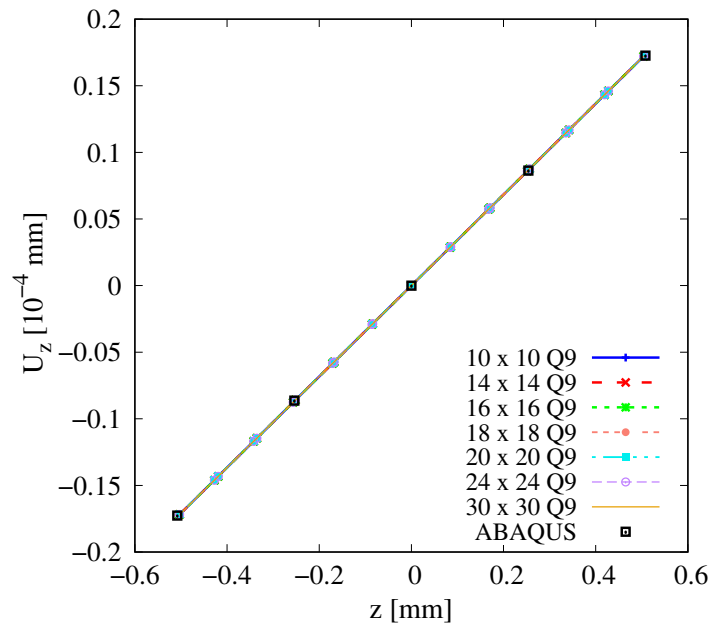


Figure 6.10: Displacement along z -direction. Convergence study varying the in-plane discretization, 4 LE3 thickness expansion, results have been taken in point P .

It is clear from the displacement results that a good displacement is reached also with a 10×10 Q9 discretization. It is also clear that the displacement is typical, the first value reaching the convergence for this type of applied load and deflection. Therefore, the buckling critical temperature is considered the principal variable to determine the best mesh discretization for the following analysis. Thanks to the analyses reported in Table 6.4 it is possible to decide the better discretization with a trade-off between the accuracy and the computational cost. With a 20×20 Q9 mesh, good results are reached and the computational cost remains limited, indeed increasing the number of elements the slope of the curve representing the error of the calculated temperature changes and becomes less steep. The new trend indicates that fewer changes are present as a result with respect to the following one. Considering the computational cost, the same accuracy considerations are followed because it rapidly increases after a 20×20 Q9 mesh.

As said before, a change in the in-thickness expansion is now reported. Table 6.5 reports the critical temperature obtained with the present analysis considering an in-plane mesh of 20×20 Q9 elements. The reference temperature is reported in the same table. The results from the variation along the thickness expansion are reported in the following bar diagram where buckling critical temperature is represented considering the difference HOT used.

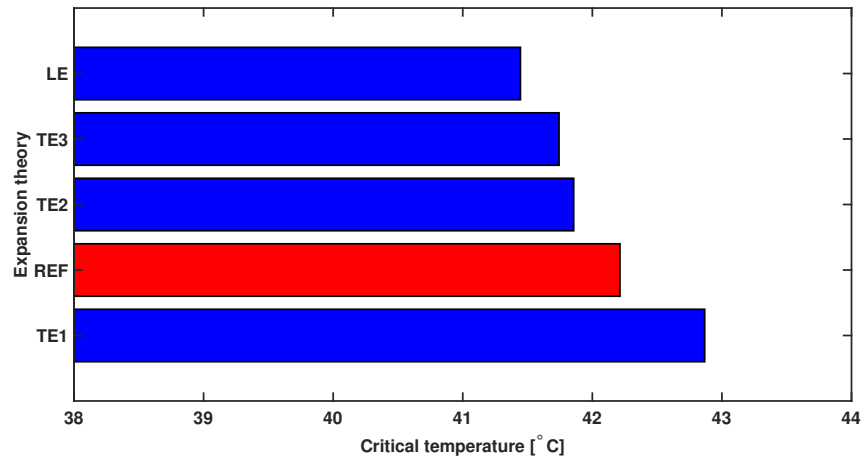


Figure 6.11: Representation of the buckling critical temperature obtained by in-thickness theory variations.

Table 6.5: Thermal-buckling critical temperature for changes in the in-thickness expansion theory, 20×20 Q9 plate discretization.

Expansion theory	TE1	TE2	TE3	LE	References [12]
DOFs	10087	15129	20172	65559	
Critical temperature [°C]	42.867	41.856	41.743	41.322	42.213

As expected the reference result provides a buckling critical temperature between the first two Taylor models. Considering the critical temperature, the Lagrange expansion along the thickness supplies the best result with a better description of the phenomenon. The Lagrange increases in the number of DOFs is not too high and for comparing reasons, both LE and TE2 are used to analyze Carbon/Epoxy laminate. However, in the E-Glass case, only the LE model is used. In Table 6.6, some results are reported changing the constraints of the plate. Geometry and material remain the same as in the previous case. A comparison between clamped and simply supported results is reported.

The results collected in Table 6.6 make evident the importance of the boundary conditions in the buckling analysis, in fact, with a clamped plate the buckling critical temperature abruptly increases and doubles to the ones calculated in the simply supported case.

Table 6.6: Thermal-buckling critical temperature for in-thickness expansion theory changes, 20×20 Q9 plate discretization.

	TE1	TE2	TE3	LE
Simply supported	42.867	41.856	41.743	41.445
Clamped	88.450	86.365	86.265	86.243

The analyses reported in this section are very important to validate the present method for the VAT thermal buckling problem, the used method permits to obtain of accurate results concerning

the buckling problem and represents the starting point for working on the angle path optimization.

6.4 Thermal buckling angle optimization

As said before, in this section two different materials are considered and angle optimization of the fiber path is done. For the sake of clarity, the equation describing the angle orientation along the x - y plane is following reported.

$$\theta(x') = \Phi + T_0 + \frac{T_1 - T_0}{d} |x'| \quad (6.1)$$

where the full explanation of the formula is done in Chapter 4.

For simplicity in the optimization only two of the three variables describing the problem are varied. The angle Φ remains zero for all the analyses. The two angles T_0 and T_1 are varied from -90 to 90 degrees and the lamination along the thickness is $[\theta / -\theta / -\theta / \theta]$ for each analysis.

All the analyses are done considering an in-plane mesh of 20×20 Q9 and a thickness expansion of 4LE3 as determined in the convergence analysis. The model is described before and the material properties are the ones in Table 6.3. The stress results are taken in point P reported in Figure 6.8.

6.4.1 Carbon/Epoxy angle optimization

The following graphs represent the buckling critical temperature varying the two variables of the fiber path. The data used for the interpolation are reported in Appendix B. Following the same analysis is done with two different expansion theories. In the first graph, reported in Figure 6.12 TE2 is used with an ESL approach for the material representation. Following, in Figure 6.13, the reference results are reported taken from Duran et al. [12]. In Figure 6.14 the same plate is analyzed considering an LE thickness expansion. As expected, the LE results are more accurate than the Taylor ones but present a higher computational cost.

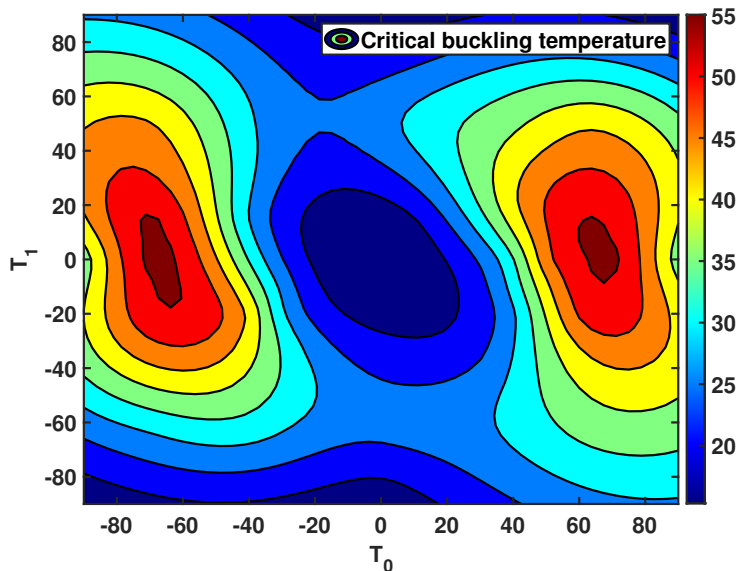


Figure 6.12: Carbon/Epoxy critical buckling temperature varying the path angles. Present method with ESL and TE2 in-thickness expansion.

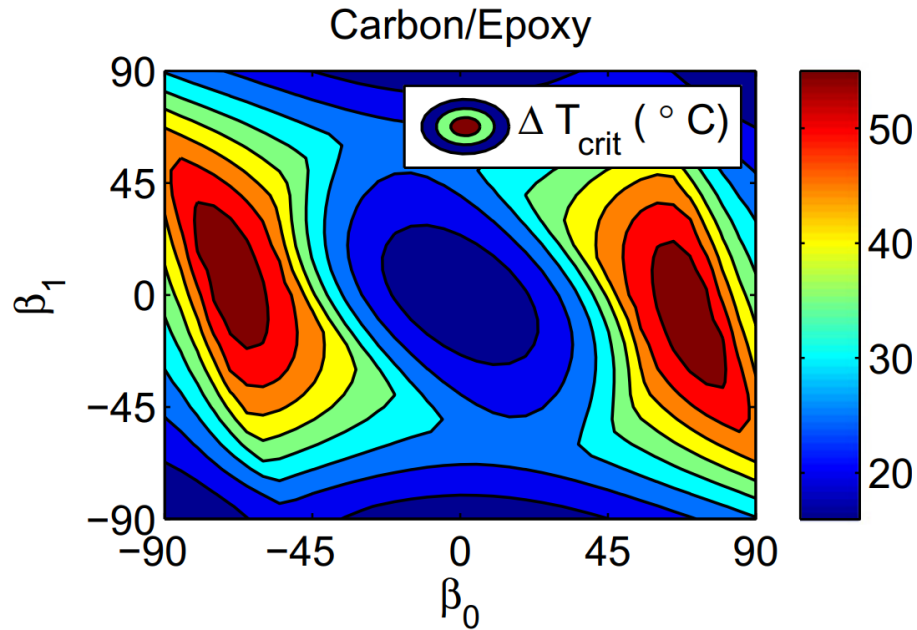


Figure 6.13: Carbon/Epoxy critical buckling temperature varying the path angles. Reference taken from Duran et al. [12]

The reported results in Fig. 6.12 and Fig.6.13 are comparable with few differences. The maximum value of the critical temperature is about the same as reported in Table 6.7.

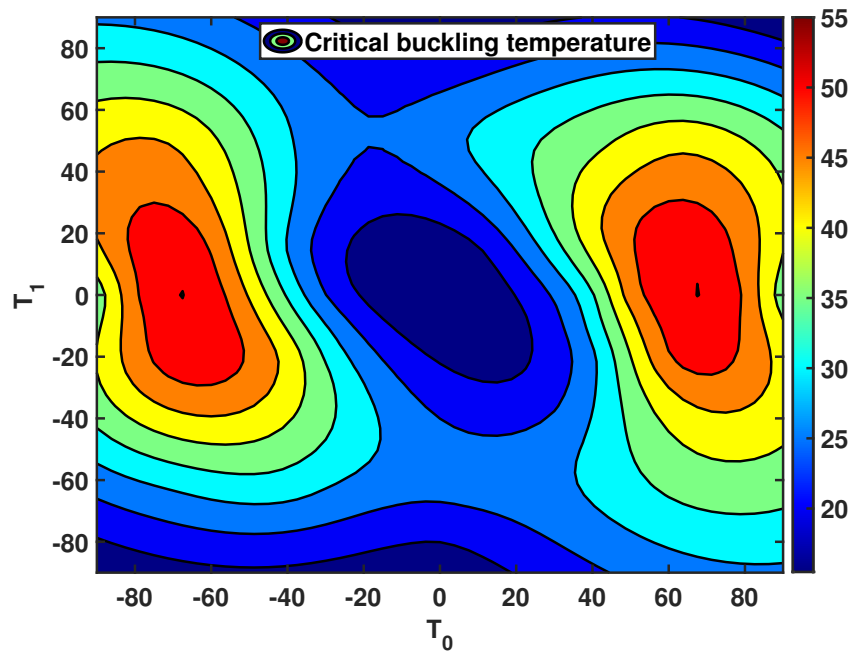


Figure 6.14: Carbon/Epoxy critical buckling temperature varying the path angles. LE3 thickness expansion.

The thermal buckling critical temperature graphs, as expected are symmetric with respect to the line $T_0 = -T_1$ and present two maximum value zones. In the most accurate case, the critical temperature goes from about 15 *degrees* to 55 *degrees*. The difference between maximum and minimum critical temperature is very high and is evaluated following.

In Table 6.7 the maximum critical temperatures calculated with the present method are reported and compared with the reference one, and the better curvilinear path with relative angles is described. The results are also calculated for the better straight path of [45/ - 45/ - 45/45], and the worst curvilinear path and are reported respectively in Table 6.7 and 6.8. A comparison between the results of the reference and the present analysis of critical temperature is done.

Table 6.7: *Maximum critical buckling temperatures for VAT and straight configuration. Present work with surface mesh 20 x 20 Q9, thickness expansion 4LE3. Carbon/Epoxy.*

Analysis	T_0	T_1	ΔT_{cr}	$\Delta T_{straight}$
20 x 20 Q9 4LE3	-68.290	0.452	55.107	41.322
20 x 20 Q9 TE2	-67.387	0.452	56.2697	41.856
Ref. [12]	69.00	-5.705	57.790	42.213

Table 6.8: *Minimum critical buckling temperature and orientations. Present work with surface mesh 20 x 20 Q9, thickness expansion 4LE3. Carbon/Epoxy.*

	T_0	T_1	ΔT_{min}
20 x 20 Q9 4LE3	-3.166	4.070	15.470
20 x 20 Q9 TE2	-3.166	1.357	15.296

From the comparison between the different method, it is clear that, changing the in-thickness expansion the critical temperature change little. The most important change is in the extension of the zones where the critical temperature is maxima. Comparing the results calculated with the present method, the TE2 is more similar to the reference but the LE model is more accurate. The zones with maximum temperature are abruptly reduced in the LE model than in the less accurate models. Therefore, the increase in accuracy of the model using LE is not constant all over the path but changes depending on the critical temperature. As a consequence, it is interesting to consider the percentage relative increase in accuracy reached with the Lagrange model which is reported in Fig. 6.15.

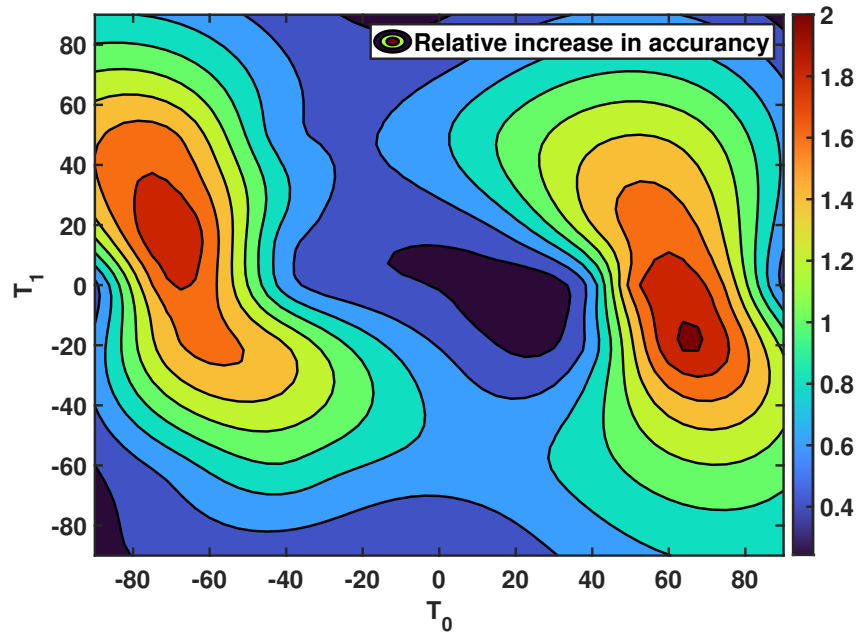


Figure 6.15: Percentage relative increasing accuracy from LE to TE2.

The graph reported in Fig. 6.15 represents the increase in accuracy reached with the LE model with respect to the TE2 ($\frac{\theta_{TE} - \theta_{LE}}{\theta_{TE}}$). It is clear that the relative variation is not constant for each path configuration but follows the same trend of the results increases in the zones with maximum temperature.

From the results reported in Table 6.7 and Figs 6.14 and 6.12 it is clear that the influence of the angle orientation has a high incidence on the thermal buckling critical temperature for the Carbon/Epoxy composite material. The better VAT configuration calculated with the present method has a similar orientation compared with the references [12]. Furthermore, the present work is more accurate, considering the element discretization and the method used for the analysis, and, as expected, a lower critical temperature is obtained.

Following the stresses trends for the better and worst curvilinear fiber distribution from the LE configuration are reported for comparison. Some stresses are comparable and are represented in the same graph instead, other stresses with different entities are reported next to each other.

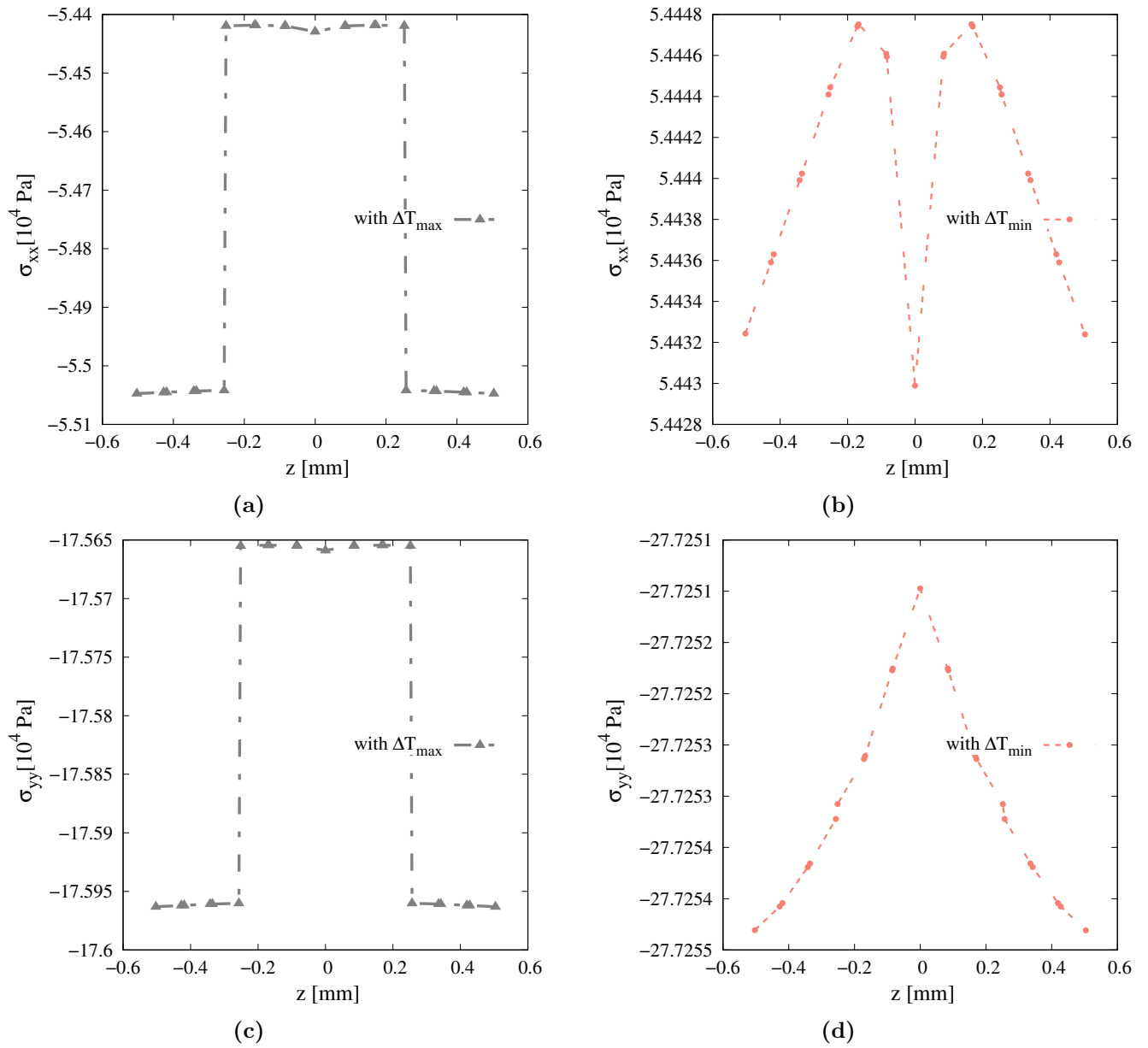


Figure 6.16: Carbon/Epoxy. Thickness expansion: one LE3 for each layer, 20 x 20 Q9 elements. Comparison of stresses in the better and worst buckling case. (a)(b) σ_{xx} , (c)(d) σ_{yy} .

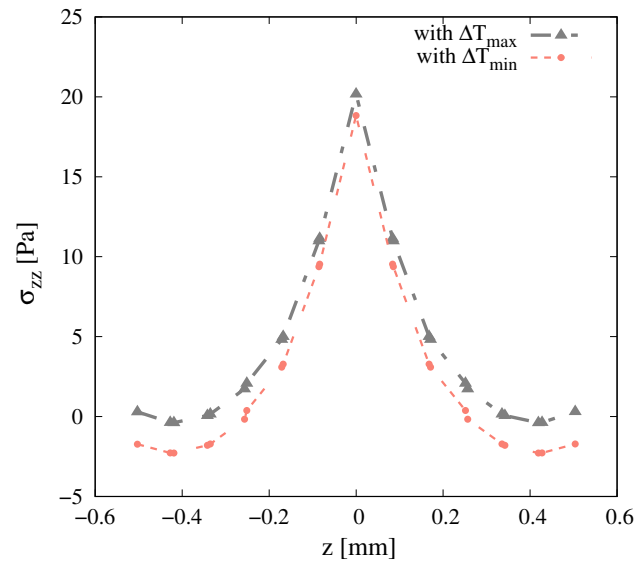


Figure 6.17: *Carbon/Epoxy. Thickness expansion: one LE3 for each layer, 20 x 20 Q9 elements. Comparison of stresses in the better and worst buckling case, σ_{zz} .*

The stress representation is useful to determine their influence on the buckling critical load. Firstly, it is clear that the in-plane stresses in the minimum temperature configuration are not compressive stress but the plate is subject to traction. The in-plane y-direction stress is negative and represents a compression configuration for the model. The very high difference between the x and y stresses, particularly for the type of stress state favors the buckling of the plate. Shear stresses are not so high and are similar for the two configurations, it is so clear that no high influence is given from the shear stresses.

6.4.2 E-Glass/Epoxy optimization

The graph in Figure 6.18 represent the buckling critical temperature varying the two variable of the fiber path. The graph can be compared with the literature [12] reported in the graph in Fig. 6.19 and about the same trend is reached. One main difference is present between the reference and the present work. In fact, as reported in Section 6.3, the present work is more accurate and the critical temperatures are lower than the published ones [12].

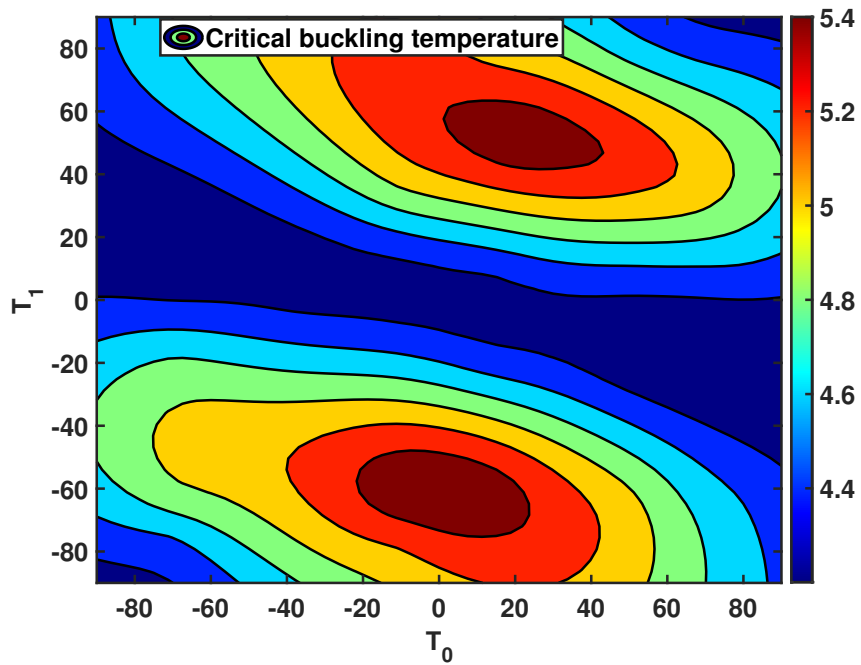


Figure 6.18: E-Glass/Epoxy critical buckling temperature varying the path angles.

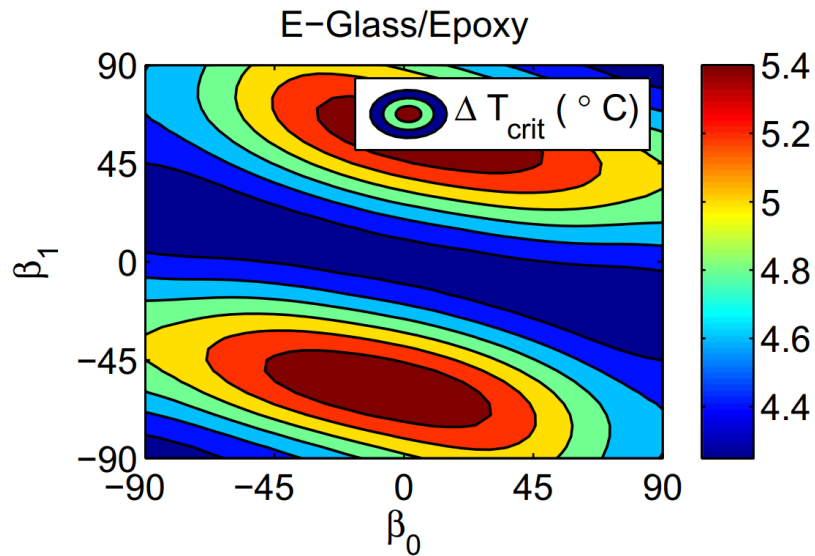


Figure 6.19: E-Glass/Epoxy critical buckling temperature varying the path angles. Reference taken from Duran et al. [12]

From the Figs 6.18 and 6.19 it is clear that the LE model is more accurate and low critical temperatures are reached. Considering Fig. 6.15 the differences in critical temperature are more reached for high value of the ΔT_{cr} and due to the little values of the present case critical temperature, no comparison is done in this case. In Tables 6.9 and 6.10, the critical temperatures calculated with

the present method are reported and compared with the references ones. In Table 6.9 the results of the better straight path of $[45/-45/-45/45]$ and the better curvilinear path are compared and also the reference results are reported. In Table 6.10 the worst critical temperature for the VAT configuration and the relative curvilinear path is reported.

Table 6.9: Maximum critical buckling temperatures for VAT and straight configuration. Present work with surface mesh 20×20 Q9, thickness expansion $4LE3$. E-Glass/Epoxy.

Analysis	T_0	T_1	ΔT_{cr}	$\Delta T_{straight}$
20 x 20 Q9 4LE3	-4.975	-60.15	5.55	5.384
Ref. [12]	6.710	58.04	5.580	5.428

Table 6.10: Minimum critical buckling temperature and orientations. Present work with surface mesh 20×20 Q9, thickness expansion $4LE3$. E-Glass/Epoxy.

	T_0	T_1	ΔT_{min}
20 x 20 Q9 4LE3	80.050	-20.351	4.20

The contour map reported in Figure 6.18 presents a symmetric behavior as the one representing the Carbon/Epoxy laminated but the excursion between the maximum and minimum value is not so high. Probably the presence of a negative expansion coefficient of the Carbon/Epoxy material influences the thermal buckling variation along the path and makes it bigger.

Following the stresses trends for the better and worst curvilinear fiber distribution are reported for comparison purposes. Some stresses are comparable and are represented in the same graph instead some stresses with different entities are reported next to each other.

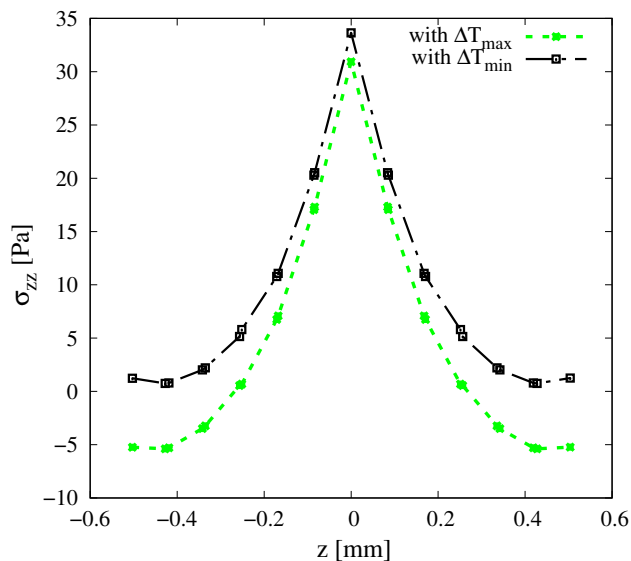


Figure 6.20: E-Glass/Epoxy. Thickness expansion: one $LE3$ for each layer, 20×20 Q9 elements. Comparison of stresses in the better and worst buckling case, σ_{zz} .

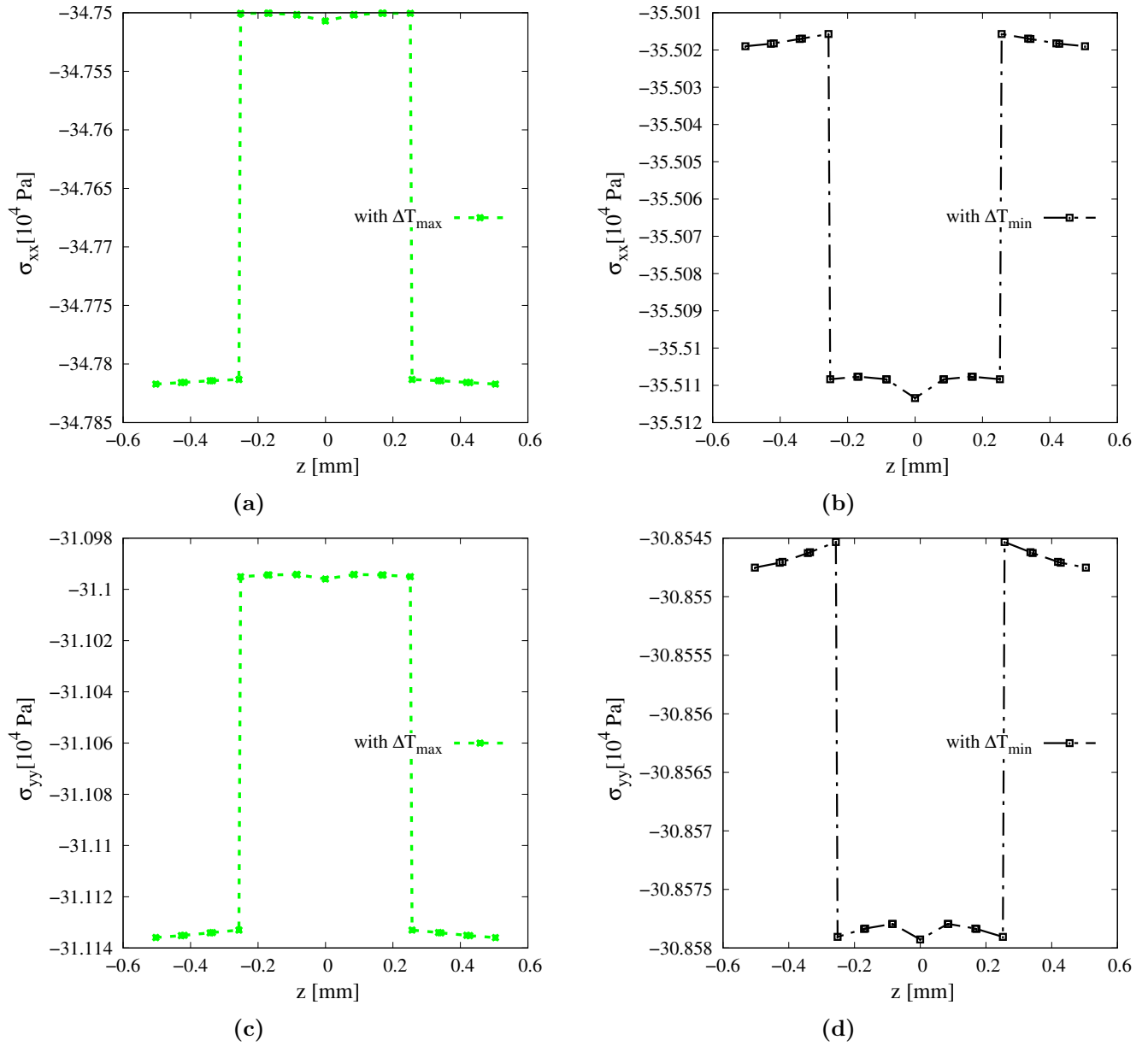


Figure 6.21: *E-Glass/Epoxy*. Thickness expansion: one LE3 for each layer, 20 x 20 Q9 elements. Comparison of stresses in the better and worst buckling case. (a)(b) σ_{xx} , (c)(d) σ_{yy} .

Also, the difference between the x and y stresses is high in the minimum critical temperature case but the difference is not so high and the same type of stress configuration is present in both analyses. The external layers are more loaded than the internal ones for the worst case and the stress configuration can favor the buckling phenomenon.

Chapter 7

Conclusions

The present thesis work has investigated the thermal buckling critical load for VAT panels using the 2D-CUF framework. Thermo-mechanical problem is examined for different materials, and isotropic and fiber composite reinforced laminate are studied to validate the model. Convergence analyses are done and coupled and decoupled approaches are investigated to choose the better configuration for the thermo-buckling analysis. The Carrera Unified Formulation plate theory is implemented considering QUAD9 elements and Lagrange expansion functions. Therefore, the Layer Wise model is used to describe the laminate as well as guarantee the C_z^0 requirements.

Thermo-static analyses are done and displacement and stresses are reported in the different plate configurations and for various materials to evaluate their trends. Different boundary conditions were investigated in the thermo-static analyses. Therefore, for the buckling analysis constant over-temperature and simply supported constraints are chosen. Moreover, the discretization was selected, and Q9 elements with 1LE3 in each layer are chosen for the last analyses.

Decoupled buckling analyses are carried by solving the eigenvalue problem which makes the non linear problem much more simple to solve, by finding the critical buckling temperature as the bifurcation point (first eigenvalue). Finally, two square plates with VAT layers are analyzed and compared with the literature where the same models are analyzed with commercial software. The first plate was composed of Carbon/Epoxy with α_{11} negative expansion coefficient and the second was of E-Glass/Epoxy.

The VAT path was investigated by changing the deposition angles to show the various critical temperature, and the best configuration for retarding the phenomenon is selected. A comparison between the pre-buckling stresses for the higher and lower critical buckling temperature configurations is done for both materials. The difference between the critical temperatures for better straight fiber configuration and VAT deposition are analyzed.

From the analyses some consideration can be reported:

- For the Carbon/Epoxy laminate, the better deposition angles are $T_0 = -68.29$, $T_1 = 0.45$ that allows reaching a critical over-temperature of 55.1 *degrees* with a consistent gain to the straight deposition critical temperature of 41.3 *degrees*.
- E-Glass/Epoxy configuration does not present great advantages using VAT deposition with a gain using VAT materials of 0.03% passing from a critical temperature of 5.384 to a VAT optimal critical temperature of 5.55 *degrees*.
- Comparing the results obtained from the present work and the published one it is clear that

the present method permits describing more accurately the thermal buckling critical load with a lower computational cost.

7.1 Future Trends

The thermal buckling research of VATs is still in its early stages, and the following case study have further analyses and materials that may be examined.

For future analyses, it could be interesting to investigate different materials, stacking sequence, thickness and boundary conditions. As clear from the reported results, different materials can have various behavior and no rules can be extracted from the present work. More materials with different expansion coefficients, mechanical properties, and orthotropic ratios can be considered to evaluate the influence of these parameters.

Interasting work can be done for:

- Post-buckling behavior and post-buckling stresses condition. Indeed, the 'bending' due to the buckling deflection implies not negligible shear stresses are presents.
- Non-symmetric laminate that present coupling elements.
- Optimization of the VATs orientation to maximize the post-buckling strength.
- Application to 3D printing materials.

Appendix A

The CUF mechanical fundamental nuclei are following reported.

$$\begin{aligned}
 K_{xx}^{\tau sij} &= C_{11} \int_{\Omega} N_{i,x} N_{j,x} d\Omega \int_h F_{\tau} F_s dz + C_{16} \int_{\Omega} N_{i,x} N_{j,y} d\Omega \int_h F_{\tau} F_s dz + \\
 &+ C_{16} \int_{\Omega} N_{i,y} N_{j,x} d\Omega \int_h F_{\tau} F_s dz + C_{44} \int_{\Omega} N_i N_j d\Omega \int_h F_{\tau,z} F_{s,z} dz + C_{66} \int_{\Omega} N_{i,y} N_{j,y} d\Omega \int_h F_{\tau} F_s dz
 \end{aligned} \tag{A.1}$$

$$\begin{aligned}
 K_{xy}^{\tau sij} &= C_{12} \int_{\Omega} N_{i,y} N_{j,x} d\Omega \int_h F_{\tau} F_s dz + C_{62} \int_{\Omega} N_{i,y} N_{j,y} d\Omega \int_h F_{\tau} F_s dz + \\
 &+ C_{16} \int_{\Omega} N_{i,x} N_{j,x} d\Omega \int_h F_{\tau} F_s dz + C_{45} \int_{\Omega} N_i N_j d\Omega \int_h F_{\tau,z} F_{s,z} dz + C_{66} \int_{\Omega} N_{i,x} N_{j,y} d\Omega \int_h F_{\tau} F_s dz
 \end{aligned} \tag{A.2}$$

$$\begin{aligned}
 K_{xz}^{\tau sij} &= C_{13} \int_{\Omega} N_i N_{j,x} d\Omega \int_h F_{\tau,z} F_s dz + C_{63} \int_{\Omega} N_i N_{j,y} d\Omega \int_h F_{\tau,z} F_s dz + \\
 &+ C_{44} \int_{\Omega} N_{i,x} N_j d\Omega \int_h F_{\tau} F_{s,z} dz + C_{45} \int_{\Omega} N_{i,y} N_j d\Omega \int_h F_{\tau} F_{s,z} dz
 \end{aligned} \tag{A.3}$$

$$\begin{aligned}
 K_{yx}^{\tau sij} &= C_{21} \int_{\Omega} N_{i,x} N_{j,y} d\Omega \int_h F_{\tau} F_s dz + C_{61} \int_{\Omega} N_{i,x} N_{j,x} d\Omega \int_h F_{\tau} F_s dz + \\
 &+ C_{26} \int_{\Omega} N_{i,y} N_{j,y} d\Omega \int_h F_{\tau} F_s dz + C_{45} \int_{\Omega} N_i N_j d\Omega \int_h F_{\tau,z} F_{s,z} dz + C_{66} \int_{\Omega} N_{i,y} N_{j,x} d\Omega \int_h F_{\tau} F_s dz
 \end{aligned} \tag{A.4}$$

$$\begin{aligned}
 K_{yy}^{\tau sij} &= C_{22} \int_{\Omega} N_{i,y} N_{j,y} d\Omega \int_h F_{\tau} F_s dz + C_{62} \int_{\Omega} N_{i,y} N_{j,x} d\Omega \int_h F_{\tau} F_s dz + \\
 &+ C_{26} \int_{\Omega} N_{i,x} N_{j,y} d\Omega \int_h F_{\tau} F_s dz + C_{55} \int_{\Omega} N_i N_j d\Omega \int_h F_{\tau,z} F_{s,z} dz + C_{66} \int_{\Omega} N_{i,x} N_{j,x} d\Omega \int_h F_{\tau} F_s dz
 \end{aligned} \tag{A.5}$$

$$\begin{aligned}
K_{yz}^{\tau sij} &= C_{23} \int_{\Omega} N_i N_{j,y} d\Omega \int_h F_{\tau,z} F_s dz + C_{63} \int_{\Omega} N_i N_{j,x} d\Omega \int_h F_{\tau,z} F_s dz + \\
&+ C_{55} \int_{\Omega} N_{i,y} N_j d\Omega \int_h F_{\tau} F_{s,z} dz + C_{45} \int_{\Omega} N_{i,x} N_j d\Omega \int_h F_{\tau} F_{s,z} dz \quad (A.6)
\end{aligned}$$

$$\begin{aligned}
K_{zx}^{\tau sij} &= C_{31} \int_{\Omega} N_{i,x} N_j d\Omega \int_h F_{\tau} F_{s,z} dz + C_{44} \int_{\Omega} N_i N_{j,x} d\Omega \int_h F_{\tau,z} F_s dz + \\
&+ C_{45} \int_{\Omega} N_i N_{j,y} d\Omega \int_h F_{\tau,z} F_s dz + C_{36} \int_{\Omega} N_{i,y} N_j d\Omega \int_h F_{\tau} F_{s,z} dz \quad (A.7)
\end{aligned}$$

$$\begin{aligned}
K_{zy}^{\tau sij} &= C_{32} \int_{\Omega} N_{i,y} N_j d\Omega \int_h F_{\tau} F_{s,z} dz + C_{55} \int_{\Omega} N_i N_{j,y} d\Omega \int_h F_{\tau,z} F_s dz + \\
&+ C_{45} \int_{\Omega} N_i N_{j,x} d\Omega \int_h F_{\tau,z} F_s dz + C_{36} \int_{\Omega} N_{i,x} N_j d\Omega \int_h F_{\tau} F_{s,z} dz \quad (A.8)
\end{aligned}$$

$$\begin{aligned}
K_{zz}^{\tau sij} &= C_{33} \int_{\Omega} N_i N_j d\Omega \int_h F_{\tau,z} F_{s,z} dz + C_{44} \int_{\Omega} N_{i,x} N_{j,x} d\Omega \int_h F_{\tau} F_s dz + \\
+ C_{45} \int_{\Omega} N_{i,x} N_{j,y} d\Omega \int_h F_{\tau} F_s dz + C_{45} \int_{\Omega} N_{i,y} N_{j,x} d\Omega \int_h F_{\tau} F_s dz + C_{55} \int_{\Omega} N_{i,y} N_{j,y} d\Omega \int_h F_{\tau} F_s dz \quad (A.9)
\end{aligned}$$

Following the additional thermal fundamental nuclei are reported.

$$K_{x\theta}^{\tau sij} = -\lambda_1 \int_{\Omega} N_i N_{j,x} d\Omega \int_h F_{\tau} F_s dz - \lambda_6 \int_{\Omega} N_i N_{j,y} d\Omega \int_h F_{\tau} F_s dz \quad (A.10)$$

$$K_{y\theta}^{\tau sij} = -\lambda_2 \int_{\Omega} N_i N_{j,y} d\Omega \int_h F_{\tau} F_s dz - \lambda_6 \int_{\Omega} N_i N_{j,x} d\Omega \int_h F_{\tau} F_s dz \quad (A.11)$$

$$K_{z\theta}^{\tau sij} = -\lambda_3 \int_{\Omega} N_i N_j d\Omega \int_h F_{\tau} F_{s,z} dz \quad (A.12)$$

$$K_{\theta x}^{\tau sij} = -\lambda_1 \int_{\Omega} N_{i,x} N_j d\Omega \int_h F_{\tau} F_s dz - \lambda_6 \int_{\Omega} N_{i,y} N_j d\Omega \int_h F_{\tau} F_s dz \quad (A.13)$$

$$K_{\theta y}^{\tau sij} = -\lambda_2 \int_{\Omega} N_{i,y} N_j d\Omega \int_h F_{\tau} F_s dz - \lambda_6 \int_{\Omega} N_{i,x} N_j d\Omega \int_h F_{\tau} F_s dz \quad (A.14)$$

$$K_{\theta z}^{\tau sij} = -\lambda_3 \int_{\Omega} N_i N_j d\Omega \int_h F_{\tau,z} F_s dz \quad (A.15)$$

$$K_{\theta\theta}^{\tau sij} = \chi \int_{\Omega} N_i N_j d\Omega \int_h F_{\tau} F_s dz \quad (A.16)$$

Appendix B

Table reporting the calculated buckling critical temperature are reported for both, Carbon/Epoxy and E-Glass/Epoxy.

Table B.1: *On the left: Carbon/Epoxy critical temperature. On the right: E-Glass/Epoxy critical temperature.*

Carbon/Epoxy			E-Glass/Epoxy		
T_0	T_1	ΔT_{cr}	T_0	T_1	ΔT_{cr}
45	45	4.13E+01	45	45	5.38E+00
-70	0	5.50E+01	-70	-76	4.59E+00
-70	-20	5.26E+01	-70	-62	4.93E+00
-70	-62	3.07E+01	-70	-20	4.83E+00
-70	15	5.43E+01	-70	8	4.27E+00
-70	50	4.45E+01	-70	36	4.33E+00
-40	0	3.44E+01	-70	80	4.78E+00
-40	-20	4.32E+01	-10	-76	5.26E+00
-40	-62	3.25E+01	-10	-62	5.53E+00
-40	15	2.97E+01	-10	-20	4.67E+00
-40	50	3.07E+01	-10	8	4.33E+00
-30	0	2.51E+01	-10	36	5.01E+00
-30	-20	3.44E+01	-10	80	5.29E+00
-30	-62	3.03E+01	50	-76	5.10E+00
-30	15	2.27E+01	50	-62	5.03E+00
-30	50	2.67E+01	50	-20	4.28E+00
63	0	5.41E+01	50	8	4.53E+00
63	-20	5.13E+01	50	36	5.24E+00
63	-62	3.65E+01	50	80	4.70E+00
63	15	5.42E+01	67	-76	4.83E+00
63	50	4.34E+01	67	-62	4.74E+00
10	0	1.69E+01	67	-20	4.22E+00
10	-20	1.82E+01	67	8	4.54E+00
10	-62	2.69E+01	67	36	5.13E+00
10	15	1.97E+01	67	80	4.53E+00
10	50	3.09E+01	13	-76	5.39E+00
90	90	1.60E+01	13	-62	5.51E+00
90	-90	2.91E+01	13	-20	4.51E+00
90	0	3.75E+01	13	8	4.40E+00
-90	0	3.75E+01	13	36	5.20E+00
-90	90	2.91E+01	13	80	5.11E+00
-90	-90	1.60E+01	80	-76	4.65E+00
80	0	4.91E+01	80	-62	4.58E+00
-80	0	4.91E+01	80	-20	4.20E+00
0	-80	2.00E+01	80	8	4.54E+00
0	80	2.00E+01	90	90	4.31E+00
30	-35	2.43E+01	90	-90	4.56E+00
50	0	4.72E+01	-90	-90	4.31E+00
70	0	5.50E+01	-90	90	4.56E+00
40	-20	2.91E+01	-35	8	4.28E+00
40	20	4.32E+01	20	50	5.51E+00
40	0	3.44E+01			

Table B.2: *Carbon/Epoxy TE2 point of evaluation*

T_0	T_1	ΔT_{cr}
-70	0	55.963
-70	-20	53.423
-70	-62	30.945
-70	15	55.443
-70	50	45.227
-40	0	34.606
-40	-20	43.806
-40	-62	32.845
-40	15	29.886
-40	50	30.929
-30	0	25.228
-30	-20	30.929
-30	-62	30.554
-30	15	22.813
-30	50	26.856
63	0	55.142
63	-20	52.403
63	-62	36.954
63	15	55.173
63	50	44.039
10	0	16.943
10	-20	18.266
10	-62	27.135
10	15	19.831
10	50	31.236
90	90	16.081
-90	-90	16.081
-90	90	29.350
90	-90	29.350
90	0	37.730
-90	0	37.730
30	-35	24.473
50	0	48.039
70	0	55.963
40	-20	29.309
40	20	43.806
40	0	34.606
0	80	20.126
0	-80	20.126

Bibliography

- [1] Zhongchang Qian, Daoqing Chang, Bilong Liu, and Ke Liu. Prediction of sound transmission loss for finite sandwich panels based on a test procedure on beam elements. *Journal of Vibration and Acoustics*, 135:061005, 12 2013.
- [2] Wenzhi Wang, Xiaopeng Wan, Jun Zhou, Meiyong Zhao, Yulong Li, Shen Shang, and Xiaosheng Gao. Damage and failure of laminated carbon-fiber-reinforced composite under low-velocity impact. *Journal of Aerospace Engineering*, 27:308–317, 03 2014.
- [3] Erasmo Carrera, M. Cinefra, and Fiorenzo Fazzolari. Some results on thermal stress of layered plates and shells by using unified formulation. *Journal of Thermal Stresses*, 36:589–625, 06 2013.
- [4] Luciano Demasi, Biagini Giacomo, Vannucci Federico, Enrico Santarpia, and Rauno Cavallaro. Equivalent single layer, zig-zag, and layer wise theories for variable angle tow composites based on the generalized unified formulation. 01 2017.
- [5] Prof. Erasmo Carrera Prof. Maria Cinefra Stefano Valvano. Development of computational efficient shell formulation for analysis of multilayered structures subjected to mechanical, thermal, and electrical loadings.
- [6] Alberto Racionero Sánchez-Majano, Rodolfo Azzara, Alfonso Pagani, and Erasmo Carrera. Accurate stress analysis of variable angle tow shells by high-order equivalent-single-layer and layer-wise finite element models. *Materials*, 14(21), 2021.
- [7] S Nagendra, Srinivas Kodiyalam, Jonathan Davis, and V Parthasarathy. *Optimization of tow fiber paths for composite design, 36th Structures, Structural Dynamics and Materials Conference*.
- [8] Zhangming Wu, Gangadharan Raju, and Paul Weaver. Postbuckling analysis of variable angle tow composite plates. *International Journal of Solids and Structures*, 50:1770–1780, 05 2013.
- [9] Alfonso Pagani, Rodolfo Azzara, and Erasmo Carrera. Geometrically nonlinear analysis and vibration of in-plane-loaded variable angle tow composite plates and shells. *Acta Mechanica*, 234, 05 2022.
- [10] Nasim Fallahi, Andrea Viglietti, Erasmo Carrera, Alfonso Pagani, and Enrico Zappino. Effect of fiber orientation path on the buckling, free vibration, and static analyses of variable angle tow panels. *Facta Universitatis, Series: Mechanical Engineering*, 18:165, 07 2020.

- [11] Yang Yan, Alfonso Pagani, and Erasmo Carrera. Thermal buckling solutions of generic metallic and laminated structures: Total and updated lagrangian formulations via refined beam elements. *Journal of Thermal Stresses*, 45:1–26, 07 2022.
- [12] A.V. Duran, Nicholas Fasanella, Veera Sundararaghavan, and Anthony Waas. Thermal buckling of composite plates with spatial varying fiber orientations. *Composite Structures*, 124, 06 2015.
- [13] Mojtaba Farrokh, Majid Afzali, and Erasmo Carrera. Mechanical and thermal buckling loads of rectangular fg plates by using higher-order unified formulation. *Mechanics of Advanced Materials and Structures*, 28, 03 2019.
- [14] Mojtaba Farrokh, Mohammad Taheripur, and Erasmo Carrera. Optimum distribution of materials for functionally graded rectangular plates considering thermal buckling. *Composite Structures*, 289:115401, 03 2022.
- [15] Fiorenzo Fazzolari and Erasmo Carrera. Accurate free vibration analysis of thermo-mechanically pre/post-buckled anisotropic multilayered plates based on a refined hierarchical trigonometric ritz formulation. *Composite Structures*, 95:381–402, 10 2013.
- [16] Prof. Olivier Polit Dr. Adriano Calvi Pietro Nali, Prof. Erasmo Carrera. Modeling and validation of multilayered structures for spacecraft, including multifield interactions.
- [17] E. Carrera M. Petrolo. Best theory diagrams for multilayered structures via shell finite elements. *Advanced model and simulation in engineering sciences*, 2019.
- [18] M. Petrolo & E. Zappino E. Carrera, M. Cinefra. *Finite Element Analysis of Structures through Unified Formulation*. Wiley, 2014.
- [19] E. Riks. *Encyclopedia of Computational Mechanics*.
- [20] E. Carrera, editor. *Sull'uso dell'operatore secante in analisi non lineare di strutture multistrato con il metodo degli elementi finiti*.
- [21] Bin Wu, Alfonso Pagani, M. Filippi, W. Chen, and Erasmo Carrera. Large-deflection and post-buckling analyses of isotropic rectangular plates by carrera unified formulation. *International Journal of Non-Linear Mechanics*, 116, 05 2019.
- [22] Michele D'Ottavio and Erasmo Carrera. Variable-kinematics approach for linearized buckling analysis of laminated plates and shells. *Aiaa Journal - AIAA J*, 48:1987–1996, 09 2010.
- [23] H. Matsunaga. Buckling instabilities of thick elastic beams subjected to axial stresses. *Computers Structures*, 59(5):859–868, 1996.
- [24] A. Steinboeck, Xin Jia, Gerhard Hoefinger, H. Rubin, and H.A. Mang. Remarkable postbuckling paths analyzed by means of the consistently linearized eigenproblem. *International Journal for Numerical Methods in Engineering*, 76:156 – 182, 10 2008.
- [25] Erasmo Carrera and Luciano Demasi. Classical and advanced multilayered plate elements based upon pvd and rmvt. part 1: Derivation of finite element matrices. *Internaltional journal for numerical methods in engineering*, 55:191–231, 2002.
- [26] Erasmo Carrera. *Mechanics of Multilayered Composite Structures: Basics Concepts and Advanced Theories*.

- [27] Paul M Weaver Zhangming Wu, Gangadharan Raju. Optimization of postbuckling behaviour of variable thickness composite panels with variable angle tows: Towards “buckle-free” design concept.
- [28] Erasmo Carrera. Temperature profile influence on layered plates response considering classical and advanced theories. *Aiaa Journal - AIAA J*, 40:1885–1896, 09 2002.
- [29] M. Cinefra, Stefano Valvano, and Erasmo Carrera. Heat conduction and thermal stress analysis of laminated composites by a variable kinematic mitc9 shell element. *Curved and Layered Structures*, 2, 01 2015.